

GAMMA-RAY IMAGING AND POLARIZATION MEASUREMENT USING 3-D POSITION-SENSITIVE CdZnTe DETECTORS

by
Dan Xu

A dissertation submitted in partial fulfillment
of the requirements for the degree of
Doctor of Philosophy
(Nuclear Engineering and Radiological Sciences)
in The University of Michigan
2006

Doctoral Committee:

Associate Professor Zhong He, Chair
Professor James Paul Holloway
Emeritus Professor Glenn F. Knoll
Professor Jianjun Shi

© Dan Xu 2006
All Rights Reserved

To my family.

ACKNOWLEDGEMENTS

First and foremost I would like to express my gratitude to my advisor, Prof. Zhong He, for all his guidance and support throughout my graduate career. Words can not describe my appreciation to him. This work would not have been possible without his support. I would also like to thank Prof. Glenn Knoll, who was always overlooking my research progress and gave me encouragements. I am thankful to Prof. James Holloway and Prof. Jianjun Shi for serving on my dissertation committee and providing many thoughtful comments and suggestions about this thesis.

I appreciate Dr. Feng Zhang for his marvelous work on the 3-D CdZnTe detectors. Without his solid development on the detector hardware, all my work would only have been pictures on paper. Many thanks are due to Dr. Carolyn Seifert. Her previous work built a solid foundation for the gamma-ray Compton imaging using a single 3-D CdZnTe detector. It was her pioneer work that led me into this interesting and promising research field. I would also like to thank other members in the group, including Prof. James Baciak, Prof. Ling Jian Meng, Benjamin Sturm, Scott Kiff, and Steve Anderson. They are always there whenever I need help. Special thank goes to Prof. Jeffrey Fessler, who provided valuable insights when I was uncertain about the methods I used in the maximum likelihood reconstruction.

I would like to thank the Department of Nuclear Engineering and Radiological Sciences, the faculty, the staff and the students. To a student studying abroad, the friendship, the goodwill, and the brotherhood I found here are invaluable and always

keep me warm. I am also thankful to the Department of Energy for the financial support throughout the past five years.

I am so grateful to my parents, Dacheng Xu and Hefeng Tang, for their full support from the other side of the earth, although I am their only son and I know they desperately want to see me everyday. I know I am deeply in debt to my wife, Yan Cao, for all her love, support, and encouragement since we met. Her cleverness often sparked my thoughts, her trust gave me confidence, and most importantly, her selfless love was the source of my strength to go through the past few years. Although my family contributed little to this thesis academically, they provided a firm mental base of this thesis.

TABLE OF CONTENTS

DEDICATION	ii
ACKNOWLEDGEMENTS	iii
LIST OF FIGURES	viii
LIST OF TABLES	xiv
CHAPTER	
I. INTRODUCTION	1
1.1 Principles of Compton Camera Systems	1
1.2 History of Compton Camera Development	3
1.3 Objectives of This Work	8
II. 3-D POSITION-SENSITIVE CdZnTe DETECTORS	10
2.1 The Shockley-Ramo Theorem	11
2.2 Single Polarity Charge Sensing	12
2.2.1 Frisch Grids in Gas Detectors	13
2.2.2 Coplanar Grids	14
2.2.3 Pixellated Anode	15
2.2.4 3-D Position Sensing	17
2.3 3-D Position-Sensitive CdZnTe Detector	19
2.3.1 Hardware	20
2.3.2 Performance	23
2.3.3 Demonstration of the 3-D Position-Sensing Technique by Muon Tracks	26
2.4 Detector System Limitations	29
2.4.1 Anode Threshold	29
2.4.2 ASIC Dynamic Range	29
2.4.3 Charge Sharing between Neighboring Pixels	30
2.4.4 Multiple Interactions under One Pixel	31
III. SEQUENCE RECONSTRUCTION	36
3.1 Simple Comparison Method	37
3.2 Deterministic Method	42
3.3 Deterministic Method with Known Source Direction	43
IV. ANGULAR UNCERTAINTIES	47
4.1 Angular Resolution Measurement	47

4.2	Factors Contributing to the ARM	49
4.2.1	Detector Position Uncertainties	49
4.2.2	Detector Energy Uncertainties	50
4.2.3	Doppler Broadening	52
4.2.4	Coherent Scattering	54
4.2.5	Comparison of the Factors Contributing to the ARM	56
4.3	Modeling of Angular Uncertainties	58
4.3.1	Detector Position Uncertainties	59
4.3.2	Doppler Broadening	61
4.3.3	Detector Energy Uncertainties	65
V.	IMAGE RECONSTRUCTION	68
5.1	The Simple Back-Projection Algorithm	68
5.2	The Filtered Back-Projection Algorithm	70
5.2.1	Spherical Harmonics	72
5.2.2	Spherical Deconvolution	72
5.2.3	Filter Design from Theoretical Calculation	76
5.2.4	Filter Design from Monte Carlo Simulations	84
5.2.5	Performance	88
5.3	The List-Mode Maximum Likelihood Expectation Maximization Algorithm	91
5.3.1	The MLEM Algorithm for Photon-Emission Imaging Systems	91
5.3.2	Properties of the MLEM algorithm	96
5.3.3	The List-Mode MLEM Algorithm	99
5.3.4	Performance	100
5.4	3-D Imaging	103
VI.	ENERGY-IMAGING INTEGRATED DE-CONVOLUTION	108
6.1	Spectral Deconvolution in Energy Space	108
6.2	Energy-Imaging Integrated Deconvolution	111
6.2.1	Modeling of the System Response Function	113
6.2.2	Factors not Included in the Model	127
6.2.3	Verification of the System Response Function	128
6.2.4	Calculation of the Sensitivity Image	130
6.3	Performance	133
6.3.1	Deconvolution Using Simulation Data	134
6.3.2	Deconvolution Using Experiment Data	136
6.3.3	Comparison with Conventional Compton Imaging and Energy Spectral Deconvolution	138
VII.	POLARIZATION MEASUREMENT	143
7.1	The Klein-Nishina Formula for Polarized Incident Gamma-Rays	144
7.2	Polarimetry Using Compton Scattering	146
7.3	Experiment Setup	147
7.4	Theoretical Prediction of the Modulation Ratio Amplitude	148
7.5	Simulations	150
7.6	Results	152
VIII.	Summary and Future Work	157
8.1	Summary	157
8.2	Suggestions for Future Work	160

BIBLIOGRAPHY	162
-------------------------------	------------

LIST OF FIGURES

Figure

1.1	A gamma-ray Compton scattered by an electron.	1
1.2	If a gamma-ray interacts at least twice in the detector, the direction of the incident gamma-ray can be constrained on the surface of a cone. The half angle is determined by the energy losses, the cone vertex is placed at the first interaction position, and the cone axis is defined by the first and the second interaction positions.	2
1.3	Interaction cross sections for gamma-ray with energy between 0.01 MeV and 10 MeV in CdZnTe detector.	3
2.1	Frisch grid detector and the weighting potential distribution of its anode.	13
2.2	Electrodes configuration on coplanar grid detectors. (a) Cross-sectional view of the detector. (b) Anode pattern.	14
2.3	Weighting potentials of each electrode in coplanar grid detectors.	15
2.4	Weighting potential in a detector with a pixellated anode array.	16
2.5	3-D position-sensitive CdZnTe detector.	20
2.6	Depth sensing by measuring electron drift time for multiple interaction events. . .	21
2.7	A $15\text{mm} \times 15\text{mm} \times 10\text{mm}$ 3-D position-sensitive CdZnTe detector. (a) The cathode side. (b) The ceramic plate glued to the anode side. (c) A broken detector shows the anode structure and the ceramic plate facing the detector anode.	22
2.8	A 3-D CdZnTe detector mounted to a hybrid board.	23
2.9	Illustration of the VAS channel and the TAT channel.	24
2.10	Depth separated spectra for single-pixel photopeak events at 662 keV.	25
2.11	Timing spectra separated by C/A ratio for single-pixel photopeak events at 662 keV.	26
2.12	Timing spectra peak centroid vs. depth by C/A ratio.	27
2.13	Some muon tracks observed in a 3-D position-sensitive CdZnTe detector.	28
2.14	Depth difference distribution of neighboring and non-neighboring two-pixel photopeak events at 662 keV.	34

2.15	Depth difference distribution between two interactions under the same pixel.	35
3.1	Fractions of full-energy two-pixel events in the three different groups as a function of the incident gamma-ray energy.	40
3.2	Fraction of simulated full-energy two-pixel events which are correctly sequenced by the simple comparison method and the deterministic method.	41
3.3	Klein-Nishina cross section in the three different groups as a function of the incident gamma-ray energy. When the incident gamma-ray energy is less than $m_e c^2/2$, all scattering events fall in group 1, which can be correctly sequenced by the Compton edge test.	42
3.4	The two back-projection cones of a two-pixel event. The correct sequence is $(E_1, \mathbf{r}_1) \rightarrow (E_2, \mathbf{r}_2)$. In far field imaging, the two back-projection cones overlap with each other when $\theta_1 + \theta_2 = 180^\circ$	44
3.5	The average difference between $\theta_1 + \theta_2$ and 180° , $E(\theta_1 + \theta_2 - 180^\circ)$, is calculated by simulations. The full energy two-pixel events that can not be identified by the Compton edge test were used. When the gamma-ray energy is below $m_e c^2/2$, all full energy two-pixel events can be correctly identified by energy depositions. . . .	45
4.1	The Angular Resolution Measurement.	48
4.2	The ARM distribution of two-pixel photopeak events at 662 keV due to the detector position uncertainties.	50
4.3	The ARM distribution of two-pixel photopeak events at 662 keV due to the detector energy uncertainty.	52
4.4	The ARM distribution of two-pixel photopeak events at 662 keV due to the detector energy uncertainty. The scattering angles of those events are within $90^\circ \pm 2.5^\circ$. . .	53
4.5	The ARM distribution of two-pixel photopeak events at 662 keV due to Doppler broadening.	54
4.6	Percentage of two-pixel photopeak events that are coherent scattered before the gamma-rays are fully stopped.	55
4.7	The ARM distribution of two-pixel photopeak events at 662 keV that are coherent scattered before the gamma-rays are fully stopped.	56
4.8	The standard deviations of the overall ARM distributions at different incident gamma-ray energies.	57
4.9	Angular uncertainty caused by the detector position uncertainties.	61
4.10	Double differential Compton cross section in $\text{Cd}_{0.9}\text{Zn}_{0.1}\text{Te}$. The incident photon energy is 662 keV. The color bar on the right represents the values of the double differential Compton cross section, which has units of $\text{barn} \cdot \text{MeV}^{-1} \cdot \text{Sr}^{-1}$	64
4.11	Scattering angle distributions at different energies of the scattered photon with 662 keV incident photon energy.	65

4.12	Standard deviations in the ARM distributions due to Doppler broadening at different scattering angles with 662 keV incident photon energy.	66
4.13	Standard deviations in ARM distributions due to the energy uncertainty at different scattering angles with 662 keV incident photon energy.	67
5.1	Simple back-projection image of a point ^{137}Cs source placed at the side of the detector.	69
5.2	Simple back-projection image of the ^{214}Bi 609 keV photopeak. The image shows the concrete distribution, and the cold area on the left represents a window in the lab.	70
5.3	Summation of cone-beam projections on the unit sphere	75
5.4	The contribution of a cone-beam projection with cone axis $\vec{\Omega}$ and half angle θ to the PSF	77
5.5	Two possible sequences in a two-pixel event. θ_1 and θ_2 are the two possible scatter angles.	80
5.6	The contribution of an incorrectly sequenced event to the PSF. The event generates a cone-beam projection with cone axis $\vec{\Omega}$ and half angle $\pi - \theta_2$	82
5.7	The upper figure shows the PSF of all two-pixel events at 662 keV with sequence reconstruction algorithm applied. Due to the azimuthal symmetry of the PSF, the Fourier transform of the PSF into the spherical harmonics domain can be simplified to the Legendre polynomial expansion. The bottom figure shows the Legendre polynomial coefficients.	84
5.8	The simulation shows that the actual scattering angle distribution of 662 keV gamma rays in a 3-D CdZnTe detector is different from the theoretical prediction based on the Klein-Nishina formula, thus the actual PSF should be different from Eq. 5.23.	85
5.9	Simulated PSF. A 662 keV gamma-ray source was placed at the side of the detector, and only two-pixel full-energy deposition events were reconstructed.	86
5.10	The upper figure shows the simulated PSF and the actual PSF used in the reconstruction. The incident gamma-ray energy is at 662 keV. The coefficients of the Legendre polynomials are shown in the bottom figure. The PSFs are for a single 15 mm \times 15 mm \times 10 mm 3D CdZnTe detector.	87
5.11	Reconstructed images of the simulated data with five Cs-137 point sources. (a). Simple back-projection. The five sources can not be distinguished. (b). Filtered back-projection with the theoretical PSF shown in Fig. 5.7. The five sources can be distinguished. (c). Filtered back-projection with the simulated PSF shown in Fig. 5.10. It has better angular resolution than the image reconstructed with the theoretical PSF.	89

5.12	Reconstructed images of the measured data with two Cs-137 sources separated by 15 degrees. (a). Simple back-projection of the reconstruction cones. The two sources can not be distinguished. (b). Filtered back-projection with the theoretical PSF shown in Fig. 5.7. The two sources can barely be distinguished. (c). Filtered back-projection with the simulated PSF shown in Fig. 5.10. The two sources can be distinguished clearly.	90
5.13	A linear imaging system.	92
5.14	Reconstructed images of the simulated data with five Cs-137 point sources. (a). Simple back-projection. (b). Filtered back-projection with the simulated PSF shown in Fig. 5.10. (c). MLEM reconstructed image after 24 iterations.	101
5.15	Reconstructed images of the measured data with two Cs-137 point sources separated by 15 degrees. (a). Simple back-projection. (b). Filtered back-projection with the simulated PSF shown in Fig. 5.10. (c). MLEM reconstructed image after 24 iterations.	102
5.16	Convergence speed of the MLEM algorithm on the simulated data with five point Cs-137 sources. The red curves show the log likelihood as a function of number of iterations. The blue curves show the difference between the current image and the previous image.	103
5.17	Illustration of the difference between far field imaging and near field imaging. In far field imaging, the vertex of each back-projection cone is approximately placed at the origin. In near field imaging, the vertex of each back-projection cone is placed at the first interaction position.	104
5.18	Reconstructed images at different focus distance. The measurement was taken with a Cs-137 point source placed 37 mm above the detector. The images were reconstructed using the filtered back-projection algorithm, and this figure shows the upper hemispheres.	104
5.19	Image resolution versus focus distance.	105
5.20	A vertical slice of the 3-D imaging space, which is a 200 mm \times 200 mm \times 200 mm cube around the detector. The measurement was taken with a Cs-137 point source placed 37 mm above the detector. The reconstruction algorithm was MLEM and was stopped after 24 iterations.	106
5.21	The geometry configuration of the simulation in which a Cs-123 source uniformly distributed on a “M” shape was placed 20 mm above a 3 \times 3 array of 3-D CdZnTe detectors.	107
5.22	Reconstructed image of the “M” shape Cs-137 source above a 3 \times 3 array of 3-D CdZnTe detectors. The MLEM algorithm was used and was stopped after 24 iterations.	107
6.1	Simulated energy response functions at different incident gamma-ray energies. . . .	110
6.2	Experiment setup. Three point sources (a ^{137}Cs , a ^{22}Na and a ^{133}Ba) were placed at three different sides of the 3-D CdZnTe detector.. . . .	110

6.3	Energy spectral deconvolution on the measured spectrum with three point sources. The top figure shows the measured raw spectrum of all events. The bottom figure shows the deconvolved spectrum.	111
6.4	A photon from pixel \mathbf{j} creates a two-interaction event \mathbf{i} , which consists of energy depositions of E_1 and E_2 at positions \mathbf{r}_1 and \mathbf{r}_2 , respectively.	116
6.5	The bin volumes in the measurement space are approximated by two spheres when calculating the system response function.	123
6.6	The escaping photon can be on any direction on the escaping cone. The half angle of the escaping cone can be calculated from E_0 , E_1 , and E_2	127
6.7	Comparison of the spectra generated from the system response function and the spectra from Geant4 simulations.	129
6.8	Comparison of the calculated sensitivity and the sensitivity from Geant4 simulations as a function of the incident gamma-ray energy.	133
6.9	Source distribution in the Geant4 simulation. The source is uniformly distributed around the side of the detector. The source energy increases from 300 keV to 1 MeV linearly as a function of the rotational angle from 0° to 360°	134
6.10	Simulated two-pixel spectrum and deconvolved spectrum.	135
6.11	Deconvolved spectra at different directions. The spectra show that the source is not only uniformly distributed in energy from 300 keV to 1 MeV, but it is also uniformly distributed across spatial directions.	136
6.12	The deconvolved images at the photopeak energies of the three sources. The 4π imaging space is projected onto a plane defined by the azimuthal and the polar angles of the sphere.	137
6.13	The upper figure is the measured two-pixel spectrum. The middle figure respectively shows the deconvolved spectra at the three source directions. The lower figure is the deconvolved spectrum from all directions.	138
6.14	Images of the 384 keV line from the ^{133}Ba source. (a) Reconstructed image by setting an energy window from 370 keV to 390 keV. (b) Energy-imaging integrated deconvolved image summed from 370 keV to 390 keV.	140
6.15	Images of the 511 keV line from the ^{22}Na source. (a) Reconstructed image by setting an energy window from 490 keV to 520 keV. (b) Energy-imaging integrated deconvolved image summed from 490 keV to 520 keV.	141
7.1	Compton scattering of a polarized photon at position O. ε_0 and ε' are the electric vectors of incident and scattered photons, respectively. θ is the scattering angle, ξ is the angle between the scattering direction and the electric vector of the incident photon, η is the angle between the electric vector of the incident photon and the scattering plane, and β is the angle between the electric vector of the scattered photon and OCAD plane.	145

7.2	The change of the modulation ratio amplitude according to different incident gamma-ray energies and scattering angles. For a fixed incident gamma-ray energy, the modulation ratio amplitude is maximized when the scattering angle is slightly less than 90°	148
7.3	Experimental setup. The Cs-137 source was scattered by the BaF ₂ scintillator before entering the CdZnTe detector. The scintillator was operated in coincidence with the CdZnTe detector to suppress the background. The CdZnTe detector is enclosed in the detector box and placed underneath the scintillator.	149
7.4	The modulation ratio from simulation. The amplitude of the modulation ratio is 0.225, which is slightly less than the theoretical value of 0.24. The difference is caused by the finite size of the scintillator, the different detection efficiencies for different scattering angles and the finite pixel size.	152
7.5	Simulated spectrometer and polarimeter efficiencies for CdZnTe and Ge detectors. The events useful for polarimeter are defined as non-neighboring two-pixel events. .	153
7.6	Top view of the measurement setup. The source was placed at four different locations to produce scattered gamma rays with different polarization directions, which can be deduced by measuring the distribution of the scattering direction in the CdZnTe detector. The CdZnTe detector was placed underneath the BaF ₂ scintillator and is not displayed in this figure.	154
7.7	Modulation ratio measured for 288 keV gamma rays with 60% polarization degree. The phase shift of the modulation ratio reflects the measured polarization direction, and the amplitude of the modulation ratio is proportional to the polarization degree.	155
7.8	Reconstructed image of the 90° -scattered photons after 24 iterations with the list-mode MLEM algorithm. The image shows the up and down hemispheres of the 4π imaging space. Since the scintillator has a finite size, the reconstructed image is a distributed phantom.	156

LIST OF TABLES

Table

2.1	Simulated Multiple Interactions under One Pixel Anode at 662 keV (Pixel Sharing)	32
6.1	Relative intensities of the four ^{133}Ba lines to the 356 keV line	139

CHAPTER I

INTRODUCTION

1.1 Principles of Compton Camera Systems

A gamma-ray mainly interacts with matter through three types of interaction mechanism: photoelectric absorption, Compton scattering, and pair production. In a Compton scattering event as illustrated in Fig. 1.1, the gamma-ray transfers part of its energy to an electron and is scattered at an angle θ with respect to its initial direction.

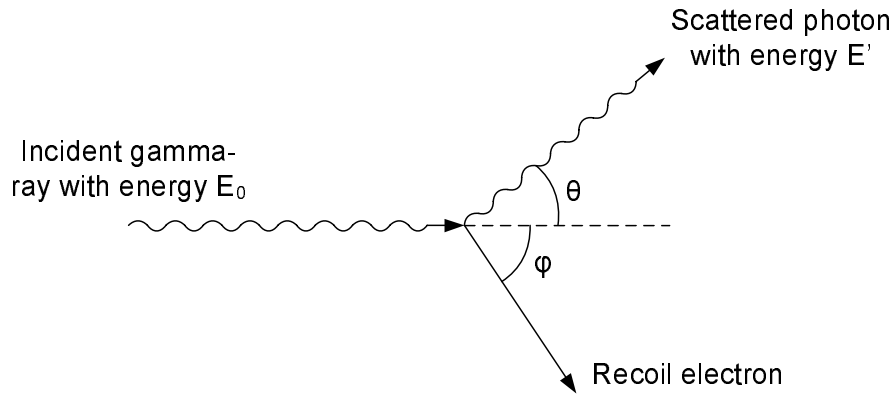


Figure 1.1: A gamma-ray Compton scattered by an electron.

Assuming the initial electron is free and at rest, according to the conservation laws of energy and momentum, the relationship between the scattered photon energy E' and the scattering angle θ can be derived as

$$E' = \frac{E_0}{1 + (E_0/m_e c^2)(1 - \cos \theta)} \quad (1.1)$$

in which $m_e c^2$ is the rest mass energy of an electron.

Eq. 1.1 also reveals that the scattered photon energy E' and the scattering angle θ are in one-to-one correspondence (bijective). Therefore, if the incident gamma-ray energy is known, the scattering angle θ can be determined uniquely based on the energy loss in the first scattering. If the scattered photon interacts with the detector by a photoelectric absorption or another Compton scattering, the positions of the two interactions can give the direction of the scattered photon. As a result, the direction of the incident gamma-ray can be constrained on the surface of a back-projection cone as shown in Fig. 1.2. With sufficient number of back-projection cones, the image of the gamma-ray source can be reconstructed.

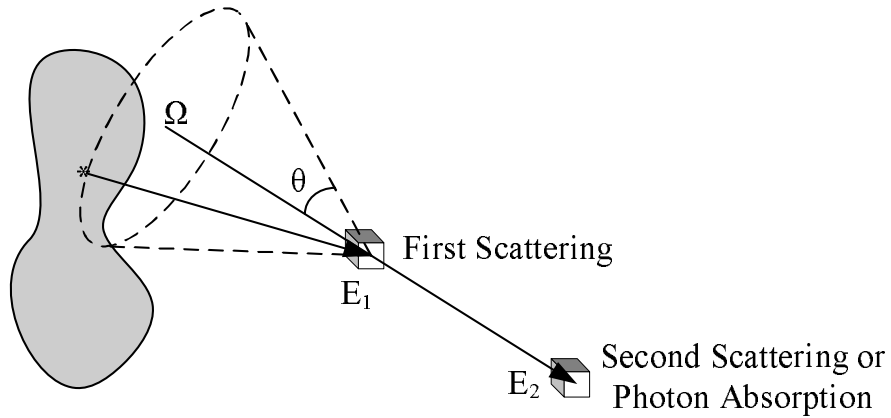


Figure 1.2: If a gamma-ray interacts at least twice in the detector, the direction of the incident gamma-ray can be constrained on the surface of a cone. The half angle is determined by the energy losses, the cone vertex is placed at the first interaction position, and the cone axis is defined by the first and the second interaction positions.

The recoil electron from a Compton scattering or a photoelectric absorption normally travels a few hundred microns before being fully stopped in a solid state detector. The measured position is the weighted centroid of this electron track unless the detector has electron tracking capability. Therefore, the measured electron positions are not exactly the interaction positions. However, in 3-dimensional position-sensitive cadmium zinc telluride (CdZnTe) detectors, the range of a recoil electron at

several hundred keV is far smaller than the position resolution, and the interaction positions are normally approximated by the measured electron positions.

Fig. 1.3 shows the various gamma-ray interaction cross sections in CdZnTe. When the gamma-ray energy is below 200 keV, photoelectric absorption is the most dominant interaction. When the gamma-ray energy is higher than 10 MeV, most interactions are pair productions. Compton scattering dominates from 300 keV to several MeV, which is the gamma-ray imaging energy range of the 3-D CdZnTe detector.

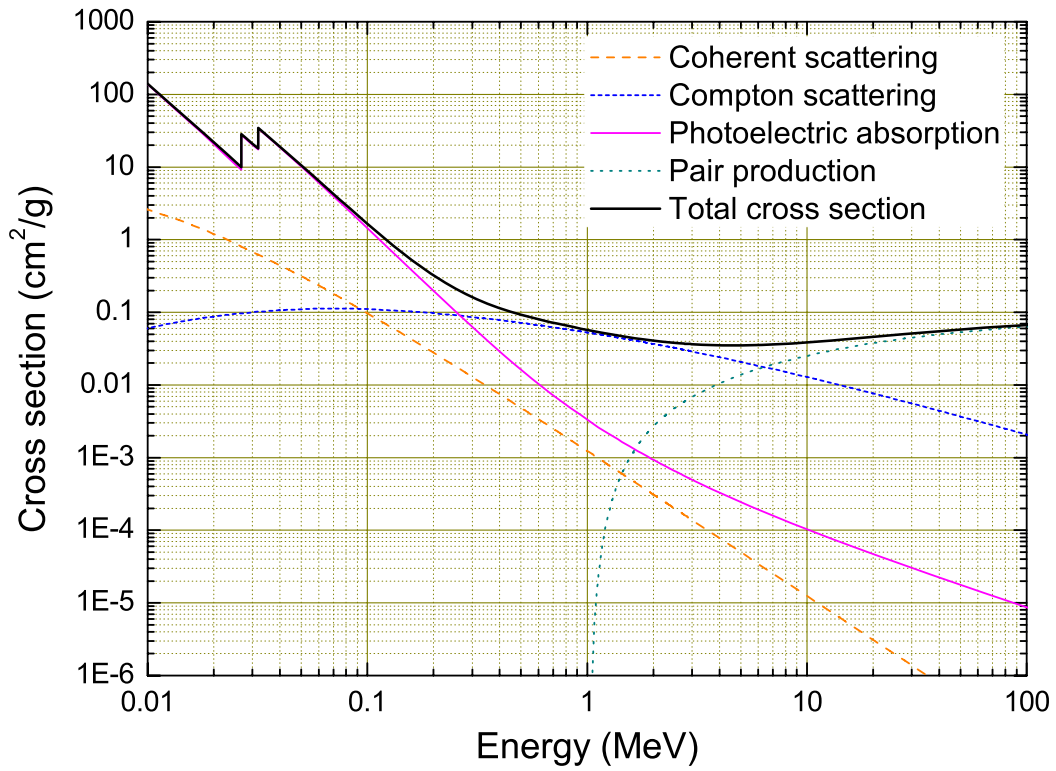


Figure 1.3: Interaction cross sections for gamma-ray with energy between 0.01 MeV and 10 MeV in CdZnTe detector.

1.2 History of Compton Camera Development

Among the various portions of the electromagnetic spectrum, the gamma-ray is one of the most difficult part to image due to its particle behavior, its high penetration power and complicated interactions with matter. Despite these challenges,

photon-emission imaging systems have generated great interest in the fields of nuclear medicine and astrophysics for many decades, and enormous efforts have been exerted to image the gamma-ray emission distribution. Various imaging systems have been developed, including Single Photon Emission Computed Tomography (SPECT)[1], Positron Emission Tomography (PET)[2], coded aperture cameras[3], rotating modulation collimators (RMC)[4], and Compton cameras[5, 6]. Among these gamma-ray imaging systems, Compton cameras are attractive because they do not require collimators and hold the promise of high detection efficiency.

Using Compton scatters to obtain directional information of the incident gamma-rays was proposed by Schönfelder *et al.*[7] in the early 1970s, and the instruments were carried on balloon flights to take measurements of the atmospheric gamma-rays. Soon thereafter, Todd proposed that the Compton imaging device for medical applications be used as an alternative to the mechanically collimated imaging system[8]. In the early 1980s, Singh and Doria developed the first Compton camera system for medical imaging[5, 6]. In 1991, NASA launched the Compton Gamma-Ray Observatory (CGRO), on which COMPTEL is one of the four telescopes covering an unprecedented electromagnetic spectrum from 30 keV to 30 GeV[9]. COMPTEL, which was designed with a sensitivity range from 1 MeV to 30 MeV, was a demonstrated success. It showed that a large-portion of gamma-ray emission between 1 MeV and 30 MeV was from our galaxy[10].

These early developments of Compton imaging systems were characterized by the employment of scintillators as both the front and the back detectors. With the development of semiconductor radiation detectors during 1980s and 1990s, many Compton camera systems followed the scheme proposed by Singh, which used semiconductor detectors as the front-plane detector and scintillator detectors as the back-plane

detector. In 1993, Martin *et al.* proposed a ring Compton scatter camera which consisted of a 4×4 array of HPGe detectors and a ring array of cylindrical NaI(Tl) scintillators[11].

In 1988, Kamae *et al.* developed a Compton imager by replacing the HPGe detectors in Singh's design with many layers of Si strip detectors[12]. The Si strip detectors were surrounded by a cylindrical CsI(Tl) scintillator. Two years later, Dogan, Wehe and Knoll proposed to reconstruct the image using multiple scattered gamma-rays[13] based on Kamae's design. In 1998, LeBlanc *et al.* built a prototype Compton camera system, C-SPRINT, for nuclear medicine as a Compton SPECT[14, 15]. Instead of using Si strip detectors, C-SPRINT consisted of $3 \text{ cm} \times 3 \text{ cm} \times 0.1 \text{ cm}$ Si pad detector modules that were pixellated into 22×22 arrays. The results showed that, in terms of noise equivalent sensitivity, the advantage of the C-SPRINT over a mechanically collimated SPECT system was limited at the low energy end, such as the 140 keV gamma-rays from $^{99\text{m}}\text{Tc}$, but it outperformed a mechanically collimated SPECT system at higher energies such as the 392 keV gamma-rays from $^{113\text{m}}\text{In}$ [16].

In 1989, Piercey *et al.* built the first Compton telescope with HPGe detectors for both the front and back planes[17]. Piercey used a single HPGe detector as the front detector and an array of four HPGe detectors as the back plane. In 1994, McKisson *et al.* reported the results of a Compton camera that used two HPGe detector arrays for both the front and back planes[18]. Two years later, Philips *et al.* replaced the HPGe detector arrays by two double-sided HPGe strip detectors[19]. The front detector was a 25×25 strip detector with 2 mm pitch, and the back detector was a 5×5 detector with 9 mm pitch. In 2001, Schmid *et al.* proposed a Compton camera by employing a single large volume segmented coaxial HPGe detector[20]. The position information

was obtained by the outer contacts and digital pulse-shape analysis. By using a single crystal to detect both the Compton scattering and the photo-electric absorption, the separation between the front and back planes was eliminated, resulting in efficiency being increased by one order of magnitude. However, due to the large preamplifier noise, the experiments could not locate the source position. In 2005, with the same design as Schmid's, Niedermayr obtained about 5° angular resolution at 662 keV with a relative efficiency of 0.3% [21]. In 2002, Wulf *et al.* demonstrated that the depth information of a HPGe double-sided strip detector could be obtained by measuring the timing difference between the cathode and anode signals. Thus a Compton camera could be realized by using a single HPGe double-sided strip detector [22]. In the following year, Wulf *et al.* designed a Compton imaging system with two HPGe double-sided strip detectors and demonstrated that the source location could be reconstructed by the three-Compton technique even if gamma-rays did not deposit full energy in the detectors [23].

In recent years, silicon detectors have become popular as the front detector because Doppler broadening is less severe in silicon due to its low atomic number. Silicon detectors are also more appealing than germanium detectors because of the less critical cooling requirement. In 2004, Wulf *et al.* built a Compton camera using three layers of double-sided silicon strip detectors. Each silicon detector had an active volume of $57\text{ mm} \times 57\text{ mm} \times 2\text{ mm}$, and had 64 strips on each side. The Compton camera showed an angular resolution of 3.3° at 662 keV [24]. If the incident gamma-ray interacts three or more times in the detectors, by employing the concept of three-Compton telescope proposed by Kroeger [25], the incident gamma-ray energy can be determined even if the gamma-ray is not fully absorbed. Multi-layer detector arrays are currently under development [26].

In 2005, Burks *et al.* from the Lawrence Livermore National Laboratory (LLNL) developed a Compton telescope using a double-sided silicon strip detector and a double-sided germanium strip detector. The two detectors are parallel, aligned on their center axis and separated by 6 cm. An angular resolution of 3° to 4° was reported in the energy range from 150 keV to 3 MeV[27].

In 2001, Du *et al.* from the University of Michigan used CdZnTe as the detectors in a Compton camera for the first time[28]. The CdZnTe detectors used in Du's work measured the 3-D position information of single gamma-ray interactions in the detector. Since a Compton camera needs at least two gamma-ray interactions, two 1 cm^3 3-D position-sensitive CdZnTe detectors were used in Du's experiment. The two CdZnTe detectors were separated by 5 cm, which limited the intrinsic efficiency at 511 keV to be only 1.5×10^{-4} . The measured angular resolution was 5.2° at 662 keV. Three years later, with the improved design of the application-specific integrated circuit (ASIC), the 3-D position information of multiple gamma-ray interactions in a single detector can be obtained by measuring the electron drift time[29]. This advance greatly improved the gamma-ray detection efficiency because about 60% of the photopeak events are multiple interaction events at 662 keV in a $15\text{ mm} \times 15\text{ mm} \times 10\text{ mm}$ detector. This new capability enabled Lehner and He to demonstrate Compton imaging using a single 3-D position-sensitive CdZnTe detector[30]. Because there is no requirement for mechanical collimators, a single 3-D CdZnTe detector can have a field of view (FOV) of 4π . Since there is no separation between the first and the second detector, and Compton scatters with all scattering angles can be detected, the imaging efficiency is three orders of magnitude higher than the previous two-detector CdZnTe system. The measured intrinsic imaging efficiency was 1.86%, and the measured angular resolution was 17° at 662 keV using a single

15 mm \times 15 mm \times 10 mm CdZnTe detector.

There are other Compton camera designs that are usually referred to as Advanced Compton Telescopes, and are mostly designed for astrophysics applications. Those Compton telescopes are characterized by the capability of tracking the recoil electrons. Examples of this type of Compton telescopes include the TIGRE experiment at the University of California, Riverside[31], the LXeGRIT project at Columbia University[32], and the MeV gamma-ray imaging detector developed at Kyoto University[33]. In these telescopes, silicon strip detectors, liquid xenon or gaseous time projection chambers (TPC) are used to track the recoil electrons. Because in a Compton scattering event, the incident gamma-ray, the scattered photon and the recoil electron must be on the same plane, the incident photon direction can be limited on a small portion of the back-projection cone by knowing the recoil electron direction, thus the angular resolution is improved.

1.3 Objectives of This Work

The 3-D position-sensitive CdZnTe detector is a novel instrument which can provide the energy and the position information of multiple gamma-ray interactions within a single detector. With this capability, many characteristics of the incident gamma-rays can be studied from the Compton scattering events. These characteristics include direction, distance, and polarization information. Because of the characteristics of Compton scattering, the system response function of multiple pixel events is not only a function of the incident gamma-ray energy, but it is also a function of the incident gamma-ray direction. Therefore, the distribution of the incident gamma-rays can be deconvolved in spectral and spatial domains simultaneously, and the deconvolved result represents the distribution of the incident gamma-rays before

they hit the detector.

The main objective of this work is to develop fast and real-time Compton imaging algorithms for 3-D position-sensitive semiconductor gamma-ray spectrometers, and to study the various characteristics of the incident gamma-rays based on the measured Compton scattering events. Chapter II introduces the principles and performances of the 3-D position-sensitive CdZnTe detectors. Because of the detector limitations, it is not possible to give the order of multiple interactions. For image reconstruction algorithms such as the simple back-projection algorithm and the filtered back-projection algorithm, sequence reconstruction is necessary and is discussed in Chapter III. Chapter IV analyzes the factors that contribute to the angular uncertainties of the imager, and models the angular uncertainties caused by individual factors. Chapter V describes different image reconstruction algorithms applied in this work, including the 3-D imaging technique which can estimate the source-to-detector distance when the source is in the vicinity of the detector. Chapter VI introduces a novel energy-imaging integrated deconvolution method, which deconvolves the measurement in both the spectral and the spatial domains. The proposed method provides the distribution of the incident gamma-rays as a function of both the energy and the direction. Chapter VII describes a method of measuring the polarization information of the incident gamma-rays, and the method is verified by experiment results. Finally, summary and future research interests are discussed in Chapter VIII.

CHAPTER II

3-D POSITION-SENSITIVE CdZnTe DETECTORS

Room temperature semiconductor radiation detectors, such as CdZnTe and HgI₂, are very attractive in many applications. They are usually characterized by high Z, high density, large band gap, and low average ionization energy per electron-hole pair. These properties enable these detectors to have high efficiency, to be operated at room temperature, and to have the potential to achieve high energy resolution. However, the charge carrier transport properties of these semiconductor materials are not as good as those in silicon or germanium. The trapping of charge carriers, especially holes, has limited the thickness of the detectors to a few millimeters for a long time. Although crystal growth techniques have been improved, the material non-uniformity is still a limiting factor of the detector size.

Single polarity charge sensing techniques became popular in developments of room temperature semiconductor detectors because the measured signals depend only on the movement of electrons. The elimination of signal dependence on the slow-moving, easily-trapped holes enables the detectors to be made in thicknesses over 10 mm. In addition, 3-D position-sensing technique overcomes the electron trapping and material non-uniformity problems by correcting the signal amplitudes as a function of the 3-D gamma-ray interaction position. As a result, excellent energy resolution

can be achieved.

This chapter first reviews the Shockley-Ramo Theorem, which describes the induced charge on an electrode by motion of charge carriers. Based on the Shockley-Ramo Theorem, various single polarity charge sensing techniques are discussed. The 3-D position-sensitive CdZnTe detector is described and the current limitations of the detector system are discussed.

2.1 The Shockley-Ramo Theorem

When a gamma-ray interacts with a detector through one of the three major interactions, an electron or an electron-positron pair is created. The electron or positron loses its energy by ionizing the detector material. In a semiconductor detector, electron-hole pairs are created by the ionization process. The number of electron-hole pairs is proportional to the energy loss of the gamma-ray in the detector. Therefore, by measuring a signal which is proportional to the number of electron-hole pairs, the initial energy loss of the gamma-ray can be obtained.

To read out the signal, an electric field is applied across the semiconductor detector to drive electrons towards the anode and holes towards the cathode. The movement of the charge carriers introduces a signal on the electrodes. The Shockley-Ramo Theorem provides a way to calculate the induced signal due to the motion of moving charge carriers[34].

The Shockley-Ramo Theorem states that the change of the induced charge ΔQ_L on an electrode L by the movement of charge q from position x_i to position x_f is

$$\Delta Q_L = \int_{x_i}^{x_f} q E_0 \cdot dx = -q[\varphi_0(x_f) - \varphi_0(x_i)] \quad (2.1)$$

in which E_0 and φ_0 are respectively the weighting field and the weighting potential, which are defined as the electric field and the potential under the conditions that

electrode L is at unit potential, all other electrodes are at zero potential, and all space charges are removed. The weighting potential is a unitless quantity.

From Eq. 2.1, we can see that the change of the induced charge on electrode L is only determined by the starting and stopping positions of the charge carriers, and is independent of the actual electric field and the space charges. The actual electric field only determines the speed and the trajectory of moving charge carriers. Eq. 2.1 provides an easy way to calculate the induced charge on any specific electrode even in a complicated electrode configuration.

The weighting potential can be determined by solving Poisson's equation

$$\nabla^2 \varphi_0 = -\frac{\rho}{\varepsilon_0} \quad (2.2)$$

in which ρ is the space charge density and ε_0 is the permittivity.

Because the weighting potential is calculated under the condition that all space charges are removed, Eq. 2.2 becomes Laplace's equation

$$\nabla^2 \varphi_0 = 0 \quad (2.3)$$

For a complicated electrode design such as coplanar grid or pixellated anode, Eq. 2.3 can be solved numerically by electromagnetic field simulation software packages such as Maxwell 3D from Ansoft.

2.2 Single Polarity Charge Sensing

In gas detectors, ions are much less mobile than electrons. Similarly, in room temperature semiconductor detectors, the hole mobility is much smaller than the electron mobility, and the hole trapping problem is much more severe. Therefore, it is desirable to design an electrode configuration in which the signal from one of the electrodes depends only on the movement of electrons. This approach is called single polarity charge sensing.

2.2.1 Frisch Grids in Gas Detectors

As early as 1944, Frisch first implemented a single polarity charge sensing technique in gas detectors[35]. In a planar gas detector configuration, a grounded Frisch grid is placed very close to the anode as shown in Fig. 2.1. The weighting potential of the anode is calculated by setting the anode potential to unity and the potential of the cathode and the Frisch grid to zero. As a result, the weighting potential remains zero between the cathode and the Frisch grid, and linearly rises to 1 from the Frisch grid to the anode. According to the Shockley-Ramo Theorem, the movement of electrons and ions between the cathode and the Frisch grid introduces no signal on the anode. Only when electrons pass the Frisch grid and drift towards the anode, the induced charge on the anode will rise from zero to the total charge carried by those electrons. Therefore, the output pulse amplitude is only proportional to the total number of electrons, and is totally independent of the movement of ions.

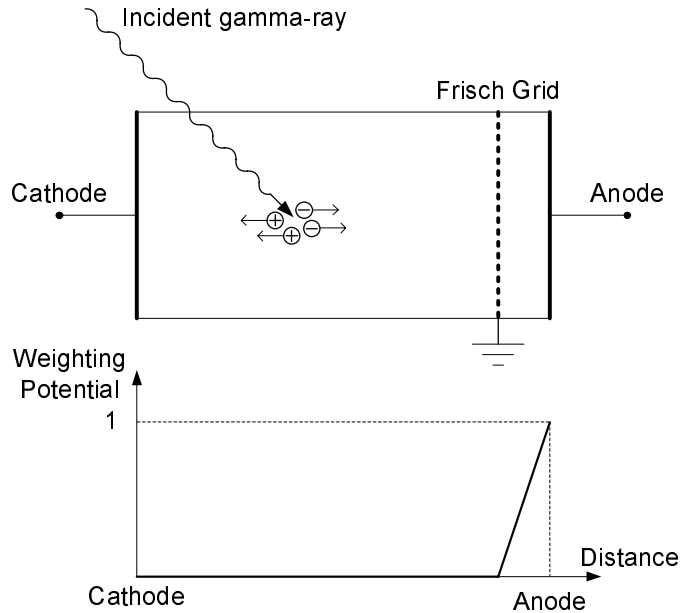


Figure 2.1: Frisch grid detector and the weighting potential distribution of its anode.

2.2.2 Coplanar Grids

The Frisch grid technique was successful in gas detectors. However, it is impractical to imbed a metal grid in a semiconductor crystal. In 1994, Luke realized that single polarity sensing could be implemented on semiconductor detectors by applying coplanar grid electrodes on the anode[36, 37]. The electrode configuration is illustrated in Fig. 2.2. The anode surface is applied with a pair of coplanar grid electrodes which are two groups of alternating strips. A small voltage difference is applied between the two electrodes so that the electrons always drift towards the one with higher potential. The anode receiving electrons is referred to as the collecting anode, and the other anode is referred to as the non-collecting anode. The cathode voltage is much higher than the voltage between the two anode electrodes so that the electric field is still uniform in most of the detector volume.

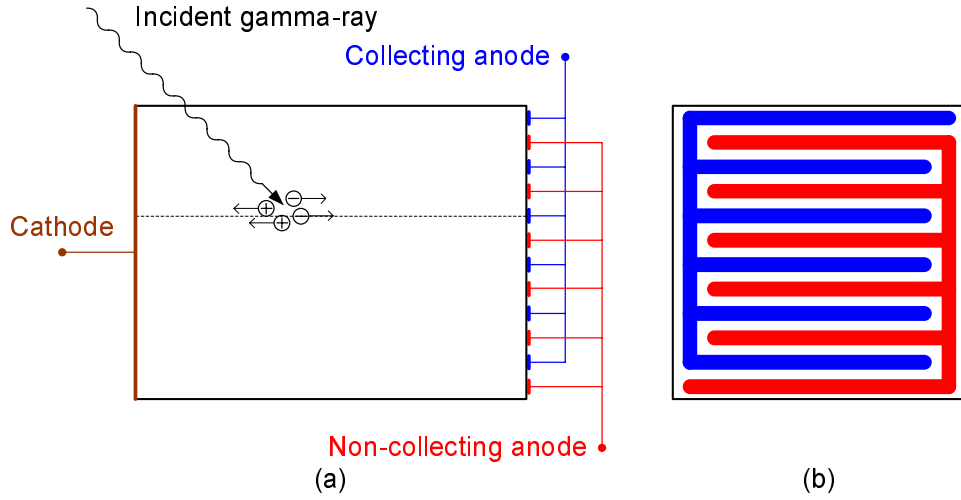


Figure 2.2: Electrodes configuration on coplanar grid detectors. (a) Cross-sectional view of the detector. (b) Anode pattern.

Fig. 2.3 illustrates the weighting potential distribution of each electrode along a line which is perpendicular to the electrode surfaces and intersects one of the collecting anode strips at its center, as shown by the dotted line in Fig. 2.2(a).

This line also resembles the actual trajectories of electrons. From the weighting potentials, we can see that when electrons are away from the anode surface, they induce identical charges on the collecting and non-collecting anodes because of the symmetry between the two electrodes. As electrons approach the collecting anode, the weighting potential of the collecting anode quickly rises to one, and the weighting potential of the non-collecting anode quickly drops to zero. The weighting potential difference between the collecting anode and the non-collecting anode is also shown in Fig. 2.1. We can see that the shape of the weighting potential difference is very similar to that of the Frisch grid gas chamber as shown in Fig. 2.2. Therefore, if the signal is read out by subtracting the non-collecting anode signal from the collecting anode signal, the readout signal is only proportional to the number of collected electrons, and single polarity charge sensing is implemented.

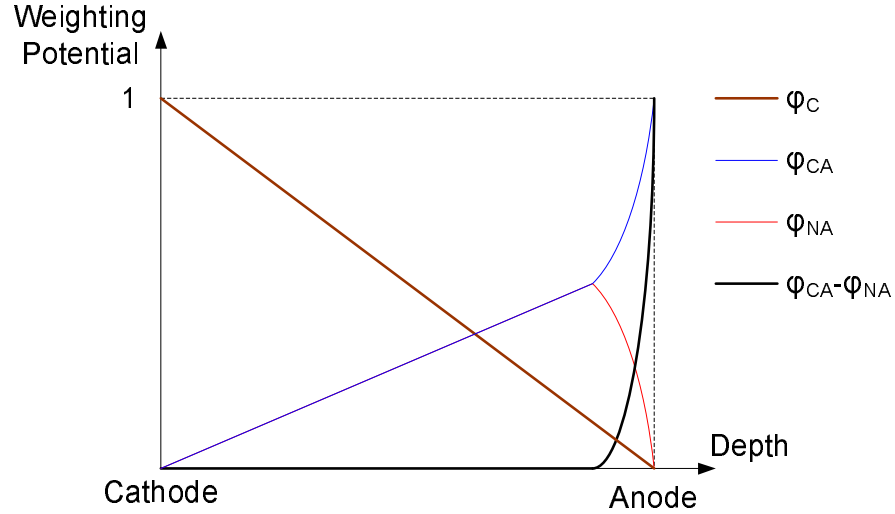


Figure 2.3: Weighting potentials of each electrode in coplanar grid detectors.

2.2.3 Pixellated Anode

Pixellated anode arrays can provide two-dimensional position information of gamma-ray interactions, which is required in imaging applications. Soon after Luke proposed the coplanar grid anode design, it was found that the pixellated anode readout signal

can be made relatively insensitive to the hole movement by carefully selecting the pixel size[38]. Therefore, detectors with pixellated anode arrays are single polarity charge sensing devices.

Fig. 2.4 illustrates the weighting potential in a detector with a pixellated anode array. The detector is $15\text{ mm} \times 15\text{ mm} \times 10\text{ mm}$ in dimension and employs an 11×11 pixel anode array on one $15\text{ mm} \times 15\text{ mm}$ surface as shown in Fig. 2.5. The depth is along a line which is perpendicular to the electrode surfaces and intersects the center of the central pixel anode. As shown in Fig. 2.4, the weighting potential stays very low when the depth is away from the anode, and increases quickly to one when the depth is close to the anode. Therefore, as electrons drift towards the pixel anode, the induced charge on the collecting pixel remains small when the electrons are far away, and increases quickly when the electrons are in the vicinity of the collecting anode.

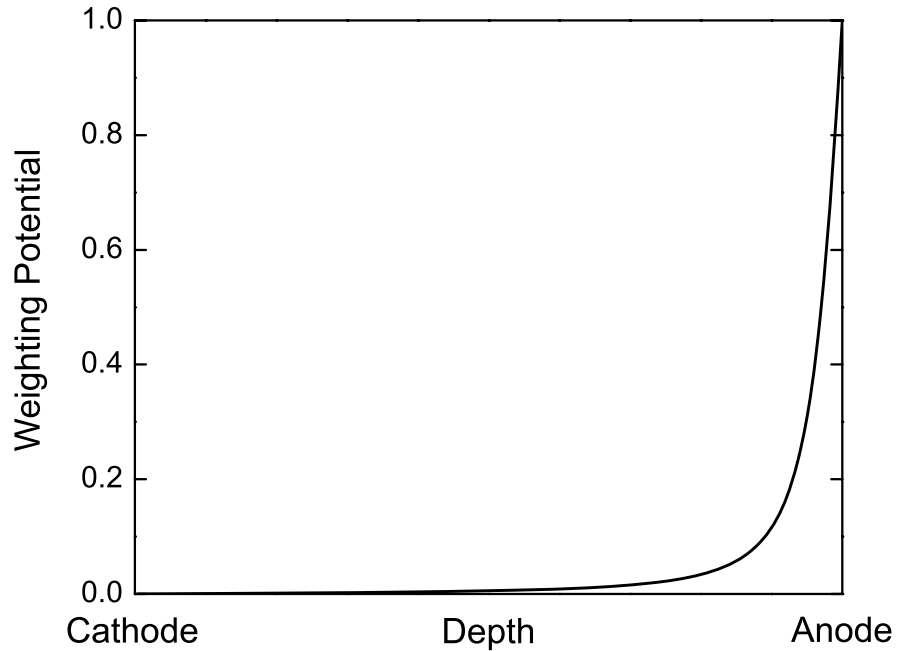


Figure 2.4: Weighting potential in a detector with a pixellated anode array.

From the shape of the weighting potential, it can be seen that interactions on

the cathode side introduce larger signals than interactions close to the anode side. However, the electron trapping has the opposite effect. The electron loss is higher if the electron travel distance is longer. Therefore, by carefully selecting the anode pixel size and the operating bias voltage, the electron trapping problem and the slowly rising weighting potential can compensate with each other, thus the energy resolution can be improved.

2.2.4 3-D Position Sensing

Although the readout signal by applying single polarity charge sensing techniques is only proportional to the number of collected electrons, the signal amplitude still depends on the gamma-ray interaction depth due to the electron trapping problem. The number of collected electrons will be smaller if the gamma-ray interaction occurs at the cathode side since the travel length of the electrons is longer. For coplanar grid anode designs, one method to compensate the electron trapping is to apply a relative gain when subtracting the non-collecting anode signal from the collecting anode signal ($\varphi = \varphi_{CA} - G \cdot \varphi_{NA}, G < 1$). In this way, the signal of a gamma-ray interaction at the cathode side is higher due to the weighting potential, thus the electron trapping effect can be compensated.

For pixellated anode designs, although the shape of the weighting potential mitigates the effect of the electron trapping problem, the pixel size and the cathode bias voltage need to be carefully chosen to optimally compensate the electron trapping. However, since the electron transport properties (mobility μ_e and lifetime τ_e) can vary from detector to detector, it is impractical to optimize the pixel size for every detector. Even if the pixel size is fixed, there is only one optimal bias voltage under which the electron trapping can be fully compensated, and that optimal bias voltage is usually different from the actual operating bias voltage. Since electron trapping is

depth dependent, He *et al.* proposed a method to correct the signal as a function of interaction depth by using the cathode to anode (C/A) ratio[39, 40].

As shown in Fig. 2.3, the cathode weighting potential is a linear function of the interaction depth. Base on the fact that the $\mu\tau$ product of holes is usually much lower than the $\mu\tau$ product of electrons in compound semiconductors, holes can be regarded as stationary during the collecting period of electrons. As a result, the cathode signal amplitude is only proportional to the number of electrons and the interaction depth. Since the anode signal amplitude is proportional to the number of electrons, the C/A ratio

$$\frac{V_c}{V_a} \propto \frac{ne_0 \cdot Z}{ne_0} = Z \quad (2.4)$$

is proportional to the interaction depth. In Eq. 2.4, n is the number of electrons, and Z is the distance from the interaction position to the anode.

The depth sensing technique was first applied to coplanar grid detectors as an alternative method to the relative gain method. However, it can also be applied to pixellated anode detectors. Together with the 2-D position sensing capability associated with the pixellated anode array, this technique can provide the 3-D position information of gamma-ray interactions in the detector[41].

The spectroscopic performance of a 3-D position sensitive semiconductor detector is superior due to the following two reasons. The first reason is that the pulse amplitude can be corrected as a function of the gamma-ray interaction position, therefore the variation of the pulse amplitude due to charge trapping and material non-uniformity can be minimized to the extent of the position resolution[42, 43]. The second reason is that the electronic noise is minimized because the leakage current and capacitance between the cathode and the anode are shared among all pixel anodes. Zhang *et al.* demonstrated that the 3D spectral response can be used to

study the possible defects in the detector, including electron trapping, variation in ionization energy, surface defect and variation in weighting potential[44]. In addition to the superb energy resolution, the 3-D position sensing capability is critical in gamma-ray imaging applications.

2.3 3-D Position-Sensitive CdZnTe Detector

The 3-D position sensing technique was applied to CdZnTe detectors by He *et al.* in 1998. The 3-D position-sensitive CdZnTe detector is illustrated in Fig. 2.5. The actual size of the detector is 15 mm \times 15 mm \times 10 mm. The anode surface is pixellated into an 11 \times 11 array. The pixel pitch is 1.27 mm \times 1.27 mm, which makes the effective volume of the peripheral pixels larger than the central pixels. In order to direct those electrons underneath the anode gap to the anode pixels, a steering grid with a bias slightly lower than the anodes is placed between the anode pixels. The first design used the C/A ratio to obtain the interaction depth if the incident gamma-ray deposits all or part of its energy in a single interaction. However, if the incident gamma-ray interacts more than once in the detector, the ratio between the cathode signal and the summed anode signal

$$\frac{V_c}{V_{a1} + V_{a2}} \propto \frac{n_1 e_0 Z_1 + n_2 e_0 Z_2}{n_1 e_0 + n_2 e_0} = \frac{n_1 Z_1 + n_2 Z_2}{n_1 + n_2} \quad (2.5)$$

can only give the centroid depth.

To obtain the individual depth of multiple interactions, the drift time of electrons is measured. As soon as electrons begin to move, they introduce a signal on the cathode. However, the anode signals remain small until electrons arrive within one pitch away from the anode surface as shown in Fig. 2.6. By applying a triggering threshold and measuring the time difference between the cathode trigger and the anode triggers, the drift time of each electron cloud from the interaction position

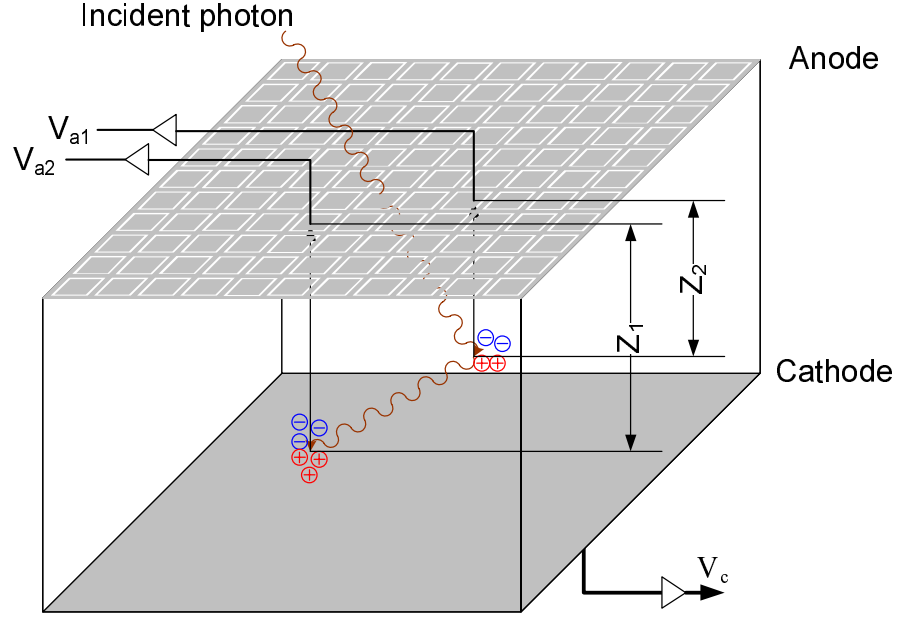


Figure 2.5: 3-D position-sensitive CdZnTe detector.

to the pixel anode can be measured. Assuming the electric field and the electron mobility are uniform across the detector, the electron drift velocity is a constant. As a result, the measured electron drift time can be used to estimate the interaction depth.

2.3.1 Hardware

The detector crystal was grown by eV Products, Inc. using the high-pressure Bridgman method. On one $15\text{ mm} \times 15\text{ mm}$ surface, the anode pixels and the steering grid were deposited using photolithography techniques. On the other $15\text{ mm} \times 15\text{ mm}$ side, the cathode covers the entire surface. The anode surface was glued to a ceramic plate, in which the anode pixels are wired to the four edges of the ceramic plate on the opposite side, as shown in Fig. 2.7.

The detector is supported by a polyvinyl chloride(PVC) mount and is placed in a hole of a hybrid board shown in Fig. 2.8, which has four VAS/TAT application specific integrated circuit(ASIC) chips. Each ASIC chip contains 32 channels, so

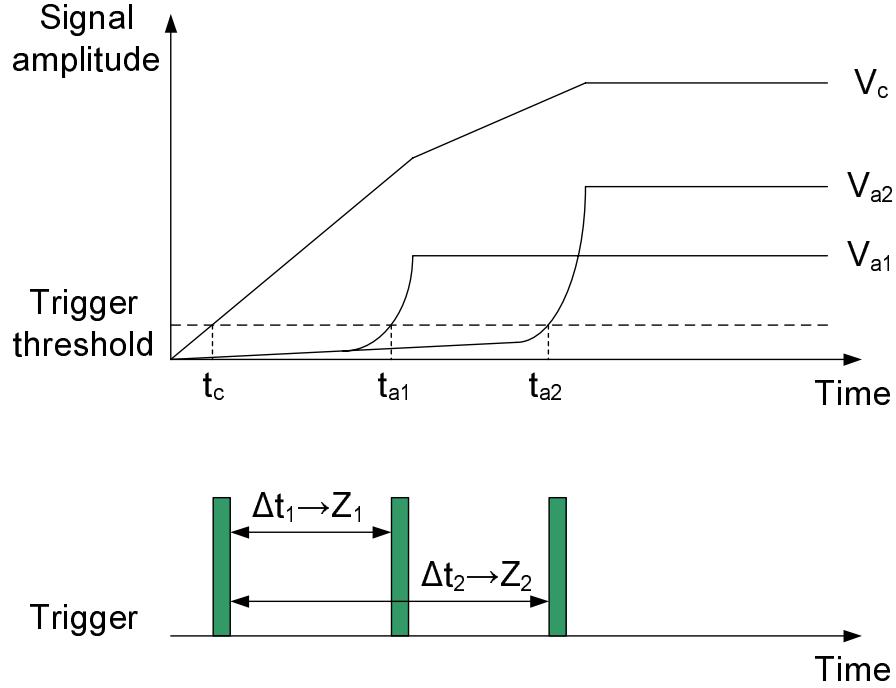


Figure 2.6: Depth sensing by measuring electron drift time for multiple interaction events.

there are 128 channels all together, among which 4 special channels are reserved for the cathode and anode grid signals. In actual measurements, only one cathode channel is used. The redundancy is due to the fragility of the cathode preamplifiers on the ASIC. The gold fingers on the ceramic plate are connected to the hybrid board through wirebonding. The ASIC hybrid board is connected to a controller card, which acts as an interface between the hybrid board and a data acquisition(DAQ) card in a computer.

Each channel in the ASIC contains a VAS circuit and a TAT circuit, as shown in Fig. 2.9. The VAS is used to measure the signal amplitudes and has a fixed shaping time of $1 \mu\text{s}$. The TAT has a much faster shaping time of 75 ns and has a time-to-amplitude converter (TAC) to measure the electron drift time. The TAT also provides the trigger for the system. If the signal from a TAT shaper exceeds a preset threshold, a trigger is generated for the corresponding channel. The system can be

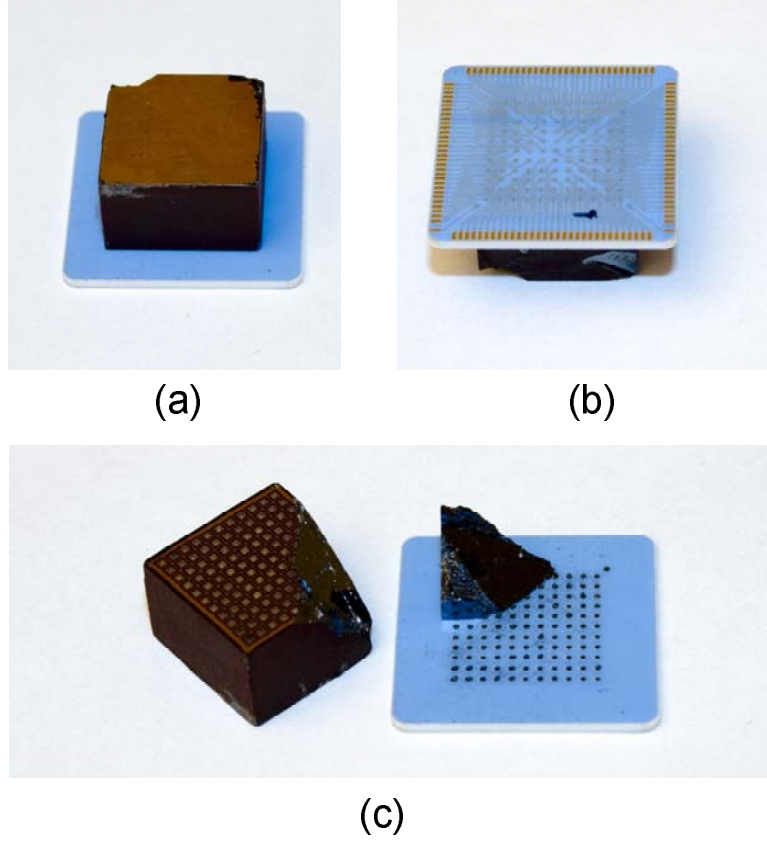


Figure 2.7: A $15\text{ mm} \times 15\text{ mm} \times 10\text{ mm}$ 3-D position-sensitive CdZnTe detector. (a) The cathode side. (b) The ceramic plate glued to the anode side. (c) A broken detector shows the anode structure and the ceramic plate facing the detector anode.

triggered by either the cathode or any of the anodes. The threshold for the cathode can be adjusted through a rheostat on the controller card, while the anode threshold can be adjusted through software. The threshold levels for all anode channels can be adjusted channel by channel.

If a gamma-ray deposits its energy in the detector through one or more interactions, as shown in Fig. 2.5, normally the cathode signal will first pass the trigger threshold of the cathode channel and therefore triggers the whole system. The signal from the cathode is sent to the VAS channel and its amplitude is held there. The signals from the anode pixels then trigger their corresponding TAT channels one after another, and are held in their corresponding VAS channels. After a fixed delay

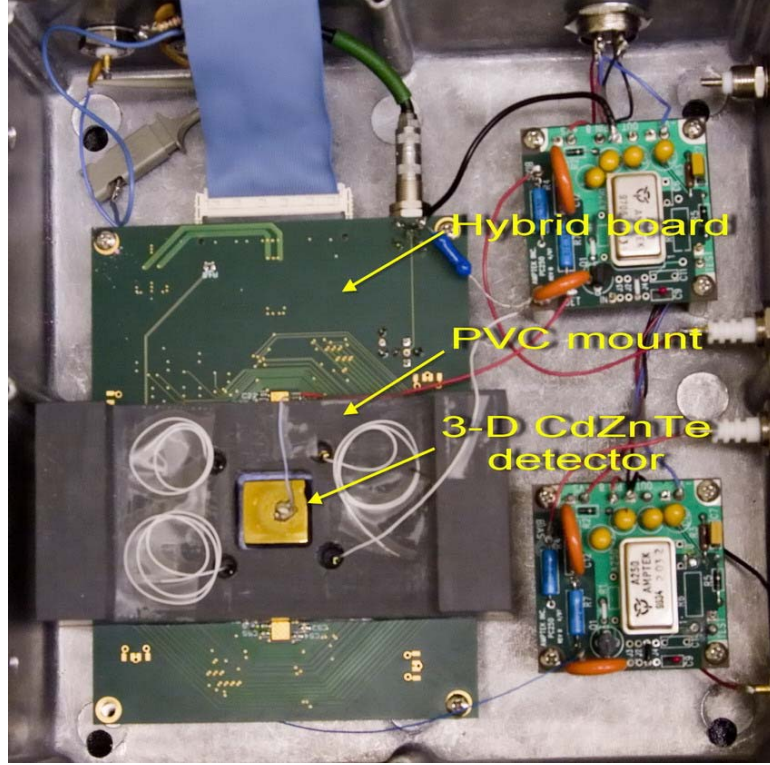


Figure 2.8: A 3-D CdZnTe detector mounted to a hybrid board.

from the first trigger, all the 128 ASIC channels (including both VAS and TAT) are read out by the controller card sequentially, and the signals are digitized by the DAQ card in the computer. The delay time between the first trigger and the read out is long enough for all electrons to be collected. The total time for all 128 channels to be read out is about $500\mu\text{s}$, which limits the highest count rate of the system to be 2000cps.

2.3.2 Performance

After the data is collected, the interaction depth can be obtained by the C/A ratio or the electron drift time, and the energy can be corrected as a function of the interaction depth. To obtain the correction data, the detector needs to be calibrated before use. Fig. 2.10 shows the depth separated spectra of one anode. As shown in the figure, the photopeak position varies at different depths due to the weighting

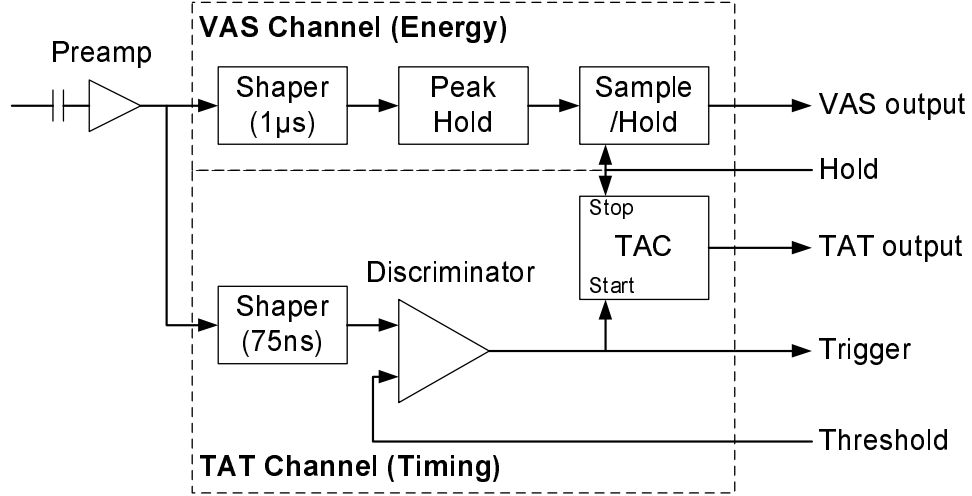


Figure 2.9: Illustration of the VAS channel and the TAT channel.

potential and the electron trapping. A gain factor can be obtained from the spectra for each depth and the energy deposited in the detector can be corrected.

After proper calibration procedures, the 3-D position sensitive CdZnTe detector can provide excellent energy spectra with full width half maximum (FWHM) below 1% at 662 keV for single-pixel events, and below 1.5% at 662 keV for two-pixel events[29, 45].

The position resolutions in the lateral directions are determined by the anode pixel size. In the $15\text{ mm} \times 15\text{ mm} \times 10\text{ mm}$ detector, the pixel size is about 1.3 mm. The depth information for single-pixel events can be obtained from either the C/A ratio or the electron drift time. Due to the poor timing resolution, the C/A ratio is always used to derive the interaction depth for single-pixel events, and the depth uncertainty is estimated to be 0.25 mm. For multi-pixel events, the depth information can only be determined by the electron drift time. To take advantage of the better depth resolution of the C/A ratio, a second order fit of the relationship between the electron drift time and the C/A ratio is generated from the single-pixel events during the calibration process. For multi-pixel events, the electron drift time is first

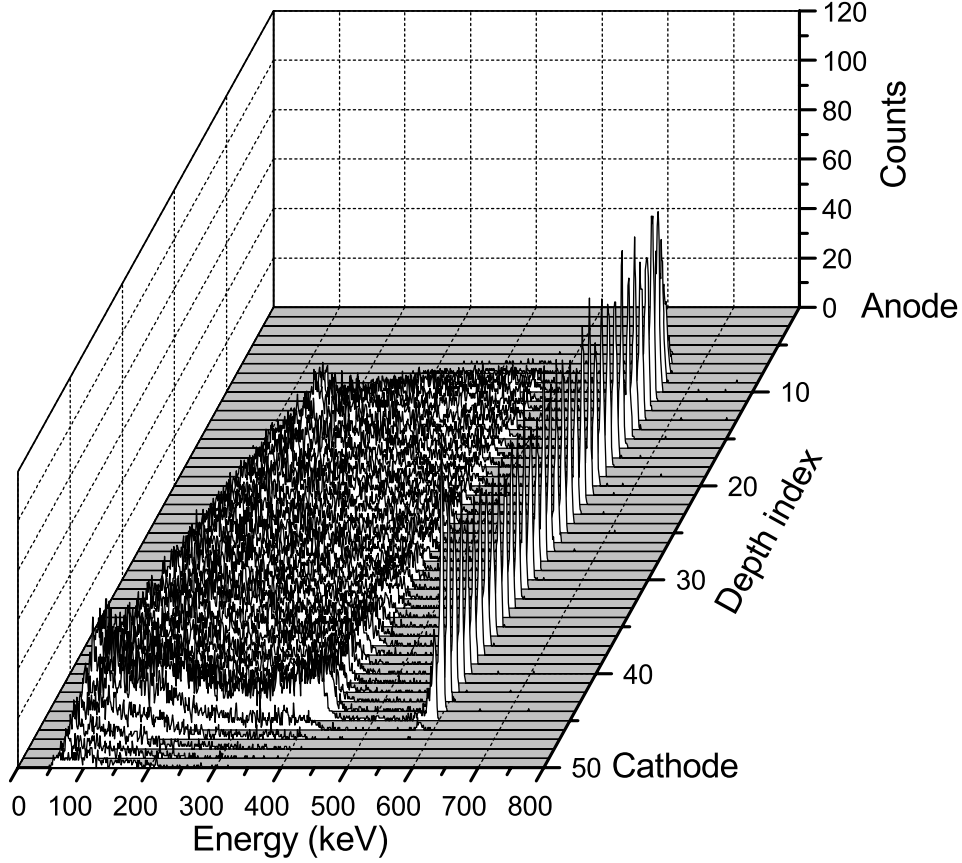


Figure 2.10: Depth separated spectra for single-pixel photopeak events at 662 keV.

converted into the corresponding C/A ratio, and the signal amplitude is corrected using the C/A ratio. The depth uncertainty for multi-pixel events is estimated to be 0.4 mm based on the timing resolution of 30ns FWHM of the TAT3[45].

Fig. 2.11 shows the timing spectra separated by the depth obtained by C/A ratio. The total span of the timing spectrum is about 200 channels, which corresponds to the total time required for electrons to drift from the cathode to the anode. At each depth, the FWHM of the timing spectrum is about 8 channels, which confirms the depth uncertainty obtained by the electron drift time is about $8/200 \times 10 \text{ mm} = 0.4 \text{ mm}$. Fig. 2.12 shows the relationship between the timing spectra peak centroid and the depth by the C/A ratio. A linear fit reveals there is non-linearity between the drift time and the C/A ratio. This is because there are non-linear factors in

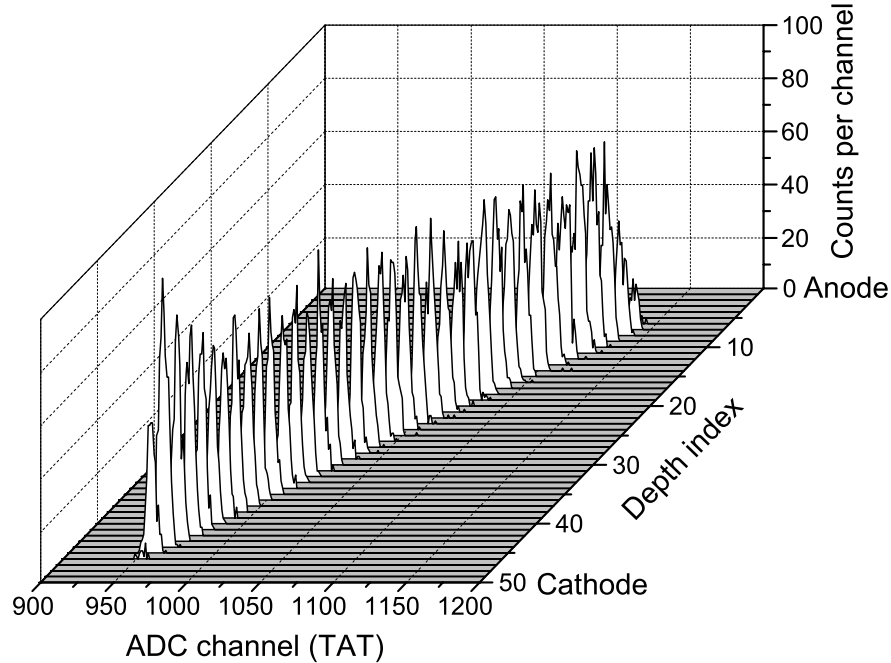


Figure 2.11: Timing spectra separated by C/A ratio for single-pixel photopeak events at 662 keV.

both the C/A ratio and the drift time as a function of the interaction depth. Those non-linear factors include the slowly rising weighting potential, electron trapping, hole movement and the triggering threshold. A second order fit accounts for most of the non-linearity.

2.3.3 Demonstration of the 3-D Position-Sensing Technique by Muon Tracks

Muon tracks were observed for the first time in a single semiconductor detector as a demonstration of the 3-D position-sensing capability.

The upper atmosphere of the earth is bombarded continuously by high energy cosmic rays which can carry energies up to 10^{20} eV. A high energy cosmic ray interacts with the upper atmosphere and creates a cascade of various consequential particles, which is known as the Extensive Air Shower (EAS). When this cascade reaches the ground, the most numerous particles are muons, which have an average energy of about 4 GeV[46]. Like electrons, muons are leptons with unit negative

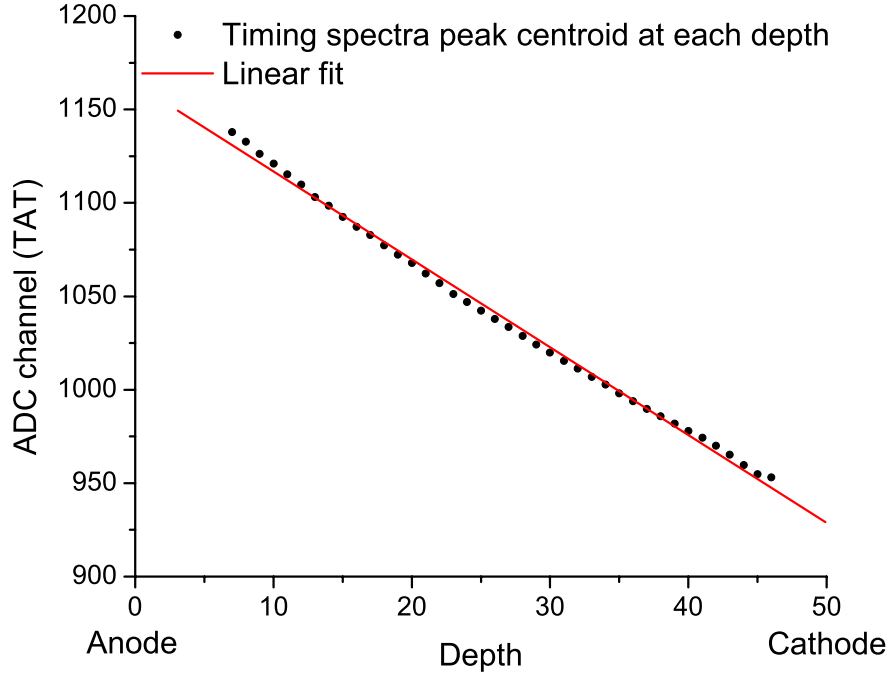


Figure 2.12: Timing spectra peak centroid vs. depth by C/A ratio.

charges. The mass of a muon is 206.768 times the mass of an electron.

The specific energy loss ($-dE/dx$) of a relativistic charged particle in a certain material approaches a constant as the energy of the charged particle increases. Those relativistic charged particles are also referred to as “minimum ionizing particles”. Muons at sea level with 4 GeV average energy fall into this category. Those muons can easily penetrate the $15\text{ mm} \times 15\text{ mm} \times 10\text{ mm}$ CdZnTe detector and leave tracks of electron hole pairs by ionization.

For minimum ionizing particles, the energy loss in a material is roughly proportional to the density of the material. The sea level cosmic ray muons deposit 5.92 MeV/cm in CsI[47] and 4.8 MeV/cm in NaI[48]. According to the mass densities of CsI, NaI, and CdZnTe, the specific energy loss of sea level muons in CdZnTe material can be estimated to be 7.6 MeV/cm. The muons have enough energy to penetrate the whole detector, thus about 10 MeV energy is deposited across the detector in one

event. The highest energy gamma-rays from the natural background are the 2.614 MeV photons from the decay of ^{208}Tl , which is a daughter product in the decay chain of ^{232}Th existing in soil or concrete. Therefore, a high cathode threshold can separate the muon tracks from most of the natural gamma-ray background. Fig. 2.13 shows four muon tracks observed in a 3-D position-sensitive CdZnTe detector. Each cube stands for an energy deposition under a pixel. The volume of each cube represents the position uncertainty of the detector, and the color represents the energy deposited under the pixel.

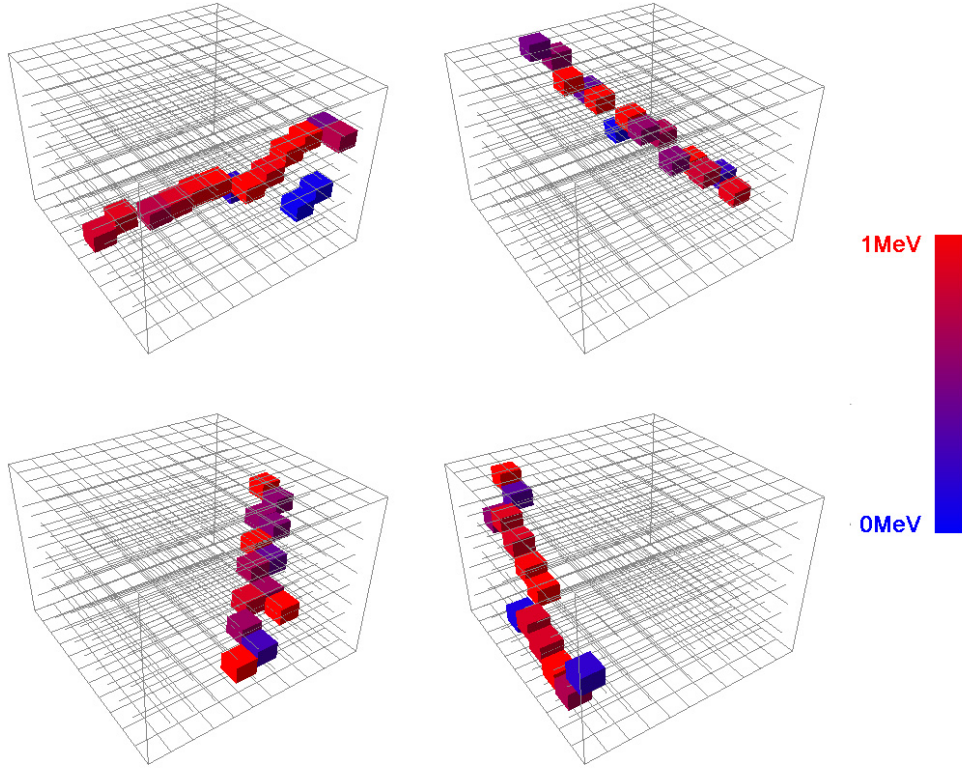


Figure 2.13: Some muon tracks observed in a 3-D position-sensitive CdZnTe detector.

For horizontal detectors, the muon flux at sea level is empirically estimated to be around $1 \text{ cm}^{-2}\text{min}^{-1}$. The overall angular distribution is proportional to $\cos^2 \theta$, in which θ is the angle between the muon direction and the zenith.

The 3-D CdZnTe detector has a dimension of $15 \text{ mm} \times 15 \text{ mm} \times 10 \text{ mm}$. The

expected count rate of muons entering the detector from the top surface is therefore 2.25 min^{-1} , which is smaller than the measured count rate of 4.2 min^{-1} . However, muons can also enter the detector from the four sides, as shown by the first muon track in Fig. 2.13. By using the $\cos^2 \theta$ approximation, the ratio of the count rates for muons to enter a vertical detector and a horizontal detector can be estimated by

$$\frac{\phi_{\perp}}{\phi_{\parallel}} = \frac{\int \int_{2\pi} \cos^2 \theta \sin \theta \sin \varphi d\Omega}{\int \int_{\pi} \cos^2 \theta \cos \theta d\Omega} = \frac{1}{4} \quad (2.6)$$

Therefore, the count rate of the muons entering the detector from the four sides is $1/4 \times 4 \times 1.5 \text{ cm}^2 \times 1 \text{ cm}^{-2} \text{ min}^{-1} = 1.5 \text{ min}^{-1}$. The total expected count rate is therefore about 3.75 min^{-1} , which is quite close to the measured rate.

The difference between the expected and the measured count rate can be caused by other high energy electromagnetic components in cosmic ray air showers such as electrons, positrons and photons. Those components are created by the decay of muons and sensitively depend on altitude.

2.4 Detector System Limitations

2.4.1 Anode Threshold

Although the anode triggering threshold can be adjusted channel by channel, the variations in the baseline and noise of each channel make the actual anode triggering amplitudes nonuniform. The current VAS3.1/TAT3 system has an anode triggering threshold of about 30 keV[45].

2.4.2 ASIC Dynamic Range

The VAS3.1/TAT3 ASIC has a dynamic range up to 1.6 MeV for each anode channel. For higher energy gamma-rays, the photons can still deposit all their energy in multiple pixel events. As a result, the detector system is capable of imaging gamma-rays with energy higher than the dynamic range of the ASIC[49]. However,

the dynamic range lowers the efficiency of imaging high energy gamma-rays because all energy depositions are required to be below the dynamic range. New ASIC under development will have a dynamic range of up to 3 MeV.

2.4.3 Charge Sharing between Neighboring Pixels

Electrons generated by a single gamma-ray interaction can be collected by two neighboring pixels. The charge sharing between two pixels is mainly due to the finite electron cloud size, the diffusion of electrons, and the x-ray emission following a photoelectric absorption. Larger pixel size can help to decrease the fraction of charge sharing events and requires fewer ASIC channels. On the other hand, a smaller pixel can provide better spectroscopic performance because it is better for single polarity charge sensing, and it has lower noise due to lower anode leakage current and capacitance. Moreover, a smaller pixel has better position resolution and can lower the probability of multiple interactions occurring under the same pixel. Du *et al.* estimated that in a 1 cm thick CdZnTe detector biased at -2000 V, the probabilities for a single interaction to be recorded as a multi-pixel event at 662 keV are 0.45 and 0.17 at pixel size of 0.5 mm and 1.5 mm, respectively[50]. Du *et al.* also suggested the pixel size to be 1.1 mm to maximize the probability of independently recording each gamma-ray interaction in the 3-D CdZnTe detector.

In Compton imaging, charge sharing events are not desired because they are not truly Compton scattered events although they are recorded as multi-pixel events. However, the charge sharing events can be distinguished from Compton scattered events by the relative positions of the two energy depositions. If the electron cloud generated by a single energy deposition is collected by two pixels, the two pixels must be neighboring to each other. Because the electrons collected by the two pixels are from the same energy deposition, they should reach the anode pixels at the same

time. Therefore, the depths of the two pixels in a charge sharing event should be very close to each other.

A Monte-Carlo simulation using Geant4[51] was performed to study the relative position distribution of two-pixel events. Unless otherwise specified, all Geant4 simulations presented in this work use a 662 keV gamma-ray flood source illuminating a $15\text{ mm} \times 15\text{ mm} \times 10\text{ mm}$ CdZnTe detector from the $15\text{ mm} \times 15\text{ mm}$ cathode side, and the electrode configuration is as shown in Fig. 2.5.

Fig. 2.14(a) and 2.14(b) respectively show the depth difference distributions for neighboring and non-neighboring two-pixel events. In the simulation, the factors causing charge sharing are not included. These factors include the electron cloud size, the x-ray emission following a photoelectric absorption, and the electron diffusion. If the two pixels are not neighboring to each other, there is no charge sharing. As a result, the measurement agrees well with the simulation. However, if the two pixels are neighboring to each other, the measurement shows that a much larger amount of the two-pixel events have depth differences less than 2 mm, while the measurement agrees with the simulation when the depth difference is greater than 2 mm. By excluding those neighboring two-pixel events with depth difference less than 2 mm, most charge sharing events can be eliminated. Although by doing so some true Compton scattered events are also excluded, the imaging performance is not affected too much because those events have poor angular resolution due to the small separation between the two interaction positions.

2.4.4 Multiple Interactions under One Pixel

Due to the finite size of the anode pixels, it is possible that the incident gamma-ray interacts two or more times under the same pixel. Because the current system can only provide one trigger from one pixel, the multiple interactions are recorded as a

single interaction. For single pixel events, the depth is obtained by C/A ratio, which is proportional to the centroid depth of the two interactions. However, for multiple pixel events, the depth is obtained by the electron drift time. Since the anode pixel is triggered by the first group of electrons arriving at the anode, the measured depth is the interaction closer to the anode side. Because the other group of electrons away from the anode side suffer more trapping, the corrected energy is smaller than the true total energy deposited. As a result, for those multiple pixel events with two or more interactions under the same pixel, both the energy and position information are incorrect.

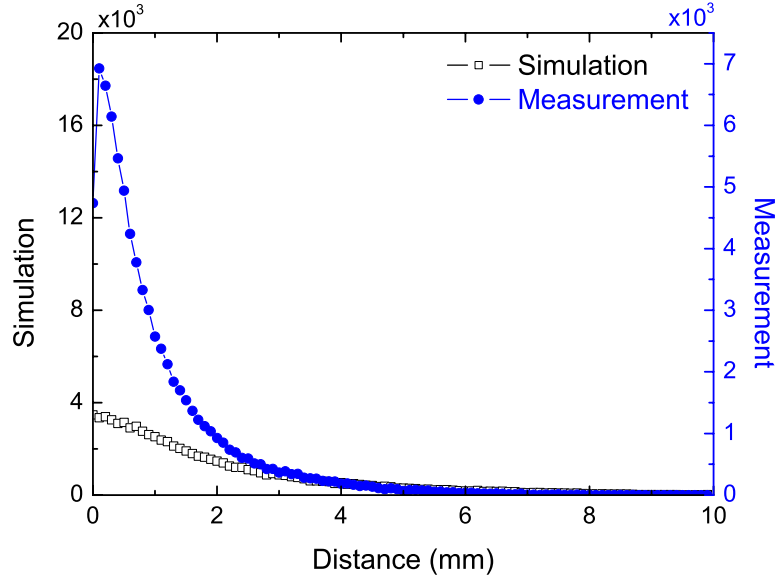
Table 2.1 shows the simulation results of multiple interactions under one pixel at 662 keV. In the Geant4 simulation, x-ray emissions are not included since those x-rays deposit their energy very close to the initial photoelectric absorption positions. As we can see, about 20% of the photopeak events have multiple interactions under the same pixel. This number increases as the gamma-ray energy and detector pixel size increase.

Table 2.1: Simulated Multiple Interactions under One Pixel Anode at 662 keV (Pixel Sharing)

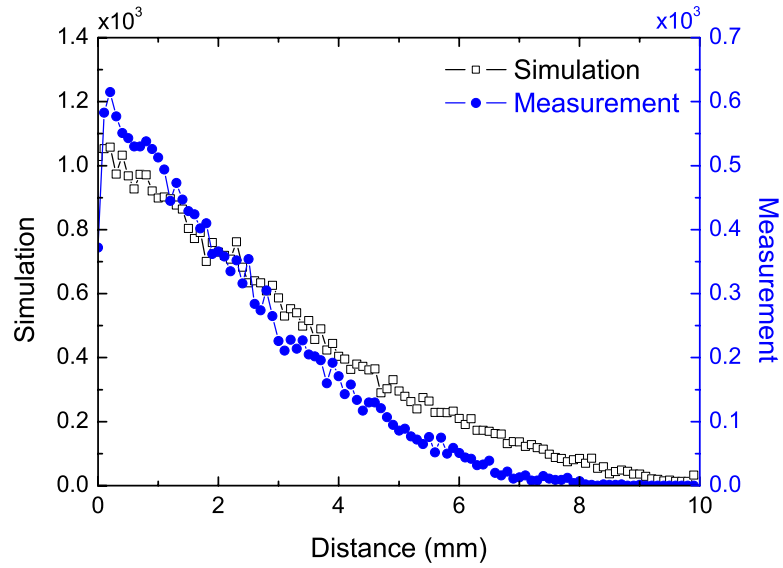
	Photopeak Efficiency	Percentage of Pixel Sharing Events
Single-pixel	4.77%	19.0%
Two-pixel	4.55%	19.9%
Three-pixel	1.61%	20.2%
Four-pixel	0.23%	20.5%
Total	11.2%	19.6%

Fig. 2.15 shows the depth difference distribution of the pixel sharing photopeak events. The quick drop of the distribution as the depth difference increases can be explained by the fact that the solid angle under the same pixel decreases quickly as the distance increases. Therefore, as the scattered photon travels longer distance,

it is more likely to leave the pixel volume. The average distance is about 0.6 mm, which is only slightly larger than the depth uncertainty measured by the electron drift time. As a result, although as many as 20% of the photopeak events have multiple interactions under the same pixel, the effect introduced by those events to energy correction and Compton imaging is very small.



(a) Neighboring two-pixel events.



(b) Non-neighboring two-pixel events.

Figure 2.14: Depth difference distribution of neighboring and non-neighboring two-pixel photopeak events at 662 keV.

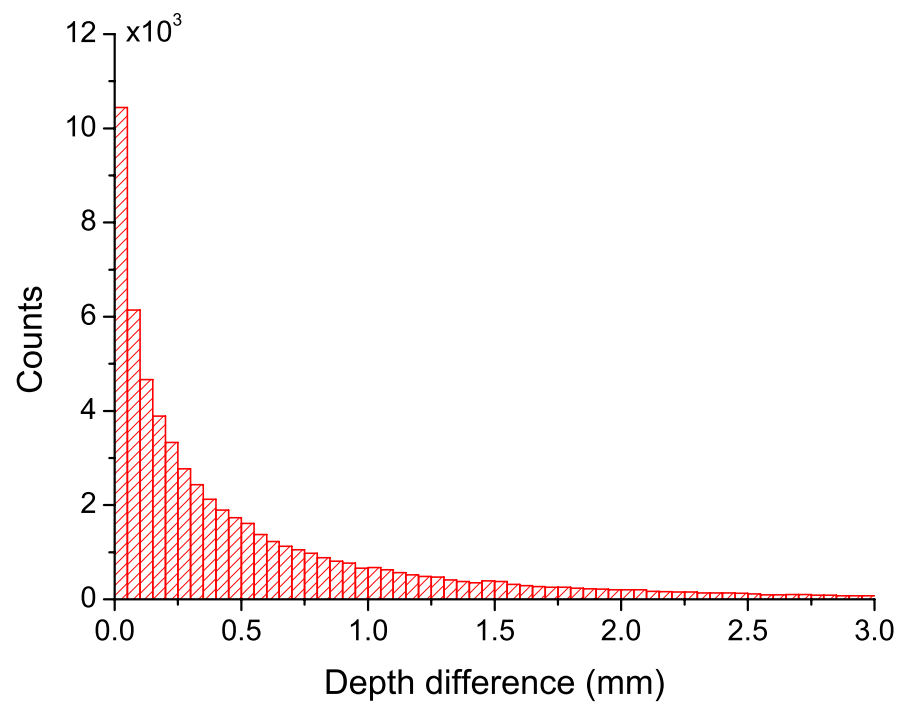


Figure 2.15: Depth difference distribution between two interactions under the same pixel.

CHAPTER III

SEQUENCE RECONSTRUCTION

Because of the small size of 3-D position-sensitive CdZnTe detectors, the separation distance between interactions is short. The poor timing resolution of the detector does not allow direct time-of-flight measurement to determine the interaction sequence. As a result, if an N -pixel event is recorded, there are $N!$ possible sequences. The sequence reconstruction is to select the most probable sequence among all the possible sequences. For image reconstruction algorithms such as the simple back-projection algorithm or the filtered back-projection algorithm, the sequence reconstruction is helpful to improve the signal-to-noise ratio and the image resolution. As this work is mostly focused on imaging with two-pixel events, only the sequence reconstruction methods for two-pixel events are discussed. If a gamma-ray does not deposit all its energy in a two-pixel event, the incident gamma-ray energy can only be assumed to be the sum of the two deposited energies if the initial energy is unknown. In this case, the reconstructed back-projection cone does not pass the source direction even with the correct sequence. As a result, the sequence reconstruction is less important for partial energy deposition events. Therefore, this chapter only discusses the sequence reconstruction methods for full-energy two-pixel events.

3.1 Simple Comparison Method

Although the measurement can not give the interaction sequence, the kinematics of Compton scattering can provide some information to determine the correct sequence. From the Compton scattering formula of Eq. 1.1, we know that the energy deposited in a Compton scattering event is maximum when the scattering angle is at 180° . The maximum deposited energy in the first scattering is

$$\max(E_1) = E_0 - E'|_{\theta=180^\circ} = \frac{E_0}{1 + m_e c^2 / (2E_0)} \quad (3.1)$$

in which E_1 is the energy deposited in a Compton scattering event.

In gamma-ray spectroscopy, $\max(E_1)$ is the Compton edge in a typical gamma-ray spectrum. A gamma-ray can not deposit more energy than the Compton edge in a Compton scattering. In other words, the first interaction of a two-pixel event must be a Compton scattering and its energy deposition must be less than the Compton edge. Therefore, if one of the energy depositions in a two-pixel event is greater than the Compton edge, the sequence can be determined by setting the other energy deposition as the first interaction. This is called the Compton edge test.

Lehner proposed a sequence reconstruction method for two-pixel events by simply comparing the energies deposited[30, 49]. When the incident gamma-ray energy is above 400 keV, the interaction with the higher energy deposition was selected as the first interaction. After that, the Compton edge test is applied. If the sequence fails the Compton edge test, either the sequence order is incorrect or the full energy is not deposited in the two interactions. In both cases, this event is rejected. As we can see, although this method can eliminate some partial-energy events, it also rejects some full-energy events which could be correctly identified because the Compton edge test denies one possible sequence and leaves the other sequence as the only

choice. Therefore, in this study, the sequence reconstruction is performed by doing the Compton edge test before the energy comparison. By this way, the probability of correctly identifying the sequence of a two-pixel event is maximized.

When the incident gamma-ray energy is below $m_e c^2/2$, the Compton edge is less than $E_0/2$ from Eq. 3.1. As a result, if the second interaction is a photoelectric absorption and the full energy of the incident gamma-ray is deposited, the energy deposition of the first interaction, which is a Compton scattering, is always less than $E_0/2$, and the energy deposition of the second interaction, which is a photoelectric absorption, is always greater than $E_0/2$. Therefore, the sequences of incident gamma-rays with energy less than $m_e c^2/2$ can be always correctly reconstructed by selecting the smaller energy deposition as the first interaction.

For incident gamma-rays with energy greater than $m_e c^2/2$, there is possibility that both interactions deposit energies less than the Compton edge for full-energy deposition events. In fact, only those events with scattering angles less than ω_1 can be identified by the Compton edge test, where ω_1 is defined by

$$\cos \omega_1 = 1 - \frac{(m_e c^2)^2}{2E_0^2} \quad (3.2)$$

Another angle ω_2 , at which the incident gamma-ray deposits half of its energy in the Compton scattering, is defined by

$$\cos \omega_2 = 1 - \frac{m_e c^2}{E_0} \quad (3.3)$$

For incident gamma-rays with energy greater than $m_e c^2/2$, we have the relationship of $0 < \omega_1 < \omega_2 < \pi$. We can divide the two-pixel events into three groups:

1. Events with scattering angles between 0 and ω_1 . These events can always be identified by the Compton edge test. The energy deposition in the first interaction is less than the second interaction.

2. Events with scattering angles between ω_1 and ω_2 . The energy deposition in the first interaction is the lower of the two.
3. Events with scattering angles between ω_2 and π . The energy deposition in the second interaction is the lower.

Geant4 simulations were run to study the fractions of full-energy two-pixel events in the three groups as a function of the incident gamma-ray energy. The result is shown in Fig. 3.1. In the simulations, the incident gamma-ray directions were randomly simulated in a parallel beam with radius of 1.2 cm, which is large enough for the beam to cover the whole detector from any direction. The direction of the beam is uniformly sampled in 4π . As a result, the numbers in Fig. 3.1 do not represent the intrinsic photopeak efficiencies of two-pixel events. For pixel sharing events, the pixel with the first interaction was set as the first pixel. Since there are multiple interactions under the same pixel, it is possible that the energy deposition under the first pixel is larger than the Compton edge. These events do not belong to any of the three groups and will be incorrectly sequenced. As a result, the sum of the counts of the three groups is slightly smaller than the total number of counts.

As we can see in Fig. 3.1, when the incident gamma-ray energy is less than $m_e c^2/2$, almost all two-pixel events can be correctly sequenced by the Compton edge test. When the gamma-ray energy is greater than $m_e c^2/2$, for those events in group 2 and group 3, which can not be sequenced by the Compton edge test, group 3 has more counts than group 2 at all energies. This means that for those events that can not be identified by the Compton edge test, the probability for the first interaction to deposit more energy is always higher than the second interaction, and this probability increases as the incident gamma-ray energy increases.

The simple comparison method is therefore stated as

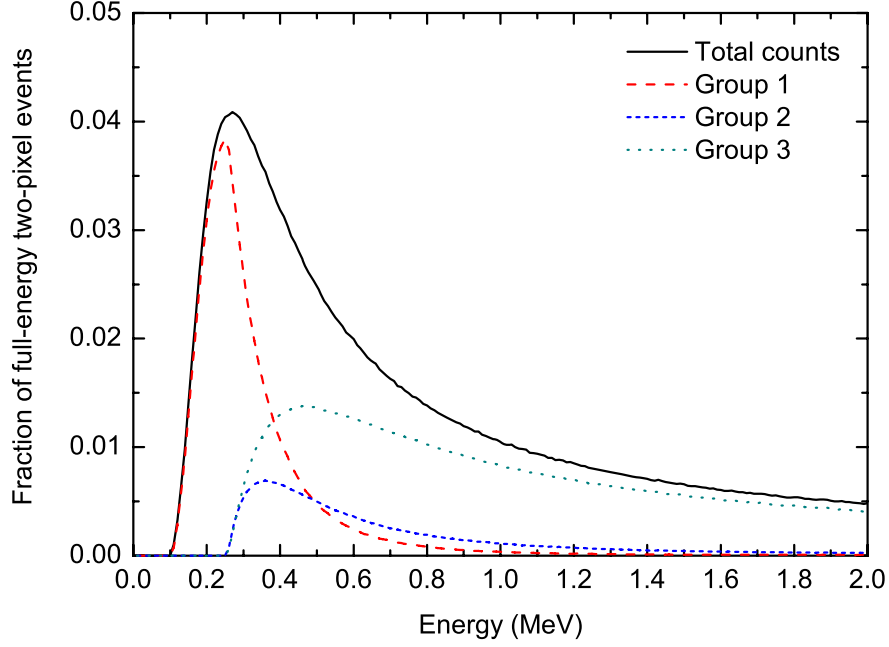


Figure 3.1: Fractions of full-energy two-pixel events in the three different groups as a function of the incident gamma-ray energy.

1. If one of the two interactions deposits more energy than the Compton edge, the interaction with the smaller energy deposition is selected as the first interaction.
2. Otherwise, the interaction with the larger energy deposition is selected as the first interaction.

With this method, all the events in group 1 and group 3 are correctly sequenced, and the events in group 2 are incorrectly sequenced. The overall efficiency of the simple comparison method is shown in Fig. 3.2. The method is the least efficient at energy around 400 keV. The high efficiency at the low energy end is because most of the events can be correctly sequenced by the Compton edge test. The higher efficiency at the high energy end is because more events deposit higher energies in the first interaction.

The results shown in Fig. 3.1 is for a $15 \text{ mm} \times 15 \text{ mm} \times 10 \text{ mm}$ 3-D CdZnTe detector. If the size of the detector increases, the fractions of the two-pixel events in

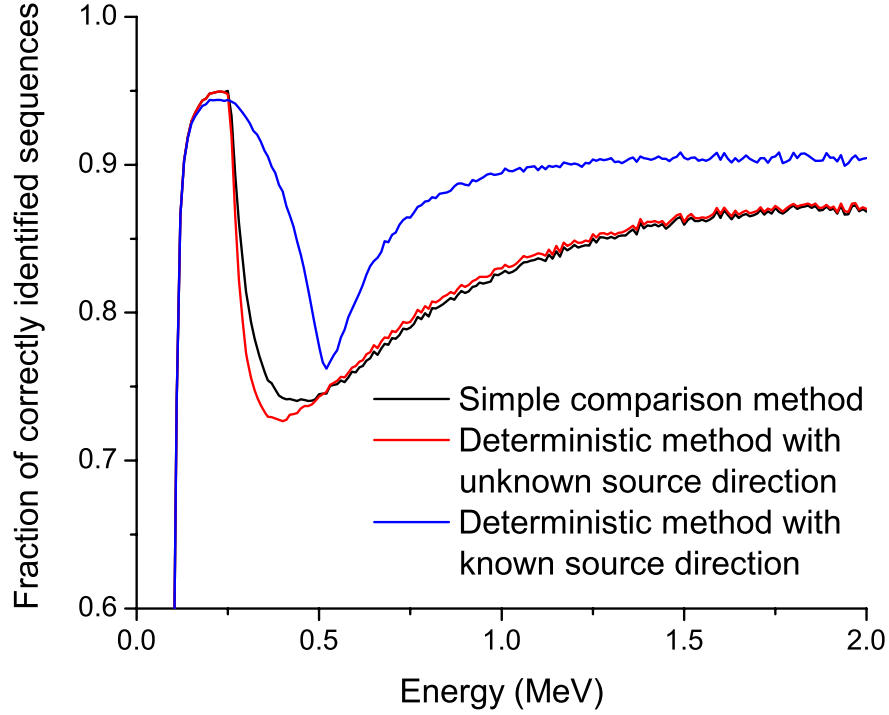


Figure 3.2: Fraction of simulated full-energy two-pixel events which are correctly sequenced by the simple comparison method and the deterministic method.

the three groups can change. In a real detector, the measured Compton scattering angle distribution usually differs from the prediction given by the Klein-Nishina formula (see Section 5.2.4). Because the back scattered photons have less energy than the forward scattered photons, those back scattered photons are easier to be captured. Therefore, the measured scattering angle distribution favors those large angle scattering events. As the detector size increases, more small angle scattering events will be captured and the measured scattering angle distribution will be closer to the prediction given by the Klein-Nishina formula. However, as shown in Fig. 3.3, even with the theoretical prediction given by the Klein-Nishina formula, a Compton scattering is more probable to fall in group 3 than group 2. As a result, the simple comparison method can also be applied to a CdZnTe detector larger than $15 \text{ mm} \times 15 \text{ mm} \times 10 \text{ mm}$.

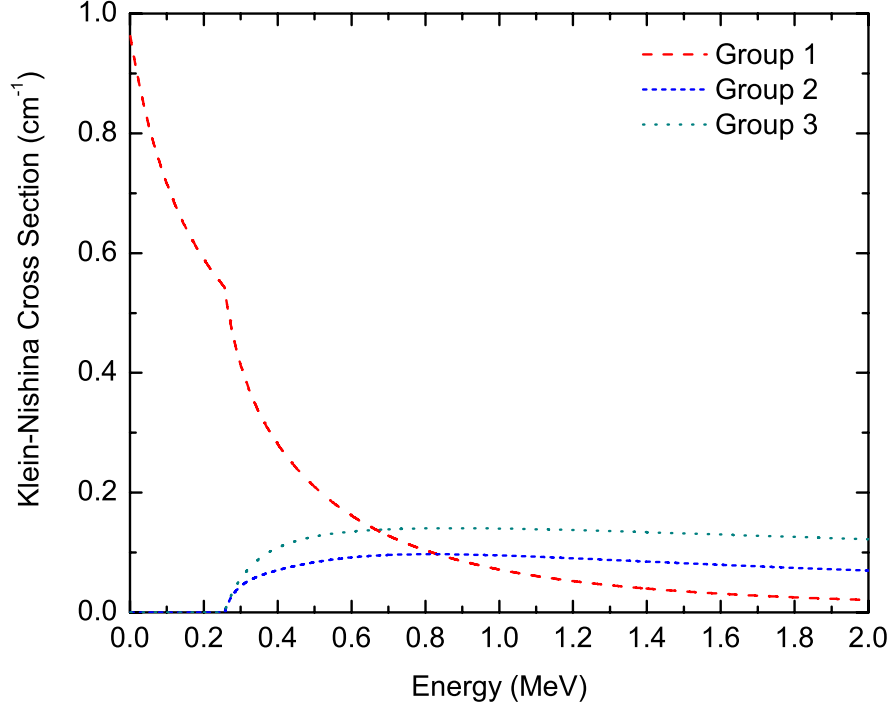


Figure 3.3: Klein-Nishina cross section in the three different groups as a function of the incident gamma-ray energy. When the incident gamma-ray energy is less than $m_e c^2/2$, all scattering events fall in group 1, which can be correctly sequenced by the Compton edge test.

3.2 Deterministic Method

The deterministic method simply chooses the sequence with the higher probability. Kroeger described a deterministic method to determine the sequence of three measured interactions[25]. For two-pixel events, the deterministic method is even simpler. The probability for an incident photon to create a two-pixel event with sequence of $(E_1, \mathbf{r}_1) \rightarrow (E_2, \mathbf{r}_2)$ can be expressed as

$$\begin{aligned}
 & \Pr\{\text{An incident photon creates a two-pixel event with sequence of } (E_1, \mathbf{r}_1) \rightarrow (E_2, \mathbf{r}_2)\} \\
 &= \Pr\{\text{The incident photon reaches } \mathbf{r}_1\} \\
 &\quad \cdot \Pr\{\text{The incident photon is scattered and deposits } E_1\} \\
 &\quad \cdot \Pr\{\text{The scattered photon reaches } \mathbf{r}_2\} \\
 &\quad \cdot \Pr\{\text{The scattered photon is photoelectric absorbed}\}
 \end{aligned} \tag{3.4}$$

The system response function developed in Chap. VI gives the probability of each sequence. Specifically, Eq. 6.28 gives the probability for a incident photon to deposit its full energy in a two-pixel event. The deterministic method uses Eq. 6.28 to calculate the probability of each sequence and chooses the sequence with the higher probability. The efficiency of the deterministic method is shown in Fig. 3.2.

Although the deterministic method is considered to be a better method because it uses a more complete model than the simple comparison method, it can be seen that the efficiencies of the two methods are almost identical at all energies. While the simple comparison method only uses the information provided by the deposited energies in the two interactions, the deterministic method takes advantage of the interaction position information as well. In other words, the simple comparison method only accounts for the scattering and absorption probabilities in Eq. 3.4, but the deterministic method also accounts for the attenuation probabilities. Because of the small size of the detector, there is not much difference between the attenuation probabilities for both sequences, especially for gamma-rays with energy of several hundred keVs. For example, if $E_1 = 400$ keV, $E_2 = 800$ keV, and $|\mathbf{r}_1 - \mathbf{r}_2| = 5$ mm, the ratio between the attenuation probabilities of the two sequences is only 1.13. Considering that for a $15\text{ mm} \times 15\text{ mm} \times 10\text{ mm}$ CdZnTe detector, the average separation distance between two-pixel events is only a few millimeters, the actual contribution of the position information to the sequence determination is even smaller. The deterministic method is expected to have a better performance for larger detectors.

3.3 Deterministic Method with Known Source Direction

The above discussion of the sequence reconstruction methods is based on the assumption that there is no a priori information about the source direction. As a

fact, the probability of Eq. 3.4 is the sum of the system response function (Eq. 6.28) over all source directions. However, since the system response function gives the probability of a gamma-ray from a specific direction to create the measured two-pixel event, the deterministic method performs better if the direction of the incident photons is known. The method examines the angle between the known source direction and the back-projection cone of each sequence, and gives more weight to the sequence with the back-projection cone closer to the source direction.

The efficiency of the deterministic method with known source direction is also shown in Fig. 3.2. It can be seen that the efficiency is improved over almost all the energy range.

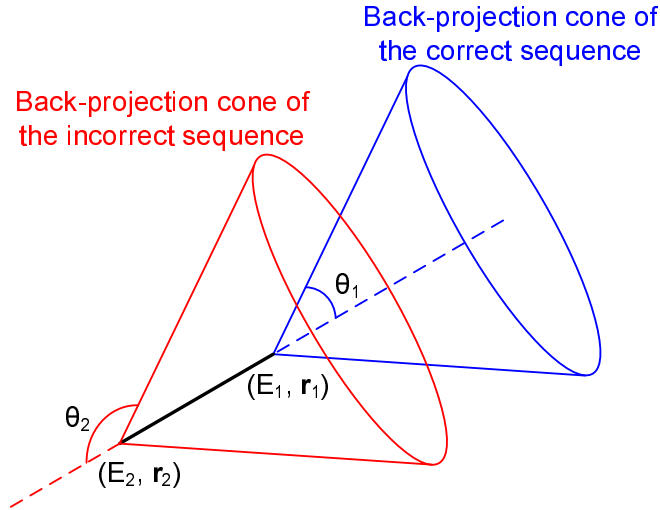


Figure 3.4: The two back-projection cones of a two-pixel event. The correct sequence is $(E_1, \mathbf{r}_1) \rightarrow (E_2, \mathbf{r}_2)$. In far field imaging, the two back-projection cones overlap with each other when $\theta_1 + \theta_2 = 180^\circ$.

As illustrated in Fig. 3.4, when the calculated scattering angles of the two possible sequences add up to 180° exactly, the two back-projection cones are identical if the separation between the two interactions can be neglected (far field imaging). In this case, the known source direction does not help in determining which sequence is more probable. The average difference between $\theta_1 + \theta_2$ and 180° as a function of the

incident gamma-ray energy is calculated by simulations, and the result is shown in Fig. 3.5. As we can see, the difference between $\theta_1 + \theta_2$ and 180° is the smallest when the incident gamma-ray energy is around 511keV. Therefore, the a priori knowledge of the source direction has the least effect in improving the sequence identification around 511 keV.

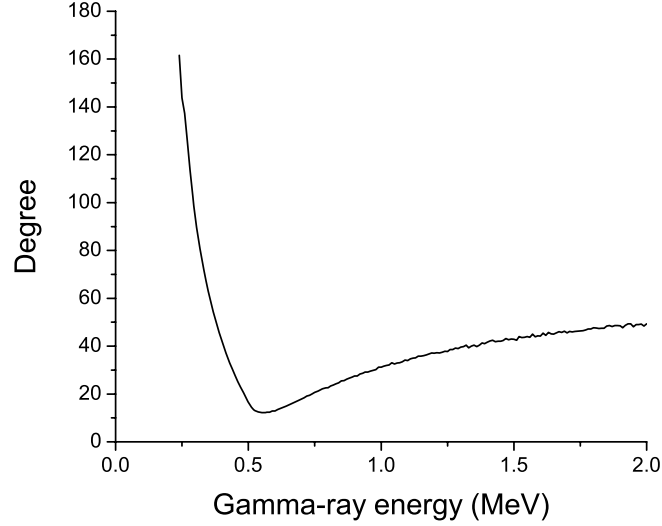


Figure 3.5: The average difference between $\theta_1 + \theta_2$ and 180° , $E(|\theta_1 + \theta_2 - 180^\circ|)$, is calculated by simulations. The full energy two-pixel events that can not be identified by the Compton edge test were used. When the gamma-ray energy is below $m_e c^2/2$, all full energy two-pixel events can be correctly identified by energy depositions.

If there is a priori knowledge that the source is a point source, a quick simple back-projection can be first applied to identify the source direction, which can be used to improve the sequencing efficiency in the next image reconstruction. However, if there are other sources at different directions, the sequencing efficiency for gamma-rays from those sources is artificially degraded. Therefore, this method should be used with great care in practice.

In summary, the deterministic method shows little advantage over the simple comparison method when the detector size is small. Therefore, the simple comparison method is used throughout this work whenever the sequence reconstruction is neces-

sary. With larger detector size or detector arrays, the deterministic method will be more efficient at identifying the correct sequence.

CHAPTER IV

ANGULAR UNCERTAINTIES

Compton imaging requires the intersection of many back-projection rings to form the source image. The imaging concept itself already introduces an uncertainty in the reconstructed image because only a small portion of each back-projection ring passes through the true source location. This effect is usually referred to as “Compton ring effect”, which can be removed by applying certain reconstruction algorithms such as Filtered Back-Projection algorithm(FBP). In addition to the Compton ring effect intrinsic to Compton imagers, there are other factors causing the uncertainty in the reconstructed image due to the imperfection of the detector system and natures of Compton scattering. Those factors include the position and the energy uncertainties of the detector, Doppler broadening, and coherent(or Rayleigh) scattering. This chapter discusses those factors and compares their contributions to the angular resolution of the reconstructed image.

4.1 Angular Resolution Measurement

Because of the detector uncertainties, the back-projection cone reconstructed from the measured data often does not pass the actual source direction. A Compton camera’s angular resolution is usually described in terms of the Angular Resolution Measurement(ARM), which is the angle between the reconstructed back-projection cone

and the actual source direction. Sometimes the ARM is also referred to as Angular Resolution Metric. As shown in Fig. 4.1, a gamma-ray from the source deposits energy E_1 at position \mathbf{r}_1 in a Compton scattering, and deposits energy E_2 at position \mathbf{r}_2 . Because of the position and the energy uncertainties, the measurement gives the values of $(E_{1m}, \mathbf{r}_{1m})$ and $(E_{2m}, \mathbf{r}_{2m})$ respectively. As a result, the back-projection cone does not pass the true source direction. The ARM is the difference between θ_r and θ_e , in which, θ_r is calculated from the measured interaction positions and the true source location, and θ_e is calculated from the measured energy depositions by the Compton scattering formula. θ_r and θ_e can be obtained by

$$\theta_r = \cos^{-1} \frac{(\mathbf{r}_{1m} - \mathbf{r}_0) \cdot (\mathbf{r}_{2m} - \mathbf{r}_{1m})}{|\mathbf{r}_{1m} - \mathbf{r}_0| |\mathbf{r}_{2m} - \mathbf{r}_{1m}|} \quad (4.1)$$

and

$$\theta_e = \cos^{-1} \left(1 + \frac{m_e c^2}{E_{1m} + E_{2m}} - \frac{m_e c^2}{E_{2m}} \right) \quad (4.2)$$

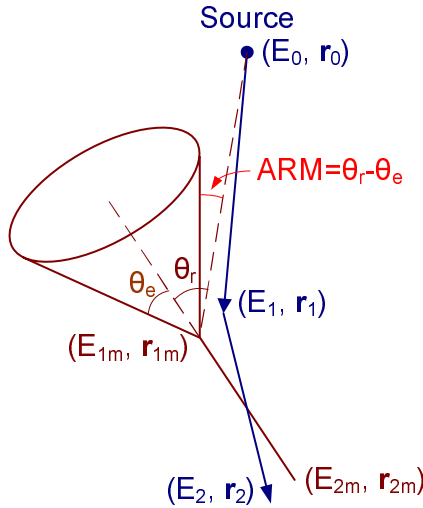


Figure 4.1: The Angular Resolution Measurement.

There are two assumptions in Eq. 4.2. The first assumption is that the incident gamma-ray energy is unknown, and the second assumption is that the gamma-ray deposits all its energy in the two interactions. If the incident gamma-ray energy is

known, the Compton scattering angle will then be independent of E_{2m} . The two assumptions applied to Eq. 4.2 are adopted throughout this chapter.

4.2 Factors Contributing to the ARM

There are several factors contributing to the ARM, including the position and the energy uncertainties of the detector, Doppler broadening, and coherent scattering. Geant4[51] simulations were run to study their contributions to the ARM. In the simulations, a point source was placed 50 cm away from the cathode. Each ARM contribution factor was included into the simulations separately, so that those factors can be studied individually.

In the study of the ARM distribution caused by a certain factor, the ARM distribution varies in different event groups. For example, if the distances between the two interaction positions are different, the ARM distribution caused by the position uncertainties can be different. Different scattering angles can also result in different ARM distributions when considering the energy uncertainty and the Doppler broadening effect. In actual reconstruction, the angular resolution can be improved by selecting those events with large distance separation or with certain scattering angle at the expense of efficiency. In this section, only the overall ARM distributions are studied to estimate the most dominating factors in determining the angular resolution of a single $15\text{ mm} \times 15\text{ mm} \times 10\text{ mm}$ 3-D CdZnTe detector.

4.2.1 Detector Position Uncertainties

Because of the finite size of the anode pixels and the finite timing resolution, the 3-D position-sensitive CdZnTe detector has position uncertainties of 1.3 mm in lateral coordinates and 0.4 mm FWHM in depth for multiple-pixel events[45]. In the simulation, if a gamma-ray deposits energy under a pixel, the pixel center was

used as the lateral position of the interaction. A Gaussian uncertainty with 0.4 mm FWHM was added to the actual interaction depth to give the measured interaction depth. The true deposited energies were used to calculate the Compton scattering angle. The ARM distribution of two-pixel photopeak events at 662 keV is shown in Fig. 4.2. The standard deviation of the ARM distribution is 12.4° .

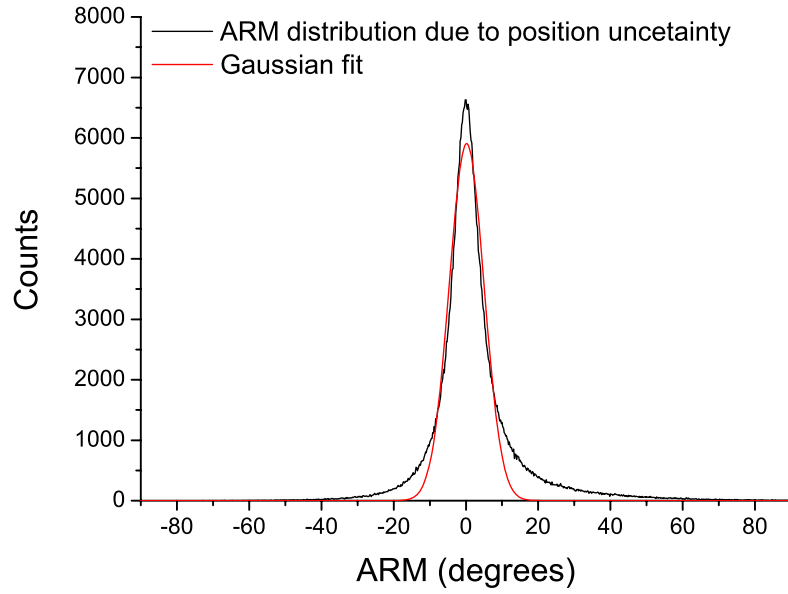


Figure 4.2: The ARM distribution of two-pixel photopeak events at 662 keV due to the detector position uncertainties.

It can be seen that the ARM distribution does not strictly follow a Gaussian distribution, and there is some asymmetry in the distribution. The non-gaussian shape is mostly due to the fact that this distribution is the superposition of the ARM distributions from the events with different distance separations.

4.2.2 Detector Energy Uncertainties

In most gamma-ray detectors, the overall energy resolution can be modeled by the quadrature sum of the electronic noise, the statistical fluctuation, and other noises,

as shown by

$$\text{FWHM}_{\text{overall}}^2 = \text{FWHM}_{\text{noise}}^2 + \text{FWHM}_{\text{statistical}}^2 + \text{FWHM}_{\text{drift}}^2 + \dots \quad (4.3)$$

The statistical fluctuation in semiconductors is usually modeled as[52]

$$\text{FWHM}_{\text{statistical}} = 2.35\sqrt{F \cdot E \cdot W} \quad (4.4)$$

in which, F is the Fano factor, E is the gamma-ray energy, and W is the average ionization energy. In CdZnTe, W is typically 5 eV.

In semiconductor materials, the Fano factor is usually less than one, and the measured value for CdZnTe is around 0.1[53]. However, in the 3-D position-sensitive CdZnTe detector, many other statistical factors can contribute to the energy resolution, such as the depth uncertainty and electron trapping. As a result, the measured energy resolution depends more on the statistical contributions. Therefore, although the variance in the number of generated charge carriers is only 0.1 of the Poisson predicted variance, the overall signal variance due to statistics is high. To account for this effect, based on the measured resolutions at different gamma-ray energies, a Fano factor of unity was assumed in the simulations. The electronic noise was set to 5 keV based on the measurement results. Therefore, the FWHM at energy E is

$$\text{FWHM}_{\text{overall}} = \sqrt{25 + 2.35^2 F \cdot E \cdot W} (keV) \quad (4.5)$$

which corresponds to about 1% FWHM at 662 keV as observed in experiments.

Fig. 4.3 shows the ARM distribution caused by the detector energy uncertainty. The ARM distribution has a standard deviation of 2.03° . The non-Gaussian shape is also evident in the distribution. Similar to the reason causing the non-Gaussian shape in the ARM distribution in Fig. 4.2, the non-Gaussian shape is due to the different ARM variances in events with different scattering angles. Fig. 4.4 shows the

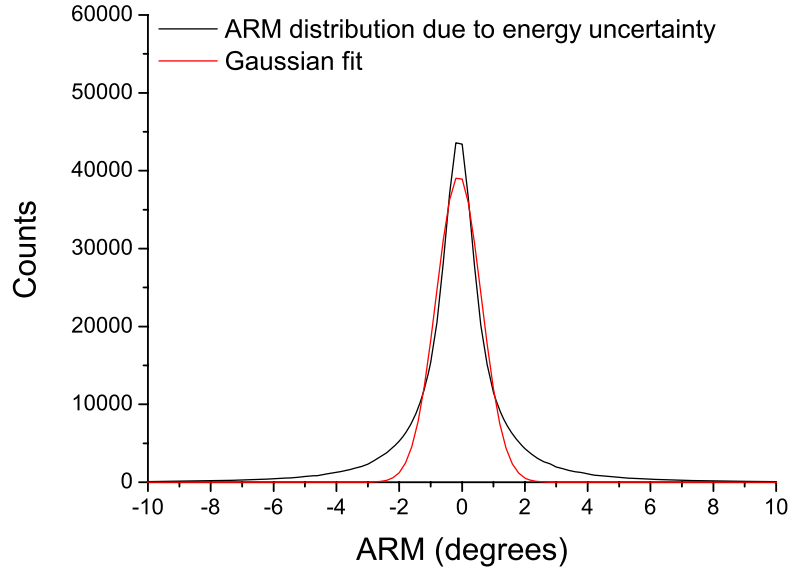


Figure 4.3: The ARM distribution of two-pixel photopeak events at 662 keV due to the detector energy uncertainty.

ARM distribution of those events with scattering angles of $90^\circ \pm 2.5^\circ$. It can be seen that for those events with fixed scattering angle, a Gaussian model can describe the ARM distribution very well. However, since events with different scattering angles have different ARM distributions, the superimposed total ARM distribution exhibits a non-Gaussian shape. For individual events, a Gaussian model is adequate to model the angular uncertainty.

4.2.3 Doppler Broadening

The Compton scattering formula (Eq. 1.1) is based on the assumption that the initial electron is at rest. In reality, electrons in atoms have momenta, which introduce uncertainties in the scatters. As a result, the energy of the scattered photon at a specific scattering angle shows some distribution around the value predicted by the Compton scattering formula. The effect is called Doppler broadening.

In the Geant simulations, the Penelope model[54] was applied to take into ac-

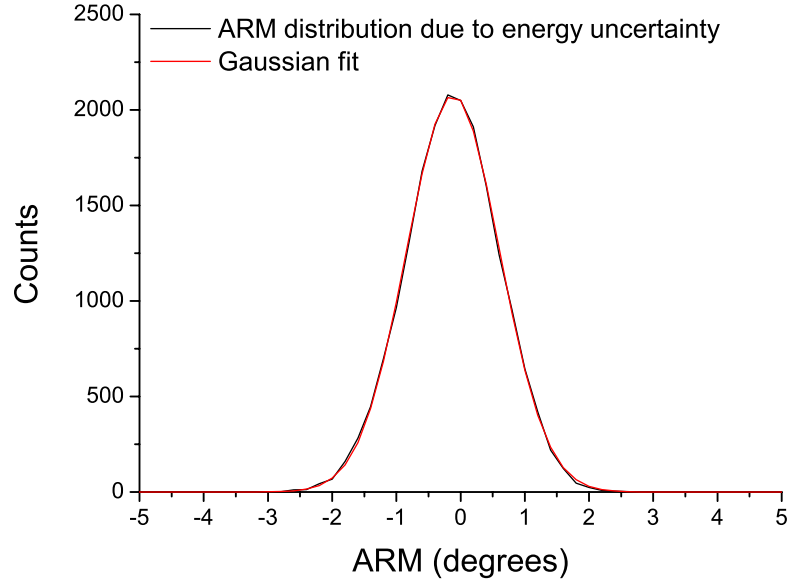


Figure 4.4: The ARM distribution of two-pixel photopeak events at 662 keV due to the detector energy uncertainty. The scattering angles of those events are within $90^\circ \pm 2.5^\circ$.

count Doppler broadening and the binding energy of electrons. In the Penelope model, scatters with bound electrons are only allowed when the transferred energy is greater than the ionization energy of the electrons. The binding effect affects the ARM distribution very little because it only impacts those scatters with very small scattering angles, which are only a small portion of the total cross section. Therefore, the ARM distribution simulated by the Penelope model is mainly due to the Doppler broadening effect. Fig. 4.5 shows the simulated ARM distribution due to Doppler broadening. The distribution shows a standard deviation of 8.43° .

Doppler broadening is related to the distribution of the electron momentum, which is broader in materials with high atomic numbers. As a result, Doppler broadening is the most severe in high Z materials. This is the reason why researchers prefer silicon as the first detector in designs of high resolution Compton cameras, although efficiency is sacrificed. In CdZnTe detector, due to the relative high atomic number,

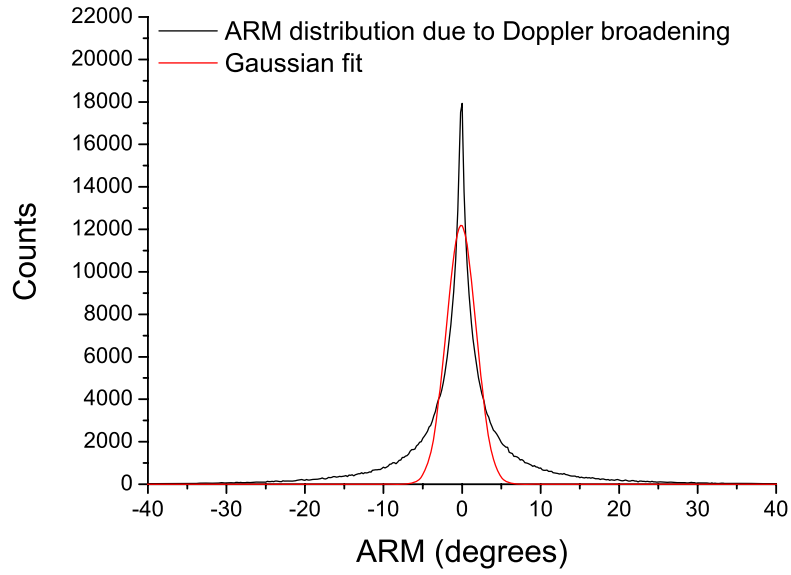


Figure 4.5: The ARM distribution of two-pixel photopeak events at 662 keV due to Doppler broadening.

Doppler broadening can be an important factor limiting the angular resolution.

4.2.4 Coherent Scattering

In a coherent scattering (also known as Rayleigh or Thomson scattering), the incident photon interacts with the whole atom in a way that the photon changes its direction without losing its energy. If a coherent scattering occurs before the first Compton scattering or between the Compton scattering and the photoelectric absorption, the reconstruction cone will be displaced. Fig. 1.3 indicates that in CdZnTe detectors, coherent scattering is more important than Compton scattering when the gamma-ray energy is below 100 keV. But as the gamma-ray energy increases, the coherent scattering cross section decreases quickly. In the imaging energy range from 300 keV to several MeV for the CdZnTe detector, coherent scattering is unlikely to happen before the first interaction. However, the incident gamma-rays can be Compton scattered into lower energies, at which coherent scattering becomes more

common. Meanwhile, the photoelectric effect also becomes important at low energies and its cross section is usually one order of magnitude higher than that of coherent scattering. Therefore, only a small portion of the scattered photons will be coherent scattered before being photoelectric absorbed. Fig. 4.6 shows the fraction of two-pixel photopeak events in which a coherent scattering occurs before the incident gamma-ray is fully absorbed. At 662 keV, only about 3.5% two-pixel photopeak events involve coherent scattering.

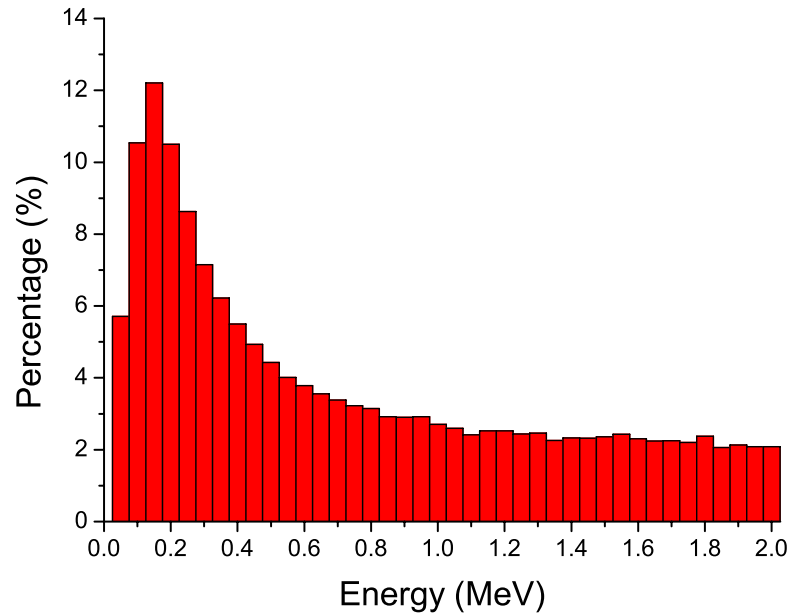


Figure 4.6: Percentage of two-pixel photopeak events that are coherent scattered before the gamma-rays are fully stopped.

Fig. 4.7 shows the ARM distribution of those two-pixel photopeak events which involve coherent scattering at 662 keV. The standard deviation of the distribution is 9.76° . However, those coherent scattered events are only a small fraction of the total events. For those events that are not coherent scattered, the ARM is zero since no other ARM contribution factors are considered. The overall standard deviation of

the ARM distribution including all events is only 1.84° .

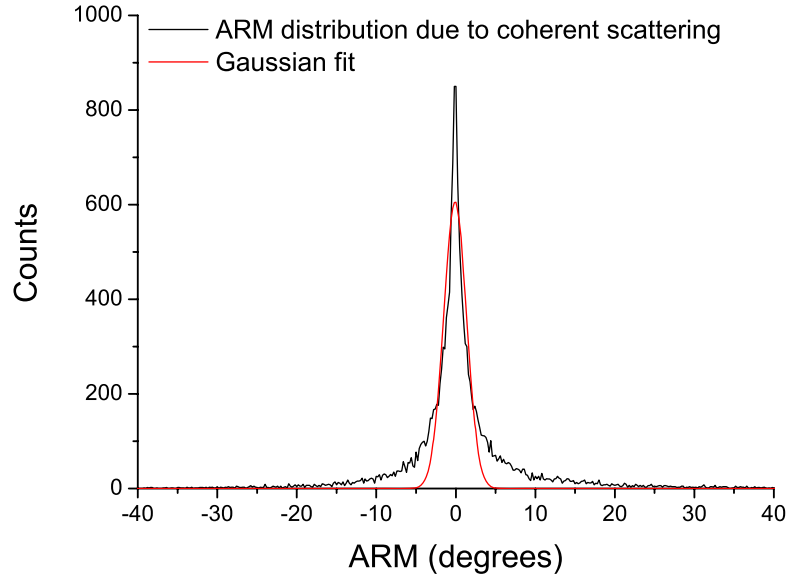


Figure 4.7: The ARM distribution of two-pixel photopeak events at 662 keV that are coherent scattered before the gamma-rays are fully stopped.

4.2.5 Comparison of the Factors Contributing to the ARM

The standard deviations of the ARM distributions due to the above four factors are shown in Fig. 4.8. Only two-pixel full-energy deposition events are considered. Although pair production becomes possible when the gamma-ray energy is greater than 1.022 MeV, it does not affect the results presented in Fig. 4.8 due to the fact that if a pair production occurs and the full energy is deposited, the event must be an at least three-pixel event.

It can be seen that the main contributors to the ARM distribution are the position uncertainties and Doppler broadening effect. The energy uncertainty and coherent scattering only have a trivial effect. Fig. 4.8 also shows that when the gamma-ray energy is above 500 keV, almost all the ARM uncertainties caused by different factors settle down to constants, which means the increase of the energy does not help

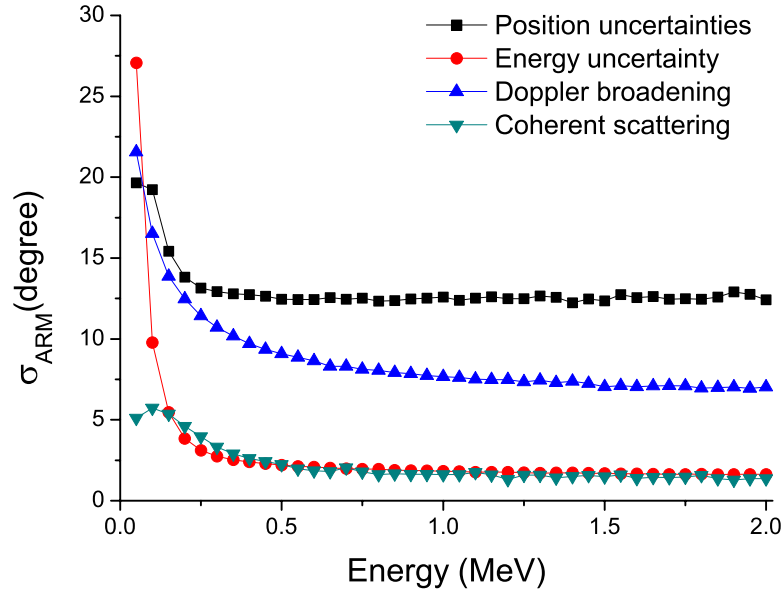


Figure 4.8: The standard deviations of the overall ARM distributions at different incident gamma-ray energies.

to improve the angular uncertainty. For higher energy gamma-rays, the scattered photons can travel more distance thus the ARM uncertainty caused by the position uncertainties seems to be improved. However, due to the small size of the detector, increasing gamma-ray energy does not necessarily mean an increase of the average distance between the two interactions. Therefore, the energy increase does not help to improve the ARM uncertainty caused by the position uncertainties.

However, the ARM is only one of the many aspects determining the final angular resolution of the image. In the simulations described in this section, the correct interaction sequences are used. In reality, due to the poor timing resolution of the system, the interaction sequence has ambiguity and must be determined based on the energy information. As the incident gamma-ray energy increases, the interaction sequence can be more accurately identified. Moreover, the Compton ring effect can be different at different energies since the scattering angle distribution could be different.

Therefore, the final angular resolution of the reconstructed image still depends on the incident gamma-ray energy. The ARM distribution helps to determine the width and shape of the back-projection rings.

The ARM distribution studied in this section is the overall ARM distribution of all two-pixel full-energy events in a single $15\text{mm} \times 15\text{mm} \times 10\text{mm}$ 3-D CdZnTe detector. If the detector system configuration is changed, the overall ARM distribution will also be changed. The ARM distribution caused by the position uncertainties depends on the separation between the two interactions, and the ARM distributions caused by other factors depend on the scattering angle.

In image reconstruction processes, the ARM distribution must be modeled so that it can be calculated event by event. The models can be established either numerically or analytically. Numerical solutions obtained by simulations can be daunting due to the large number of possible measurement outputs. Moreover, analytical models are tempting because they can be applied to different detector configurations. The next section discusses analytical models for different ARM contributors.

4.3 Modeling of Angular Uncertainties

Fig. 4.8 indicates the main contributors of the angular resolution are the position uncertainties and Doppler broadening. The effect of energy uncertainty is large at the low energy end. In this section, the modeling of angular uncertainties caused by the position uncertainties, Doppler broadening and energy uncertainty is discussed. The overall angular uncertainty is the superposition of the angular uncertainties caused by different ARM contributors. If all the angular uncertainties are Gaussian, the overall angular uncertainty is the quadrature sum of the individual angular uncertainties. For a specific event, only Doppler broadening introduces a non-Gaussian

angular uncertainty. In this work, for simplicity, the angular uncertainty caused by Doppler broadening is modeled by a Gaussian distribution with the calculated standard deviation considering that Doppler broadening is not the most dominant factor in determining the angular uncertainty comparing with the position uncertainties.

4.3.1 Detector Position Uncertainties

The position uncertainties are the dominating factors in determining the angular uncertainty of the current system. The position uncertainties are about 1.3 mm in the lateral coordinates due to the pixellation on the detector anode surface, and 0.4 mm in depth due to the timing resolution[45].

Because the gamma-ray interaction positions determine the axis of the back-projection cone, the position uncertainties introduce an uncertainty in the cone axis direction. Because of the difference in the position uncertainties in x, y, and z directions, the uncertainty in the cone axis direction can vary at different directions. As a result, the angular uncertainty can vary at different points on the back-projection cone. It is impractical to precalculate the shape of the back-projection cone by simulations since there are too many possible position combinations. In this model, the angular uncertainties in the azimuthal and polar directions are calculated by means of error propagation, and the angular uncertainty in any arbitrary direction is approximated by the uncertainties in those two directions.

The azimuthal angle θ and the polar angle φ can be calculated from the first two interaction positions (x_1, y_1, z_1) and (x_2, y_2, z_2) as

$$\theta = \tan^{-1} \frac{z_2 - z_1}{\sqrt{(x_2 - x_1)^2 + (y_2 - y_1)^2}} \quad (4.6)$$

and

$$\varphi = \tan^{-1} \frac{y_2 - y_1}{x_2 - x_1} \quad (4.7)$$

By means of error propagation, the uncertainties in the azimuthal and polar angles can be calculated as

$$\sigma_\varphi^2 = \frac{1}{(x_2 - x_1)^2 + (y_2 - y_1)^2} \cdot \frac{p^2}{6} \quad (4.8)$$

and

$$\sigma_\theta^2 = \frac{[(z_2 - z_1)^2 \cdot p^2/6 + 2[(x_2 - x_1)^2 + (y_2 - y_1)^2](\Delta z)^2]}{[(x_2 - x_1)^2 + (y_2 - y_1)^2 + (z_2 - z_1)^2]^2} \quad (4.9)$$

in which, p is the pixel size of the detector, and Δz is the depth uncertainty.

However, the directions of the azimuthal angle φ and the polar angle θ are usually not orthogonal. We define another angular uncertainty $\sigma_{\varphi'}$, as shown in Fig. 4.9, to be the angular uncertainty of the axis in the azimuthal direction before it is projected onto the x-y plane. $\sigma_{\varphi'}$ can be calculated by

$$\sigma_{\varphi'} = 2 \tan^{-1} \left(\tan \frac{\sigma_\varphi}{2} \sin \theta \right) \quad (4.10)$$

The uncertainty in the direction of the cone axis is then determined by the uncertainties in two orthogonal angular directions, which are $\sigma_{\varphi'}$ and σ_θ . Assuming the spread of the back-projection cone at a specific direction β is Gaussian, the standard deviation is approximated by

$$\sigma(\beta) = \sigma_\theta \cos^2 \beta + \sigma_{\varphi'} \sin^2 \beta \quad (4.11)$$

This angular uncertainty model was compared with simulations, and it was found that this model is a good approximation. There is some distortion in the approximation in Eq. 4.11, but it is only noticeable when the two interaction points are very close to each other or the scattering angle is very large or small. In reality, those events usually have poor angular resolution and are not very helpful to image reconstruction. The drawback of this model is that it needs to calculate angle β pixel by pixel, therefore costs more computation time.

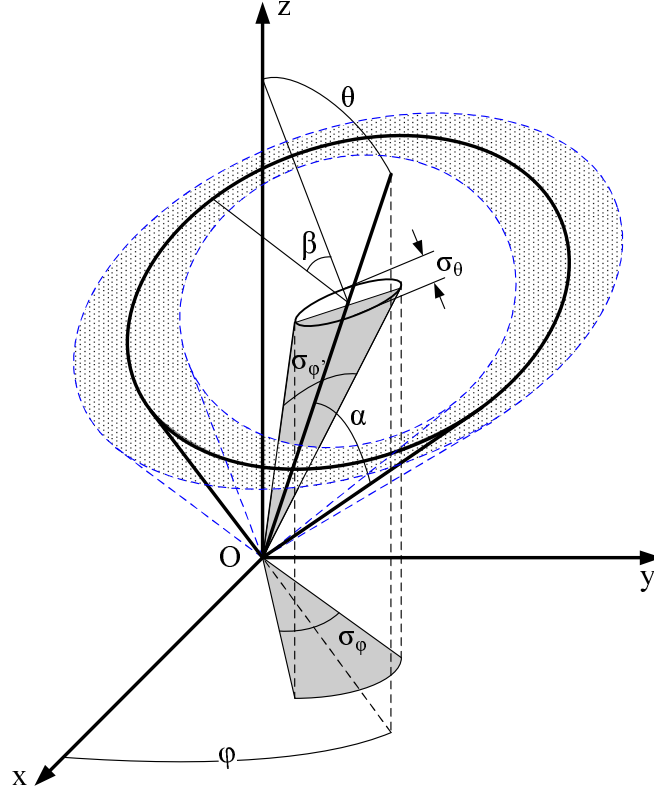


Figure 4.9: Angular uncertainty caused by the detector position uncertainties.

4.3.2 Doppler Broadening

Suppose that a single electron bound in an atom shell i has momentum \mathbf{p} . This momentum has a distribution $\rho_i(\mathbf{p}) \equiv |\psi_i(\mathbf{p})|$, in which $\psi_i(\mathbf{p})$ is the wave function of the electron in the momentum representation.

Define the momentum transfer vector $\mathbf{q} \equiv \hbar\mathbf{k} - \hbar\mathbf{k}'$, in which $\hbar\mathbf{k}$ and $\hbar\mathbf{k}'$ are respectively the momenta of the incident and scattered photons. The magnitude of \mathbf{q} is

$$q = \frac{1}{c} \sqrt{E_0^2 + E'^2 - 2E_0E' \cos \theta} \quad (4.12)$$

in which c is the speed of light, E_0 and E' are the energies of the incident and scattered photons, and θ is the scattering angle.

The projection of the initial electron momentum \mathbf{p} on the direction of the scat-

tering vector $-\mathbf{q}$ is defined as

$$p_z \equiv -\frac{\mathbf{p} \cdot \mathbf{q}}{q} = \frac{E_0 E' (1 - \cos \theta) - m_e c^2 (E_0 - E')}{c^2 q} \quad (4.13)$$

Eq. 4.13 gives a relationship among p_z , E' and θ . If p_z is known, Eq. 4.13 can be used to precisely calculate the energy of the scattered photon as a function of the scattering angle. In fact, if $p_z = 0$, Eq. 4.13 reduces to the Compton scattering formula of Eq. 1.1. In a real atom, p_z has a distribution defined by

$$J_i(p_z) \equiv \int \int \rho_i(\mathbf{p}) dp_x dp_y \quad (4.14)$$

in which $J_i(p_z)$ is referred to as the one-electron Compton profile.

The atomic Compton profile is given by the sum of all electrons, i.e.

$$J(p_z) = \sum_i f_i J_i(p_z) \quad (4.15)$$

in which f_i is the number of electrons in atomic shell i .

As a result, if the scattering angle is known, the energy of the scattered photon has a broadening due to the distribution of p_z . The Compton differential cross section is represented by a double differential equation obtained from the relativistic impulse approximation (IA) by Ribberfors[55]. Brusa simplified the equation by some first order approximations to[56]

$$\frac{d^2 \sigma}{dE' d\Omega} = \frac{r_e^2}{2} \left(\frac{E_C}{E_0} \right)^2 \left(\frac{E_C}{E_0} + \frac{E_0}{E_C} - \sin^2 \theta \right) J(p_z) \frac{dp_z}{dE'} \quad (4.16)$$

in which r_e is the classical electron radius, E_C is the scattered photon energy at scattering angle θ if the initial electron is at rest (Eq. 1.1). $\frac{dp_z}{dE'}$ can be obtained by taking the derivative of Eq. 4.13, i.e.

$$\frac{dp_z}{dE'} = \frac{m_e c}{cq} \left(\frac{E_0}{E_C} + \frac{E_0 \cos \theta - E'}{cq} \cdot \frac{p_z}{m_e c} \right) \quad (4.17)$$

The Compton profile can be obtained either by numerical Hartree-Fock profiles tabulated by Biggs[57] or by analytical profiles proposed by Brusa[56]. The relative differences between the numerical and analytical profiles are normally less than 5% except for large p_z where the probability $J(p_z)$ is very small. In this study, the analytical profiles are used, and the one-electron Compton profiles are approximated by[56]

$$J_i(p_z) = \sqrt{2}J_{i,0} \left(\frac{\sqrt{2}}{2} + \sqrt{2}J_{i,0}|p_z| \right) \exp \left[\frac{1}{2} - \left(\frac{\sqrt{2}}{2} + \sqrt{2}J_{i,0}|p_z| \right)^2 \right] \quad (4.18)$$

in which $J_{i,0}$ is the value of the profile at $p_z = 0$ obtained from the tables of Hartree-Fock Compton profiles published by Biggs.

In Eq. 4.16, the double differential Compton cross section can be rewritten as

$$\begin{aligned} \frac{d^2\sigma}{dE'd\theta} &= \int \frac{d^2\sigma}{dE'd\Omega} \sin\theta d\varphi = 2\pi \sin\theta \frac{d^2\sigma}{dE'd\Omega} \\ &= \pi \sin\theta r_e^2 \left(\frac{E_C}{E_0} \right)^2 \left(\frac{E_C}{E_0} + \frac{E_0}{E_C} - \sin^2\theta \right) J(p_z) \frac{dp_z}{dE'} \end{aligned} \quad (4.19)$$

As a result, we can calculate the double differential Compton cross section as a function of the scattering angle θ and the scattered photon energy E' , as shown in Fig. 4.10. The bright trace shows the relationship of E' and θ with no Doppler broadening, i.e., the Compton scattering formula of Eq. 1.1. The blurring represents the degree of Doppler broadening.

From Fig. 4.10, we can see that the uncertainty in the scattering angle is large for small E' , which means the Doppler broadening effect is more severe at large scattering angles. Fig. 4.11 shows the scattering angle distributions at different scattered photon energies. The incident gamma-ray energy is 662 keV. It is evident that the scattering angle distributions are not Gaussian, which makes it difficult to include Doppler broadening in the system response function.

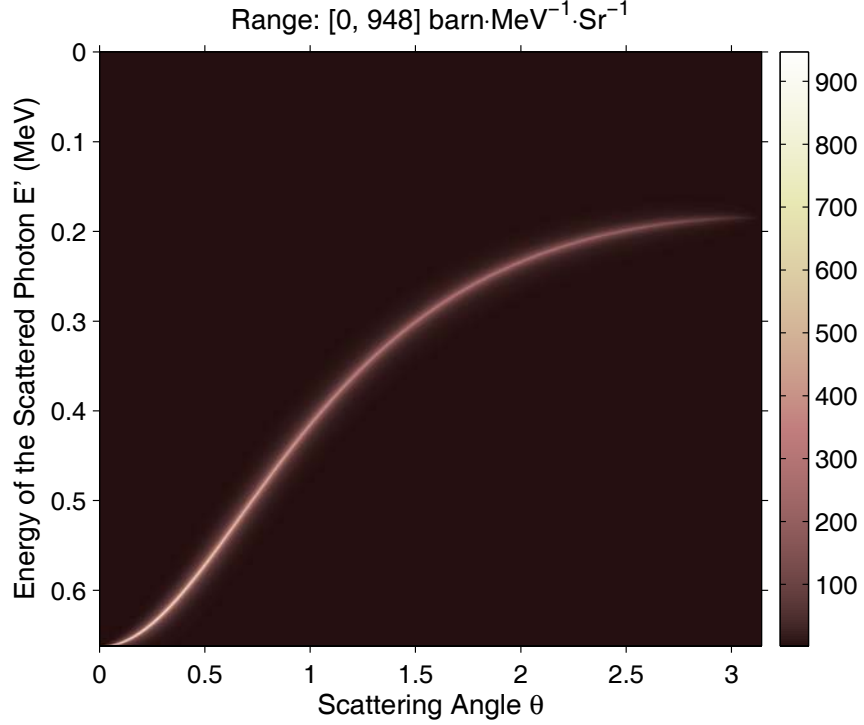


Figure 4.10: Double differential Compton cross section in $\text{Cd}_{0.9}\text{Zn}_{0.1}\text{Te}$. The incident photon energy is 662 keV. The color bar on the right represents the values of the double differential Compton cross section, which has units of barn · MeV⁻¹ · Sr⁻¹.

Fig. 4.12 shows the standard deviations in the ARM distributions due to Doppler broadening at different scattering angles calculated from both the Compton double differential cross section of Eq. 4.19 and Geant simulations. The theoretical values and the simulation results agree very well except at small scattering angles. This is caused by the fact that in the Geant Penelope model, Compton scattering is allowed only when the energy of the scattered electron is higher than the ionization energy of the electron. Therefore, small angle scatterings can only happen with those electrons in the outer shells, where the electron momentum has less uncertainty. As a result, the Geant simulations give less uncertainties in the ARM distributions at small scattering angles.

Eq. 4.19 indicates that the degree of Doppler broadening depends on two factors, which are the incident gamma-ray energy and the Compton profile determined by

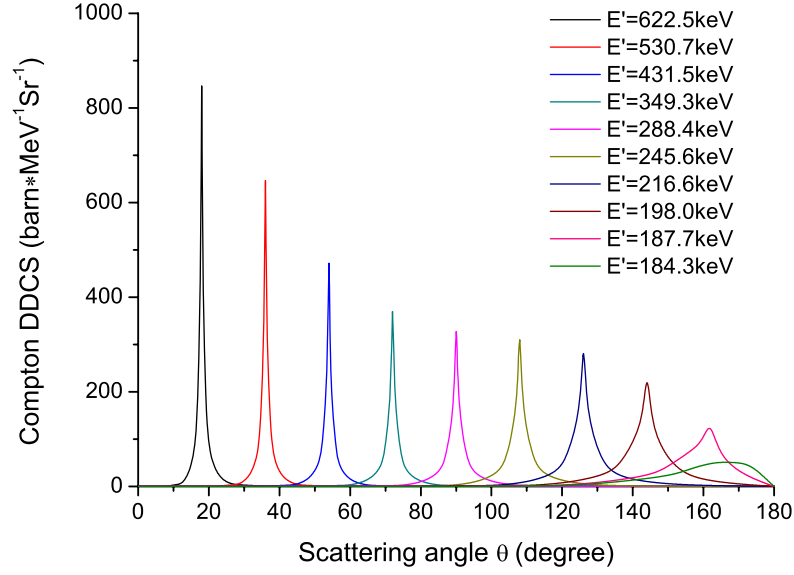


Figure 4.11: Scattering angle distributions at different energies of the scattered photon with 662 keV incident photon energy.

the detector material. The Doppler broadening effect is greater for lower energy gamma-rays and in materials with higher atomic numbers.

4.3.3 Detector Energy Uncertainties

The scattering angle is obtained from the measured energies by Eq. 4.2. The uncertainties in the measured energies will introduce an uncertainty in the calculated scattering angle, which is the half angle of the back-projection cone. The uncertainty in the scattering angle can be obtained by applying error propagation to Eq. 4.2. By doing so, the assumptions of unknown incident gamma-ray energy and full-energy deposition are implied. The scattering angle uncertainty of a two-pixel event is calculated to be

$$\Delta\theta_e = \frac{m_e c^2}{(E_{1m} + E_{2m})^2 E_{2m}^2 \sin \theta_e} \sqrt{E_{2m}^4 \Delta E_{1m}^2 + (E_{1m}^2 + 2E_{1m}E_{2m})^2 \Delta E_{2m}^2} \quad (4.20)$$

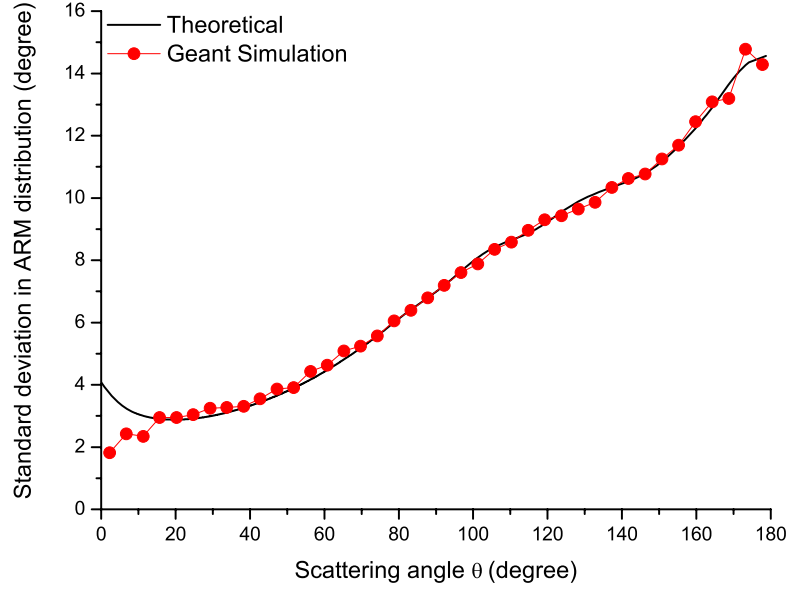


Figure 4.12: Standard deviations in the ARM distributions due to Doppler broadening at different scattering angles with 662 keV incident photon energy.

If $N(N > 2)$ interactions are recorded, Eq. 4.2 should be modified as

$$\theta_e = \cos^{-1} \left(1 + \frac{m_e c^2}{\sum_{i=1}^N E_{im}} - \frac{m_e c^2}{\sum_{i=2}^N E_{im}} \right) \quad (4.21)$$

As a result, the angular uncertainty caused by uncertainties in $E_{1m}, E_{2m}, \dots, E_{Nm}$ is

$$\Delta\theta_e = \frac{m_e c^2}{E_{0m}^2 (E_{0m} - E_{1m})^2 \sin \theta_e} \sqrt{(E_{0m} - E_{1m})^4 \Delta E_{1m}^2 + (E_{1m}^2 - 2E_{0m}E_{1m})^2 \sum_{i=2}^N \Delta E_{im}^2} \quad (4.22)$$

in which $E_{0m} = \sum_{i=1}^N E_{im}$.

Fig. 4.13 shows the standard deviations in the ARM distributions due to the energy uncertainty at different scattering angles calculated from both Eq. 4.20 and Geant simulations. Because there is a $\sin \theta_e$ on the denominator in Eq. 4.20, the angular uncertainty is large for both small and large scattering angles. Eq. 4.20 agrees with the Geant simulations very well except at large scattering angles. That

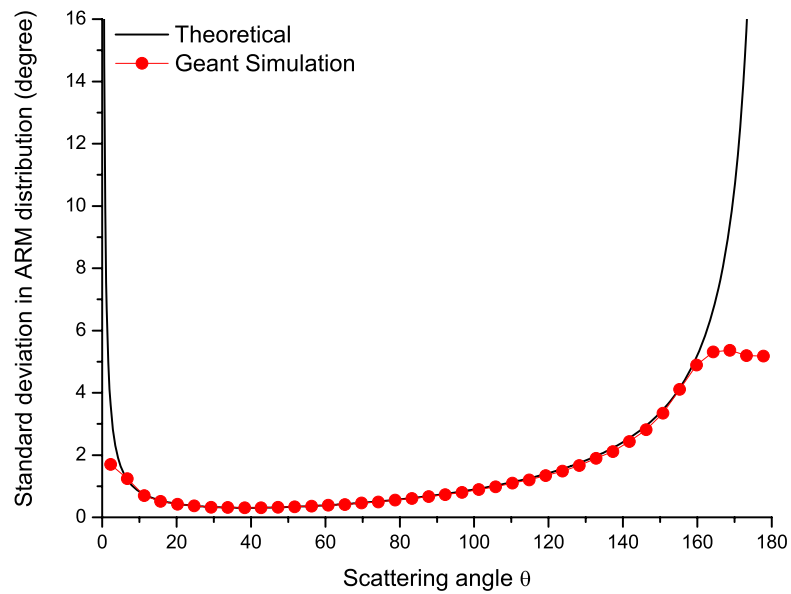


Figure 4.13: Standard deviations in ARM distributions due to the energy uncertainty at different scattering angles with 662 keV incident photon energy.

is because for the backscattered events, the uncertainties in the measured energies can make the energy deposition of the Compton scattering be greater than the Compton edge, and Eq. 4.2 becomes unsolvable. Those events are discarded by the Geant simulations, which results smaller angular uncertainties for the backscattered events.

CHAPTER V

IMAGE RECONSTRUCTION

Like many x-ray/gamma-ray imaging systems, such as CT/SPECT/PET and coded aperture imaging systems, the measured data of a Compton imager does not directly represent the source image. Certain algorithms must be applied to reconstruct the image. In this chapter, three different algorithms are discussed, including the simple back-projection algorithm, the filtered back-projection algorithm, and the list-mode maximum likelihood expectation maximization (MLEM) algorithm. Because the simple back-projection algorithm and the filtered back-projection algorithm can be operated event by event, the image reconstruction can be performed in real-time. The real-time imaging was implemented on a single 3-D CdZnTe detector for the first time. The 3-D imaging capability of the 3-D CdZnTe detector is also demonstrated.

5.1 The Simple Back-Projection Algorithm

From each sequenced multi-interaction event, the incident gamma-ray direction can be constrained on the surface of a cone, of which the axis is defined by the positions of the first two interactions, and the half angle is defined by the deposited energies. The most straightforward method to reconstruct the image is to simply back-project these cones to the imaging space, which is the 4π sphere around the

detector. The width of the back-projection cone is determined by the angular uncertainty discussed in Chapter IV. Since each cone passes the incident gamma-ray direction, the source can be enhanced and be distinguished from the background. Fig. 5.1 shows the simple back-projected image of a point source at 662 keV. Only two pixel events are used in the reconstruction. The angular resolution is about 50° .

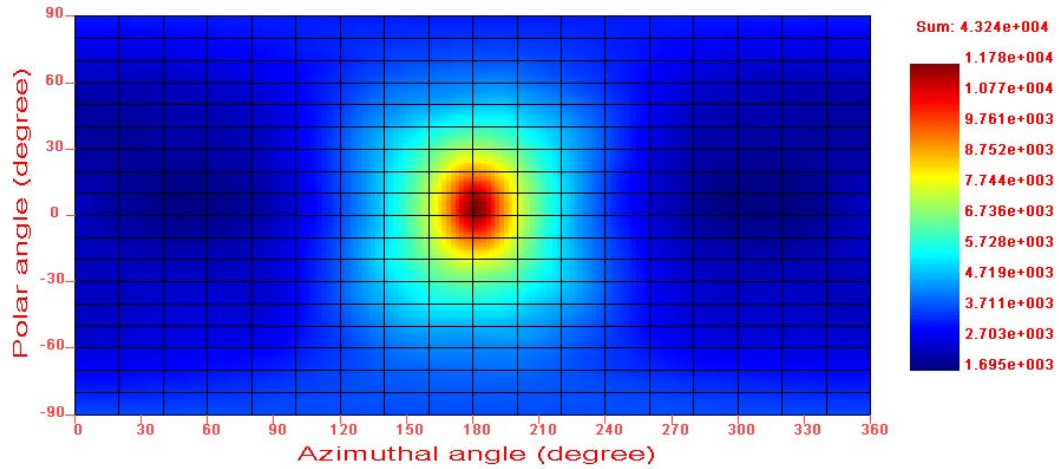


Figure 5.1: Simple back-projection image of a point ^{137}Cs source placed at the side of the detector.

The simple back-projection algorithm was applied to image the gamma-ray background in the laboratory. The image was reconstructed by those events in the 609 keV photopeak of ^{214}Bi , which is a daughter product in the ^{238}U decay chain. Because the uranium source in the lab is mostly from the concrete, the image actually shows the concrete distribution. The simple back-projection image is shown in Fig. 5.2. There was a big window in the lab where the measurement was taken, and no concrete was present in the direction of the window. The window is clearly shown in the image by the cold area. The count rate was very low, and only about 1200 two-pixel events were measured in 32 hours. Therefore, although the image appears to show some details in the ^{214}Bi distribution, those “details” are mostly due to statistics and are not trustable. It was the first time that the gamma-ray background was

imaged by a single 3-D CdZnTe detector.

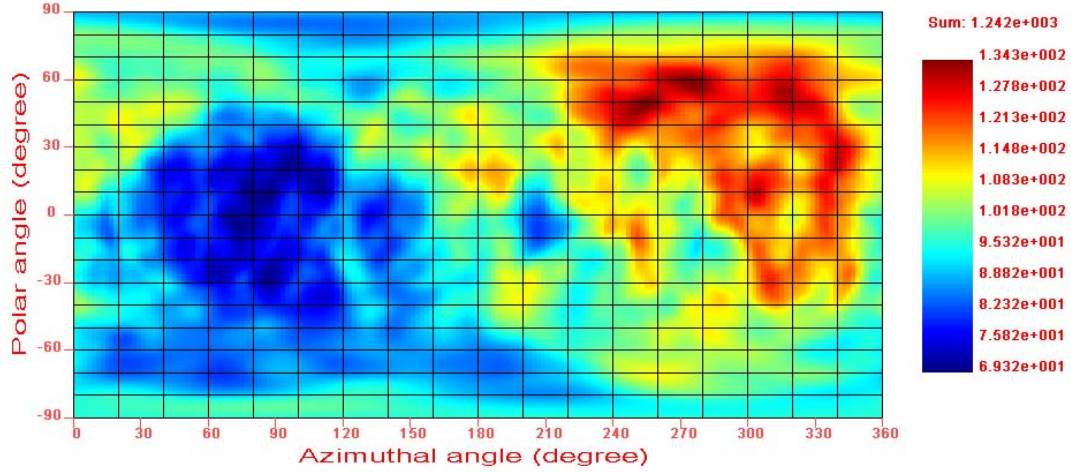


Figure 5.2: Simple back-projection image of the ^{214}Bi 609 keV photopeak. The image shows the concrete distribution, and the cold area on the left represents a window in the lab.

5.2 The Filtered Back-Projection Algorithm

Although the simple back-projection algorithm is fast and straightforward, its angular resolution is usually very poor. Algorithms such as the filtered back-projection algorithm widely used in computer tomography (CT) image reconstruction can provide better image resolution. However, due to the principle difference between Compton cameras and CT systems, the filtered back-projection algorithm using a linear ramp filter in CT systems can not be directly applied to Compton cameras. Unlike CT systems, the imaging space of a 3-D CdZnTe detector is the 4π sphere, of which the Fourier space is the spherical harmonics. The filter for a Compton camera is also different from CT systems because the point spread functions (PSF) of the two systems are formed in different ways. Due to this reason, most image reconstruct algorithms for Compton cameras are iterative methods[5, 58]. However, iterative algorithms are usually computationally intensive and their convergence points are often very different from the true source distribution because of the poor statistics.

In situations when reconstruction speed is critical and good angular resolution is required, direct image reconstruction algorithms such as the filtered back-projection algorithm are desired.

In 1994, Cree and Bones[59] developed a direct reconstruction algorithm by severely limiting the scattering direction to be perpendicular to the detector array. In 1998, Basko et al.[60] established an analytical inversion method from cone surface projections using the spherical harmonics without considering the distribution of possible scattering angles. Two years later, Parra[61] developed an analytical inversion algorithm for the complete data set of all possible scattering angles based on the Klein-Nishina formula[62]. In practice, as Tomitani and Hirasawa[63] pointed out, an actual Compton camera is unlikely to provide a data set with a full range of scattering angles due to the limitation in the detector system configuration and the difficulty in detecting small-angle scattering events. Tomitani further proposed an algorithm for limited angle Compton camera data set. Although the 3-D CdZnTe detector can detect the Compton scattering events of all scattering angles, the detection efficiency varies at different scattering angles. This is partly due to the variation in the path length of the detection material at different scattering directions, and partly due to the change of the scattered photon energy at different scattering angles. Therefore, the measured scattering angle distribution will be different from the theoretical prediction of the Klein-Nishina formula. In this study, a deconvolution algorithm using the spherical harmonics is developed. The point spread function is obtained by both theoretical calculation based on the Klein-Nishina formula and Monte Carlo simulations. The results show that the simulated point spread function performs better than the theoretical PSF.

5.2.1 Spherical Harmonics

Similar to the Fourier transform between the Cartesian space and the Fourier series, an arbitrary function $f(\vec{\Omega})$ defined on the 4π sphere can be transformed into the spherical harmonics by

$$F_l^m = \int_{S^2} d\vec{\Omega} f(\vec{\Omega}) Y_l^{m*}(\vec{\Omega}) \quad (5.1)$$

The inverse transform is given by

$$f(\vec{\Omega}) = \sum_{l=0}^{+\infty} \sum_{m=-l}^{m=l} F_l^m Y_l^m(\vec{\Omega}) \quad (5.2)$$

Here, $Y_l^m(\vec{\Omega})$ are the spherical harmonics on the 4π sphere and $Y_l^{m*}(\vec{\Omega})$ are the complex conjugate spherical harmonics

$$Y_l^m(\theta, \varphi) = \sqrt{\frac{(2l+1)}{4\pi} \cdot \frac{(l-m)!}{(l+m)!}} P_l^m(\cos \theta) e^{im\varphi} \quad (5.3)$$

in which $P_l^m(\cos \theta)$ are the associated Legendre polynomials.

5.2.2 Spherical Deconvolution

Even with perfect detector performance, such as perfect energy and position resolution, the summation image of the cone-beam projections for a point source is still blurred because only a small portion of the cone passes the true source location. This blurring is also referred to as the ‘‘Compton ring effect’’. The summation image of a point-like source is the point spread function of the detector system.

For a given source distribution $g(\vec{\Omega})$, the summation image $g'(\vec{\Omega}')$ of the cone-beam projections is a convolution of the source distribution $g(\vec{\Omega})$ with the point spread function of the detector system. Since the point spread function is azimuthal symmetric, we can write it as $h(\cos \omega)$. The convolution process can be written as

$$g'(\vec{\Omega}') = \int_{S^2} d\vec{\Omega} g(\vec{\Omega}) h(\cos \omega) \quad (5.4)$$

in which ω is the angle between $\vec{\Omega}$ and $\vec{\Omega}'$.

According to the spherical convolution theorem[64], Eq. 5.4 can be rewritten as

$$G_l'^m = \sqrt{\frac{4\pi}{2l+1}} G_l^m H_l^0 \quad (5.5)$$

where $G_l'^m$, G_l^m and H_l^0 are the transformations of $g'(\vec{\Omega}')$, $g(\vec{\Omega})$ and $h(\cos \omega)$ in the spherical harmonics domain, respectively.

Since $h(\cos \omega)$ is azimuthal symmetric, its spherical harmonics coefficients are all zeros if $m \neq 0$, and when $m = 0$, the spherical harmonics coefficients are

$$\begin{aligned} H_l^0 &= \int_{S^2} d\vec{\Omega} h(\cos \omega) Y_l^{0*}(\vec{\Omega}) \\ &= \int_{S^2} d\vec{\Omega} h(\cos \omega) \sqrt{\frac{2l+1}{4\pi}} P_l^0(\cos \omega) \\ &= \sqrt{\pi(2l+1)} \int d(\cos \omega) h(\cos \omega) P_l^0(\cos \omega) \end{aligned} \quad (5.6)$$

For a arbitrary function defined on $[-1, 1]$ such as $h(\cos \omega)$, it can also be expanded into the sum of the Legendre polynomials, i.e.

$$h(\cos \omega) = \sum_{l=0}^{+\infty} H_l P_l(\cos \omega) \quad (5.7)$$

The coefficients are defined by

$$H_l = \frac{2l+1}{2} \int d(\cos \omega) h(\cos \omega) P_l(\cos \omega) \quad (5.8)$$

By comparing Eq. 5.6 and Eq. 5.8, we find

$$H_l^0 = \sqrt{\frac{4\pi}{2l+1}} H_l \quad (5.9)$$

After replacing H_l^0 in Eq. 5.5 with Eq. 5.9, the spherical harmonics coefficients of the source image can be calculated as

$$G_l^m = \frac{(2l+1)G_l'^m}{4\pi H_l} \quad (5.10)$$

For a known point spread function $h(\cos \omega)$, its Legendre polynomials can be precalculated. To deconvolve the point spread function $h(\cos \omega)$ from the summation image of cone-beam projections $g'(\vec{\Omega}')$, we need to first transform the summation image into the spherical harmonics domain to obtain $G_l'^m$, then by Eq. 5.10, the spherical harmonics coefficients of the source image G_l^m can be computed. The source image $g(\vec{\Omega})$ is obtained by the inverse transform of the coefficients G_l^m into the 4π sphere space. This is analogous to the deconvolution procedures in Cartesian coordinates. Because it is difficult to get an analytical expression of the summation image $g'(\vec{\Omega}')$, the transforms between the 4π -sphere and the spherical harmonics are performed numerically by the SpharmonicKit package[65].

Since Eq. 5.5 is the spherical harmonics representation of Eq. 5.4, comparing Eq. 5.10 with Eq. 5.5, the deconvolution formula can be obtained as

$$g(\vec{\Omega}) = \int_{S^2} d\vec{\Omega}' g'(\vec{\Omega}') \tilde{h}(\cos \omega) \quad (5.11)$$

in which $\tilde{h}(\cos \omega)$ is a function with spherical harmonics coefficients of

$$\tilde{H}_l^0 = \left(\frac{2l+1}{4\pi} \right)^{\frac{3}{2}} \cdot \frac{1}{H_l} \quad (5.12)$$

The Legendre polynomial coefficients of $\tilde{h}(\cos \omega)$ are

$$\tilde{H}_l = \left(\frac{2l+1}{4\pi} \right)^2 \cdot \frac{1}{H_l} \quad (5.13)$$

The summation image $g'(\vec{\Omega}')$ is the sum of many cone-beam projections from individual events, as we do the reconstruction in list mode (Fig. 5.3). For a specific event i , the projection of the cone beam on the unit sphere is a ring defined by the cone axis direction $\vec{\Omega}_i$, and the cone half angle ω_i . This ring is the projection image $g'_i(\vec{\Omega}')$ of event i . The summation can be written as

$$g'(\vec{\Omega}') = \sum_{i=1}^N g'_i(\vec{\Omega}') \quad (5.14)$$

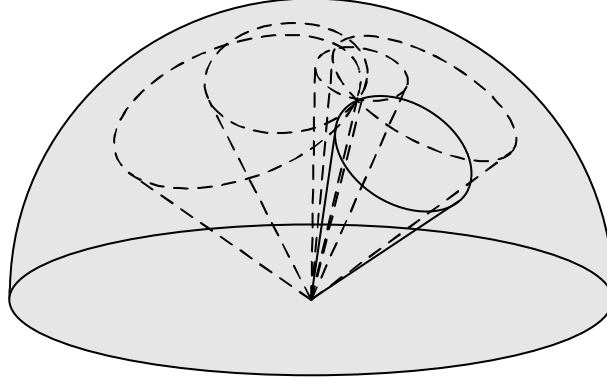


Figure 5.3: Summation of cone-beam projections on the unit sphere

According to the linear property of the spherical convolution, Eq. 5.11 can be rewritten as

$$g(\vec{\Omega}) = \sum_{i=1}^N \int_{S^2} d\Omega' g'_i(\vec{\Omega}') \tilde{h}(\cos \omega) \quad (5.15)$$

which means the filtering can be done event-by-event, which makes real-time imaging possible. The price is the requirement of doing the Fourier transform on the 4π -sphere for each event, which increases the computational cost. However, we notice that $g'_i(\vec{\Omega}')$ is a function which is azimuthal symmetric around the cone axis $\vec{\Omega}_i$. Therefore, if the Fourier transform is performed in a 4π coordinate system with its z direction defined as the cone axis $\vec{\Omega}_i$, only Legendre polynomial expansion is required, and the computational cost can be reduced. Because the spherical convolution is rotation invariant, we can rotate the filtering coordinate system of each event to the original 4π imaging sphere without altering the filtering result. With the help of the fast Fourier transform algorithms on the 4π -sphere developed in recent years[64, 66, 65], the computational cost is minimized.

5.2.3 Filter Design from Theoretical Calculation

5.2.3.1 Filter of Perfect Detectors

The point spread function $h(\cos \omega)$ is mostly caused by the Compton ring effect. To apply the deconvolution process of Eq. 5.10, the point spread function (or the filter) must be precalculated. To derive the theoretical point spread function, we assume that the detector has perfect energy and position resolutions, there is no Doppler broadening, the interaction sequence is given by the simple comparison method described in Chapter III, and the detector is large enough that all scattered photons are detected. The last assumption ensures that the scattering angle distribution follows the Klein-Nishina formula.

The differential scattering cross section of Compton scattering per atom is given by the Klein-Nishina formula:

$$\frac{d\sigma}{d\Omega} = \frac{Zr_e^2}{2} \left(\frac{E_C}{E_0} \right)^2 \left(\frac{E_C}{E_0} + \frac{E_0}{E_C} - \sin^2 \theta \right) \quad (5.16)$$

in which Z is the atomic number of the scattering medium, r_e is the classical electron radius, and E_C is the scattered photon energy at scattering angle θ . In fact, Eq. 5.16 can be obtained by integrating the double differential equation of Eq. 4.16 over E' .

Since $d\Omega = \sin \theta d\varphi d\theta$, Eq. 5.16 can be rewritten as

$$\frac{d\sigma}{d\theta} = \pi Z r_e^2 \left(\frac{E_C}{E_0} \right)^2 \left(\frac{E_C}{E_0} + \frac{E_0}{E_C} - \sin^2 \theta \right) \sin \theta \quad (5.17)$$

Suppose a mono-energetic source irradiates an idealized detector from above. When the detector detects an event with scattering angle θ , the cone-beam projection will generate a ring with half angle θ on the unit 4π -sphere. Since the detector is perfect, the reconstructed cone always passes the true source location, which is at the zenith of the 4π sphere. When many rings are reconstructed on the sphere, the back-projection summation image is formed, which is also the point spread function

of the Compton camera. Since the system is symmetric around z axis, the point spread function thus is only related to the polar angle ω . Therefore, the point spread function is also written as a function of a single variable, $h(\cos \omega)$. Fig. 5.4 shows the contribution of a cone back-projection to the point spread function.

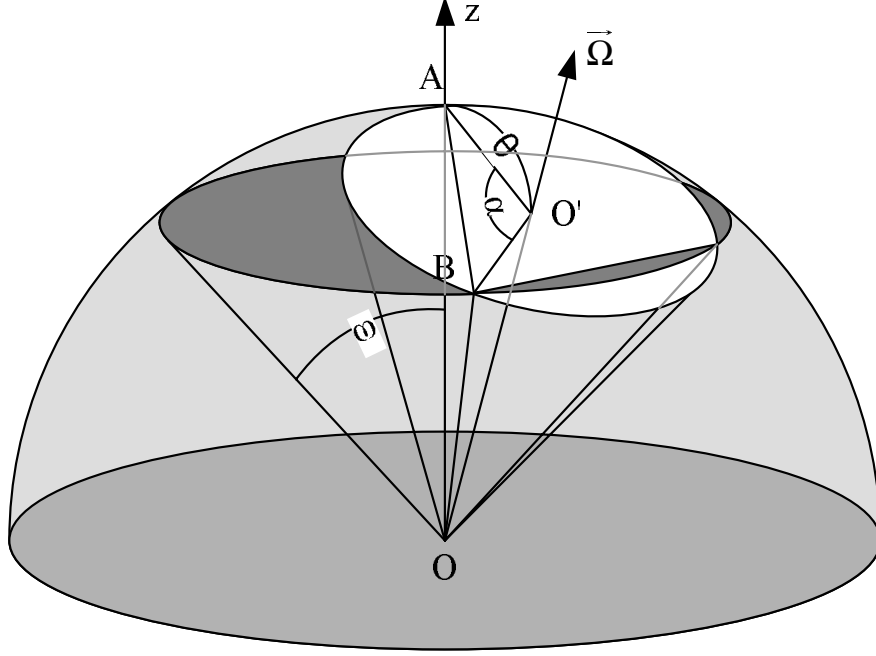


Figure 5.4: The contribution of a cone-beam projection with cone axis $\vec{\Omega}$ and half angle θ to the PSF

The values assigned to different pixels on the projection ring should be uniform, since the gamma-ray could come from any direction on that ring, provided that the incident gamma-ray is not polarized. If we assume that each event carries the same amount of information, the sum of the values on each back-projection ring should be normalized. Since the perimeter of each ring is proportional to $\sin \theta$, the values on each ring should be proportional to $1/\sin \theta$. If a back-projection ring with half angle θ intersects a ring on the unit sphere with half angle ω at angle α as shown in Fig. 5.4, the contribution of this ring to the point spread function from ω to $\omega + d\omega$ is proportional to $d\alpha/\sin \theta$. Therefore, the sum of the point spread function between ω

and $\omega + d\omega$ is proportional to the integral of all possible scattering angles, as shown by

$$h(\cos \omega) \sin \omega d\omega = \int_0^\pi d\theta K(\theta) \sin \theta \frac{d\alpha}{\sin \theta} \quad (5.18)$$

in which $K(\theta)$ is the Klein-Nishina cross section formula and $K(\theta) \sin \theta$ is proportional to the probability density function of the scattering angle θ . $K(\theta) \sin \theta$ is given by the differential cross section in Eq. 5.17.

As a result, the contribution of cone-beam projections to the point spread function at angle ω can be evaluated by

$$h(\cos \omega) = \int_0^\pi d\theta K(\theta) \frac{1}{\sin \omega} \cdot \frac{d\alpha}{d\omega} \quad (5.19)$$

In triangle ABO' , $|AB| = 2 \sin \frac{\omega}{2}$, and $|O'A| = |O'B| = \sin \theta$. The law of cosine gives

$$|AB|^2 = |O'A|^2 + |O'B|^2 - 2 |O'A| |O'B| \cos \alpha \quad (5.20)$$

Therefore, the geometrical relationship between α , ω and θ is obtained as

$$\cos \alpha = 1 - \frac{2 \sin^2 \frac{\omega}{2}}{\sin^2 \theta} \quad (5.21)$$

As a result, Eq. 5.19 becomes

$$h(\cos \omega) = \int_0^\pi d\theta K(\theta) \frac{1}{\sin \omega} \cdot \frac{\cos \frac{\omega}{2}}{\sqrt{\cos^2 \frac{\omega}{2} - \cos^2 \theta}} \quad (5.22)$$

We notice when the scattering angle θ is smaller than $\omega/2$ or greater than $\pi - \omega/2$, the back-projection cone does not contribute to the point spread function at ω , and the integral in Eq. 5.22 can be rewritten as

$$h(\cos \omega) = \frac{1}{2 \sin \frac{\omega}{2}} \int_{\omega/2}^{\pi - \omega/2} \frac{d\theta K(\theta)}{\sqrt{\cos^2 \frac{\omega}{2} - \cos^2 \theta}} \quad (5.23)$$

This result differs from Parra's result with a term of $\sin \theta$ in the integral. This is because of the fact that Parra assumed that each point on all back-projection

rings has the same value, while we assume that each back-projection ring contains the same amount of information. Therefore, in our calculation, the values on the back-projection rings are proportional to $1/\sin\theta$. This difference should not affect the final reconstructed image because although there is a $1/\sin\theta$ difference in the PSFs, the $1/\sin\theta$ difference is also present in the back-projection rings. As a result, the filtered images by both methods are identical.

5.2.3.2 Filter of detectors with limited detection angles

Tomitani pointed out that in real Compton cameras, the distribution of the scattering angle is always limited[63]. In our 3-D position sensitive CdZnTe detectors, this is especially true because of the sequence reconstruction algorithm. For events with scattering angle between η_1 and η_2 ($\eta_1 < \eta_2$), the point spread function can be obtained by replacing $K(\theta)$ with $K'(\theta)$ in Eq. 5.23, in which $K'(\theta)$ is defined as

$$K'(\theta) = \begin{cases} K(\theta) & \theta \in (\eta_1, \eta_2) \\ 0 & otherwise \end{cases} \quad (5.24)$$

In 3-D position-sensitive CdZnTe detectors, the sequence of interactions in a multiple-pixel event must be reconstructed based on energy depositions. For simplicity, only two-pixel full-energy deposition events are considered. There are two possible interaction sequences for each two-pixel event (Fig. 5.5). The simple comparison sequence reconstruction algorithm performs the Compton edge test first. Those events with an energy deposition greater than the Compton edge must deposit the smaller amount of energy first. For other events, although both sequences are possible, the interaction with higher energy deposition is selected as the first interaction since the possibility of these events is higher[30].

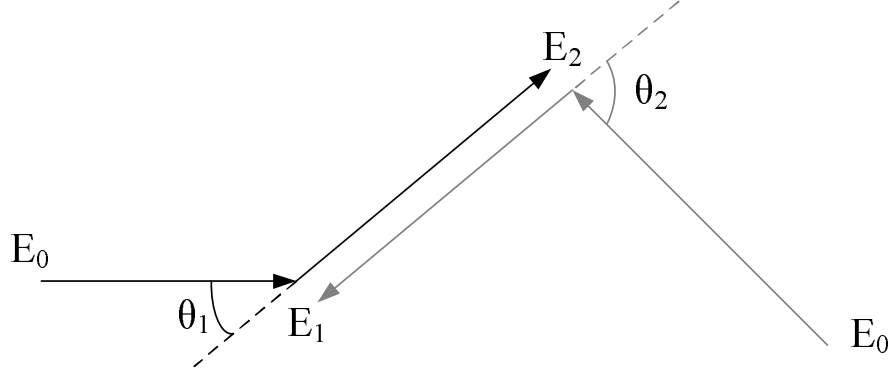


Figure 5.5: Two possible sequences in a two-pixel event. θ_1 and θ_2 are the two possible scatter angles.

Two angles, ω_1 and ω_2 , are defined as

$$\cos \omega_1 = 1 - \frac{(m_e c^2)^2}{2E_0^2} \quad (5.25)$$

and

$$\cos \omega_2 = 1 - \frac{m_e c^2}{E_0} \quad (5.26)$$

From the definition, $0 < \omega_1 < \omega_2 < \pi$ when $E_0 > m_e c^2/2$. When the scattering angle is between 0 and ω_1 , the energy deposition of the second interaction must be higher than the Compton edge. Therefore, the reversed sequence is physically impossible, and the sequence can always be correctly reconstructed by choosing the smaller energy deposition as the first interaction. ω_2 is the scattering angle when the scattered photon energy equals the scattered electron energy. When the scattering angle is between ω_1 and ω_2 , the first interaction deposits less energy than the second one, therefore the sequence is incorrectly determined by the simple-comparison algorithm. For events with scattering angle between ω_2 and π , the first interaction deposits more energy than the second one and their sequences are correctly reconstructed.

When the energy of the incident gamma-ray is less than $m_e c^2/2$, $\cos \omega_1$ and $\cos \omega_2$ are less than -1. This means that the first interaction always deposits less energy than the second one and the sequence can always be correctly reconstructed if the

strategy of the sequence reconstruction algorithm is reversed for this energy range. In this case, scattering events with all scattering angles can be correctly sequenced, and the point spread function is represented by Eq. 5.23. The following discussion will only focus on scattering events with initial gamma-ray energy greater than $m_e c^2/2$.

Suppose the correct sequence is $E_1 \rightarrow E_2$, then we have

$$\cos \theta_1 = 1 + \frac{m_e c^2}{E_0} - \frac{m_e c^2}{E_2} \quad (5.27)$$

and

$$\cos \theta_2 = 1 + \frac{m_e c^2}{E_0} - \frac{m_e c^2}{E_1} = 1 + \frac{m_e c^2}{E_0} - \frac{m_e c^2}{E_0 - E_2} \quad (5.28)$$

in which θ_1 is the true scattering angle, and θ_2 is the calculated scattering angle given the wrong sequence. From Eq. 5.27 and Eq. 5.28 we get

$$\cos \theta_2 = 1 - \frac{1}{\gamma^2(1 - \cos \theta_1)} \quad (5.29)$$

in which $\gamma = E_0/m_e c^2$ is the ratio of the initial gamma-ray energy and the rest mass energy of an electron.

For events which can be correctly sequenced by our algorithm, i.e., events with scattering angle in region $[0, \omega_1]$ or $[\omega_2, \pi]$, their contribution to the point spread function can be calculated by

$$h_{correct}(\cos \omega) = \frac{1}{2 \sin \frac{\omega}{2}} \int_{\omega/2}^{\pi-\omega/2} \frac{d\theta K'(\theta)}{\sqrt{\cos^2 \frac{\omega}{2} - \cos^2 \theta}} \quad (5.30)$$

in which,

$$K'(\theta) = \begin{cases} K(\theta) & \theta \in (0, \omega_1) \cup (\omega_2, \pi) \\ 0 & otherwise \end{cases} \quad (5.31)$$

For events with scattering angle in region $[\omega_1, \omega_2]$, the sequence will be incorrectly reconstructed, therefore the back-projection cones do not pass the source location, and their contribution to the point spread function will be different.

The sequences corresponding to the two possible scatter angles are opposite, so when calculating the contribution of the incorrectly sequenced events to the point spread function, the angle between the cone and the E_2E_1 vector $\vec{\Omega}$ is $\pi - \theta_2$. The reconstructed cone based on an incorrectly sequenced event will not pass the true source position, unless $\theta_1 + \theta_2$ exactly equals to 180° . The contribution of an incorrectly sequenced event to the point spread function is shown in Fig. 5.6. As a result, Eq. 5.23 is not valid anymore. The PSF of the incorrectly sequenced events should be recalculated from Eq. 5.19.

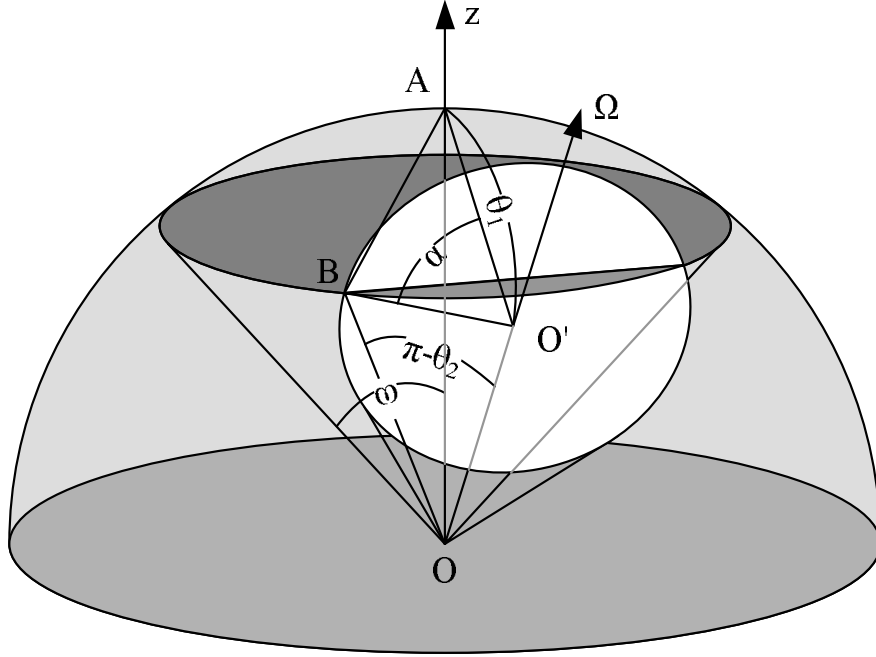


Figure 5.6: The contribution of an incorrectly sequenced event to the PSF. The event generates a cone-beam projection with cone axis $\vec{\Omega}$ and half angle $\pi - \theta_2$

In triangle ABO' , $|AB| = 2 \sin(\omega/2)$, $|AO'| = \sin \theta_1$, and $|BO'| = \sin \theta_2$. By the law of cosine, the geometry relationship of Eq. 5.32 is obtained

$$\cos \alpha = \frac{\sin^2 \theta_1 + \sin^2 \theta_2 - 4 \sin^2 \frac{\omega}{2}}{2 \sin \theta_1 \sin \theta_2} \quad (5.32)$$

As a result,

$$\frac{d\alpha}{d\omega} = \frac{2 \sin \omega}{\sqrt{4 \sin^2 \theta_1 \sin^2 \theta_2 - (\sin^2 \theta_1 + \sin^2 \theta_2 - 4 \sin^2 \frac{\omega}{2})^2}} \quad (5.33)$$

in which,

$$\sin^2 \theta_2 = \frac{2}{\gamma^2(1 - \cos \theta_1)} - \frac{1}{\gamma^4(1 - \cos \theta_1)^2}$$

Since θ_1 is the true scatter angle, $\theta_1 = \theta$. The contribution of those events with scattering angles between ω_1 and ω_2 to the point spread function is

$$\begin{aligned} h_{incorrect}(\cos \omega) &= \int_{\omega_1}^{\omega_2} d\theta K(\theta) \frac{1}{\sin \omega} \cdot \frac{d\alpha}{d\omega} \\ &= \int_{\omega_1}^{\omega_2} \frac{2K''(\theta)d\theta}{\sqrt{4 \sin^2 \theta f(\theta) - [\sin^2 \theta + f(\theta) - 4 \sin^2 \frac{\omega}{2}]^2}} \end{aligned} \quad (5.34)$$

where $f(\theta)$ and $K''(\theta)$ are defined as

$$f(\theta) = \frac{2}{\gamma^2(1 - \cos \theta)} - \frac{1}{\gamma^4(1 - \cos \theta)^2} \quad (5.35)$$

and

$$K''(\theta) = \begin{cases} K(\theta) & \theta \in (\omega_1, \omega_2) \\ 0 & otherwise \end{cases} \quad (5.36)$$

The overall PSF for incident photons with energy greater than $m_e c^2/2$ now can be written as

$$\begin{aligned} h(\cos \omega) &= h_{correct}(\cos \omega) + h_{incorrect}(\cos \omega) \\ &= \frac{1}{2 \sin \frac{\omega}{2}} \int_{\omega/2}^{\pi - \omega/2} \frac{d\theta K'(\theta)}{\sqrt{\cos^2 \frac{\omega}{2} - \cos^2 \theta}} \\ &\quad + \int_{\omega_1}^{\omega_2} \frac{2K''(\theta)d\theta}{\sqrt{4 \sin^2 \theta f(\theta) - [\sin^2 \theta + f(\theta) - 4 \sin^2 \frac{\omega}{2}]^2}} \end{aligned} \quad (5.37)$$

in which ω_1 , ω_2 , $K'(\theta)$, $K''(\theta)$ and $f(\theta)$ are defined in Eq. 5.25, Eq. 5.26, Eq. 5.31, Eq. 5.36, and Eq. 5.35 respectively.

The overall analytical point spread function and its Legendre polynomial coefficients of 3-D position sensitive CdZnTe detectors at 662 keV are shown in Fig. 5.7. As we can see, the Legendre polynomial expansion coefficients become almost constant at high orders. This is due to the fact that the point spread function of Eq. 5.37 is infinite when $\omega = 0$, which makes the point spread function similar to a delta function.

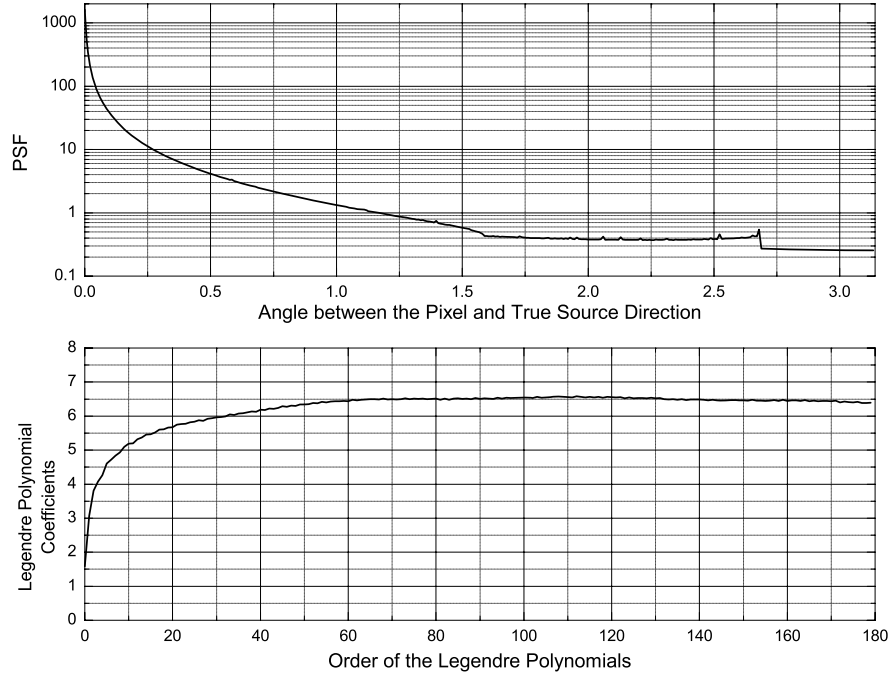


Figure 5.7: The upper figure shows the PSF of all two-pixel events at 662 keV with sequence reconstruction algorithm applied. Due to the azimuthal symmetry of the PSF, the Fourier transform of the PSF into the spherical harmonics domain can be simplified to the Legendre polynomial expansion. The bottom figure shows the Legendre polynomial coefficients.

5.2.4 Filter Design from Monte Carlo Simulations

In a real detector system, the measured scattering angle distribution usually does not follow the Klein-Nishina formula, because the detection efficiency varies for events with different scattering angles. Scattered photons at smaller scattering angles have higher energy than back-scattered photons, thus they are more likely to escape the

detector. In other words, the actual scattering angle distribution favors large scattering angles comparing with the theoretical prediction of the Klein-Nishina formula. Fig. 5.8 shows the difference of the scattering angle distributions between the prediction by the Klein-Nishina formula and Geant simulations.

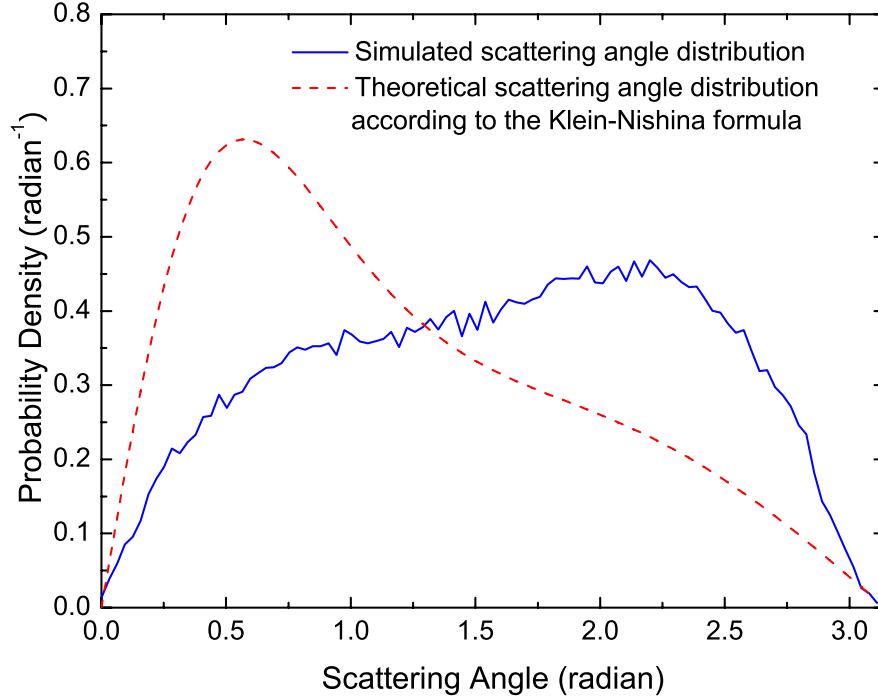


Figure 5.8: The simulation shows that the actual scattering angle distribution of 662 keV gamma rays in a 3-D CdZnTe detector is different from the theoretical prediction based on the Klein-Nishina formula, thus the actual PSF should be different from Eq. 5.23.

Therefore, the theoretical prediction of the point spread function using the Klein-Nishina formula cannot be applied directly on an actual Compton camera. Monte Carlo simulations using Geant4 packages were performed to provide the point spread function of a $15\text{ mm} \times 15\text{ mm} \times 10\text{ mm}$ 3-D CdZnTe detector. In the simulations, charge sharing problem between neighboring pixel anodes caused by the finite initial electron cloud size and the diffusion of electrons were not modeled. The detector was idealized with perfect depth and energy resolution. The anode of the detector was still divided into an 11×11 pixel array to account for the pixellation effect. A 662

keV gamma-ray source was placed 20 cm away from the side of the detector, and only two-pixel full-energy deposition events were recorded. These two-pixel events with correct sequences were reconstructed using the simple back-projection algorithm to generate the point spread function image. The information carried by each event was set to be the same, i.e., the contribution of each event to the summation image was normalized. The reconstructed point spread function from the simulated data is shown in Fig. 5.9.

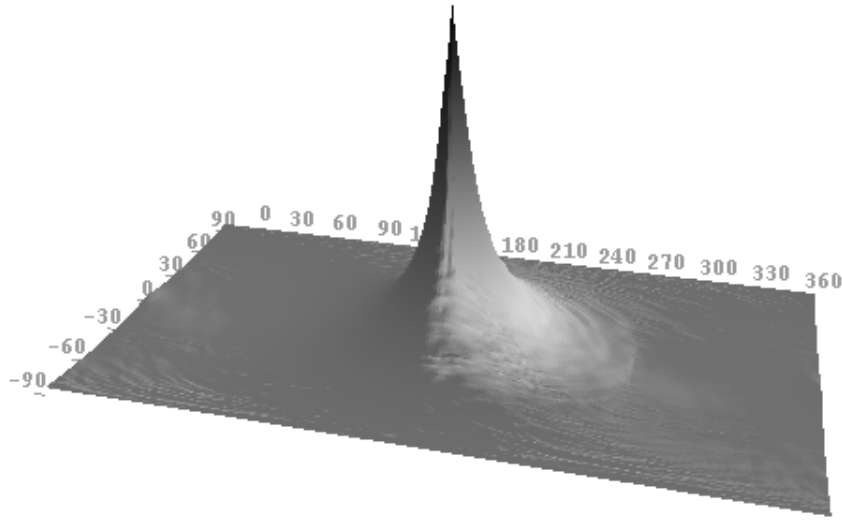


Figure 5.9: Simulated PSF. A 662 keV gamma-ray source was placed at the side of the detector, and only two-pixel full-energy deposition events were reconstructed.

Fig. 5.10 shows the simulated point spread function and its Legendre polynomial coefficients. The scale in Fig. 5.10 differs from the scale in Fig. 5.7 because the PSF in Fig. 5.7 is calculated directly from Eq. 5.37 while the PSF in Fig. 5.10 is from the simple back-projection image, which depends on how many events are used. By comparing the Legendre polynomial coefficients in Fig. 5.7 and Fig. 5.10 we can see that the PSF from the simulated data has much lower values for high-frequency components than the PSF from the theoretical calculation. This is because the pixellation of the detector blurs the simple back-projection image and suppresses

the high-frequency components.

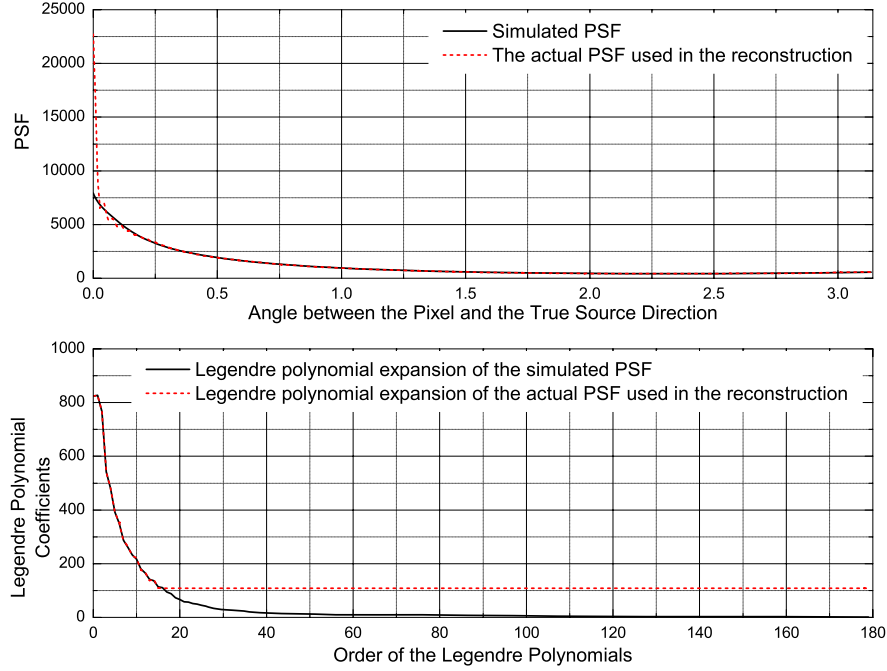


Figure 5.10: The upper figure shows the simulated PSF and the actual PSF used in the reconstruction. The incident gamma-ray energy is at 662 keV. The coefficients of the Legendre polynomials are shown in the bottom figure. The PSFs are for a single 15 mm \times 15 mm \times 10 mm 3D CdZnTe detector.

As shown in Fig. 5.10, the Legendre polynomial coefficients vanish quickly as the order increases. According to the deconvolution equation of Eq. 5.10, the Legendre polynomial coefficients of the PSF appear on the denominator. As a result, a low pass filter is usually required to avoid instability problem. However, a low pass filter with bandwidth D limits the angular resolution to π/D . If the bandwidth is too low, the system cannot achieve good angular resolution. As an alternative solution, the coefficients of the PSF for orders greater than 15 were set to be constant which equals the value at the order of 15, as shown in Fig. 5.10. The number of 15 is selected based on the observation that the algorithm performs the best at this number. The maximum order is set to 180, but could be lowered to save computation time. The actual PSF used in the reconstruction and its Legendre polynomial expansion is

also shown in Fig. 5.10. As can be seen, the actual applied PSF differs from the simulated PSF only when the angle is small. The pulse in the actual applied PSF at small angles is introduced by the constant Legendre polynomial coefficients at high orders. However, the actual applied PSF and the simulated PSF agree very well at large angles. As a result, most of the tail in the simple back-projection image can be deconvolved by the actual applied PSF, while an artifact similar to a sinc function will be introduced at small angles. However, because the width of the artifact is much smaller than the achievable angular resolution of the 3D CdZnTe detector (only a few degrees as shown in Fig. 5.10), this artifact will be overwhelmed by other angular uncertainties (such as the uncertainties caused by the position uncertainties and Doppler broadening) and is not noticeable in the final reconstructed image. By this treatment, the system can achieve better angular resolution while avoiding the instability problem.

5.2.5 Performance

The filtered back-projection algorithm was applied to both simulated and measured data using the theoretical PSF of Fig. 5.7 and the simulated PSF of Fig. 5.10 separately. Only two-pixel events with full-energy deposition were used. Neighboring pixel events with depth separation less than 2 mm were excluded since in real measurements, those events are most likely to be charge sharing events.

In the Geant4 simulation, five 662 keV point sources were placed in a cross shape at the side of the detector. The distance between the center source and the detector was 25 cm, and the distances between the center source and the four corner sources were 10 cm. The detector was modeled with a 5 keV FWHM electronic noise, and average ionization energy of 5 eV for each electron-hole pair, a Fano factor of 1, and a depth resolution of 1 mm FWHM. About 32,000 two-pixel full-energy events were

used in the reconstruction. The reconstructed images are shown in Fig. 5.11, which also includes a simple back-projection image for comparison. Evidently, the filtered back-projection image using the simulated PSF has the best angular resolution.

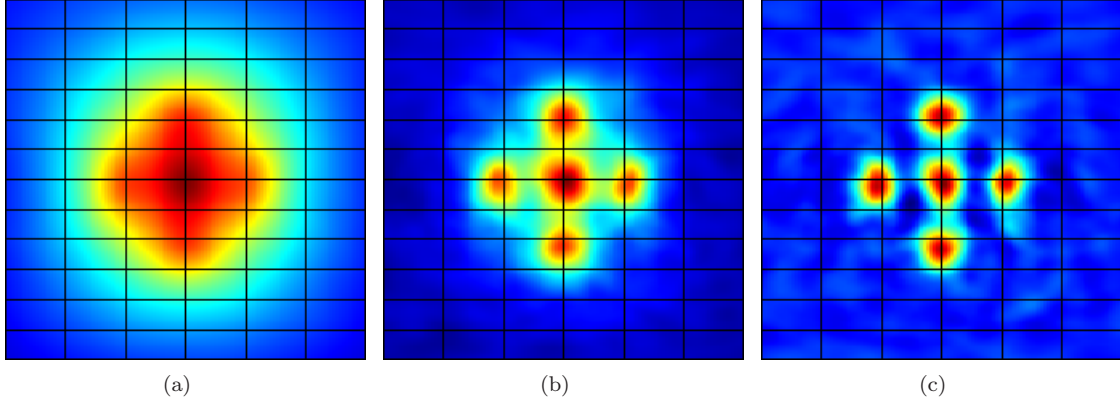


Figure 5.11: Reconstructed images of the simulated data with five Cs-137 point sources. (a). Simple back-projection. The five sources can not be distinguished. (b). Filtered back-projection with the theoretical PSF shown in Fig. 5.7. The five sources can be distinguished. (c). Filtered back-projection with the simulated PSF shown in Fig. 5.10. It has better angular resolution than the image reconstructed with the theoretical PSF.

In the measurement, two $10\ \mu\text{Ci}$ Cs-137 sources were placed 15 degrees apart and 10 cm away from one side of the detector. About 40,000 two-pixel full-energy events were used in the reconstruction. The reconstructed images are shown in Fig. 5.12. It can be seen from Fig. 5.12 that the reconstructed image using the theoretical PSF can barely distinguish the two sources, while the two sources are well resolved using the simulated PSF.

The angular resolution of a point Cs-137 source by the filtered back-projection algorithm is about 19° and 25° in the azimuthal and lateral directions, respectively.

Because of the linear property of the filtered back-projection algorithm, the reconstruction can be done event-by-event. Currently, remote real-time imaging with the filtered back-projection algorithm has been implemented on a single 3-D CdZnTe detector.

When calculating the PSF from simulated data, it is desired to get the PSF as

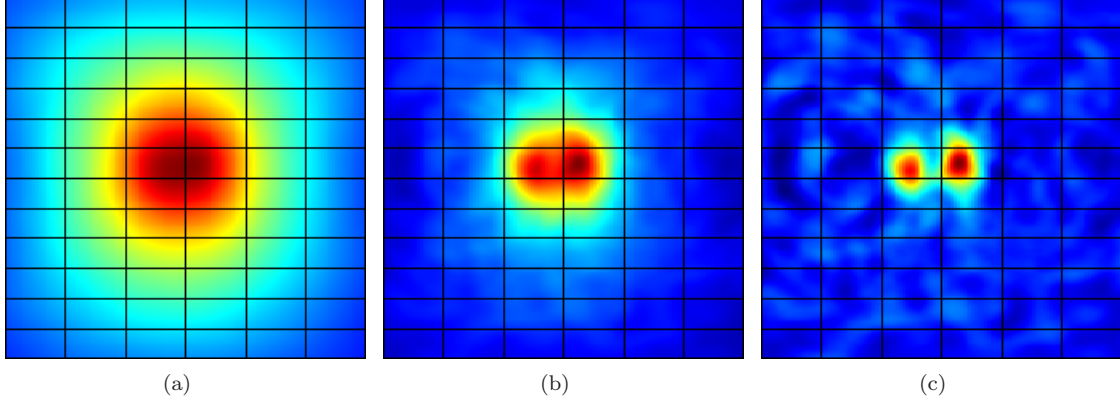


Figure 5.12: Reconstructed images of the measured data with two Cs-137 sources separated by 15 degrees. (a). Simple back-projection of the reconstruction cones. The two sources can not be distinguished. (b). Filtered back-projection with the theoretical PSF shown in Fig. 5.7. The two sources can barely be distinguished. (c). Filtered back-projection with the simulated PSF shown in Fig. 5.10. The two sources can be distinguished clearly.

close as the true PSF of the system. Factors that can affect the PSF include the scattering angle distribution, Doppler broadening, the detector position and energy uncertainties, and the sequence reconstruction. In the calculated PSF of Fig. 5.10, only the scattering angle distribution, Doppler broadening, and the detector pixellation were included. Because the energy and depth resolution can vary for different detectors, and different sequence reconstruction algorithms might be developed and applied, other factors were not included.

In both the measurement and the simulation, the sources were at 662 keV and placed at the side of the detector. The PSF was calculated based on the simulation result with this configuration. If the source is at different locations, the distribution of the scattering angle might be different, thus the PSF can be changed. However, since the asymmetry in the geometry is not significant for a $15\text{ mm} \times 15\text{ mm} \times 10\text{ mm}$ CdZnTe detector, the PSF of a point source at the side can still be applied to other source locations. For a detector configuration with large asymmetry, simulations should be performed to obtain the PSFs at different source locations. Different PSFs

at different energies also need to be calculated from separate simulations, which could require a large amount of work. For each source location at each energy, the PSF can be described by a few coefficients of the Legendre polynomials. Therefore, it does not require a huge database to store a complete set of PSFs.

5.3 The List-Mode Maximum Likelihood Expectation Maximization Algorithm

5.3.1 The MLEM Algorithm for Photon-Emission Imaging Systems

The image reconstruction can be considered as a parameter estimation problem, in which method of maximum likelihood is widely used. The gamma-ray source distribution is regarded as the parameters to be estimated in this problem, and the maximum likelihood estimation of the source distribution is the one with the maximum probability to generate the measured data, i.e.

$$\hat{\mathbf{f}} = \arg \max_{\mathbf{f} \geq 0} \Pr[\mathbf{g}|\mathbf{f}] \quad (5.38)$$

in which, $\mathbf{g} = \{g_1, g_2, \dots, g_I\}$ is the measurement, and g_i stands for the number of counts measured as event i , $\mathbf{f} = \{f_1, f_2, \dots, f_J\}$ is the source distribution that we want to estimate. We put a constrain here that the estimates $\hat{\mathbf{f}}$ must be positive.

Most of the gamma-ray imaging systems can be simplified by a linear model illustrated in Fig. 5.13. The imaging space \mathbf{J} is divided into J pixels, and is transformed by the system response function \mathbf{T} to generate the measured data, which is defined in the measurement space \mathbf{I} . The element t_{ij} in the system response function \mathbf{T} is the probability that a photon emitted from pixel j creates a recorded event i . The imaging space \mathbf{J} in our application is the 4π directional space. A event i in the measurement space includes both the position and the energy information of a measured multi-pixel event.

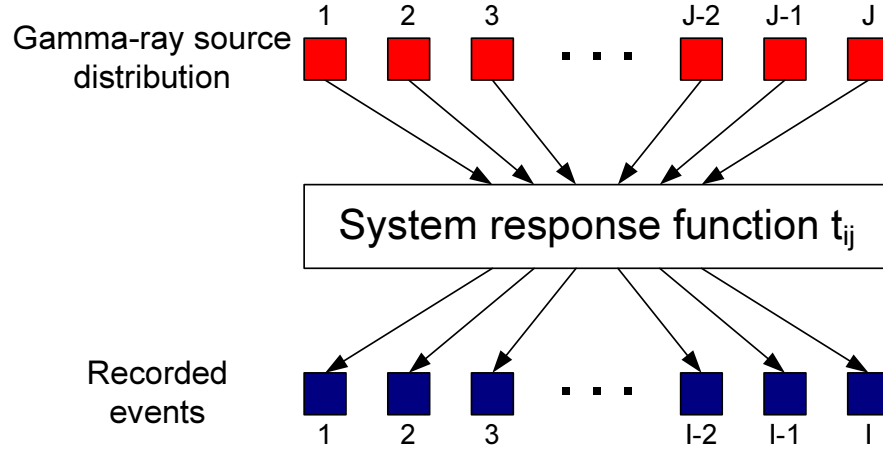


Figure 5.13: A linear imaging system.

With enough statistics and the linear model, the problem is simplified to I simultaneous equations:

$$\mathbf{T}\mathbf{f} = \mathbf{g} \quad (5.39)$$

Basically, the above problem is similar to the transmission tomography problem[67] and it is tempting for one to solve the problem with the well-established algorithms developed for transmission tomography[68, 69]. However, as Shepp pointed out[70], the attempts to solve Eq. 5.39 would be futile mostly due to the low count rates intrinsic to photon-emission imaging systems. The statistical noise will be amplified if one tries to solve 5.39 directly. The maximum likelihood method tries to solve Eq. 5.39 from a statistical point of view and can provide a much less noisy solution. To find the maximum likelihood solution of the problem, the likelihood of observing \mathbf{g} given \mathbf{f} must be derived first.

In the following discussion, we assume that the data is collected for a given time, which is also referred to as preset time assumption. Another assumption about the data collection time is preset counts, which means that the measurement is stopped when a certain number of counts is reached. The main difference between these two assumptions is that the total number of measured events is a random variable for

preset time, while it is a constant for preset counts.

Under the preset time assumption, the number of photons emitted from each pixel in \mathbf{J} is a Poisson random variable. f_j then represents the mean value of that Poisson random variable.

For each photon emitted from a specific pixel j , it has a probability t_{ij} to be recorded as event i . From counting statistics we know that the number of photons emitted from pixel j and recorded as event i is also a Poisson random variable with mean value of $t_{ij}f_j$. Since the numbers of photons emitted from different pixels are independent of each other, and since the sum of independent Poisson random variables is still Poisson, the total number of photons recorded as event i is a Poisson random variable with mean value of

$$\bar{g}_i = \sum_{j=1}^J t_{ij} f_j \quad (5.40)$$

Therefore, the probability to observe g_i counts as event i is

$$\Pr[g_i|\mathbf{f}] = \exp(-\bar{g}_i) \frac{(\bar{g}_i)^{g_i}}{g_i!} \quad (5.41)$$

In most detector systems, g_1, g_2, \dots, g_I are independent random variables. As a result, the probability to observe measurement \mathbf{g} given the source distribution \mathbf{f} is

$$\Pr[\mathbf{g}|\mathbf{f}] = \prod_{i=1}^I \Pr[g_i|\mathbf{f}] = \prod_{i=1}^I \exp(-\bar{g}_i) \frac{(\bar{g}_i)^{g_i}}{g_i!} \quad (5.42)$$

As we can see, the likelihood is a function of the source distribution \mathbf{f} . Since the likelihood function is positive definite, to simplify the problem, we can maximize the logarithmic likelihood instead of maximizing Eq. 5.42 directly. The logarithmic likelihood is

$$\begin{aligned} L(\mathbf{g}|\mathbf{f}) &= \ln \Pr(\mathbf{g}|\mathbf{f}) = \sum_{i=1}^I [-\bar{g}_i + g_i \ln(\bar{g}_i) - \ln(g_i!)] \\ &= \sum_{i=1}^I \left[-\sum_{j=1}^J t_{ij} f_j + g_i \ln\left(\sum_{j=1}^J t_{ij} f_j\right) - \ln(g_i!) \right] \end{aligned} \quad (5.43)$$

To maximize the log likelihood, the most straightforward way is to take its derivative and let it be zero, i.e.

$$\frac{\partial L(\mathbf{g}|\mathbf{f})}{\partial f_j} = -\sum_{i=1}^I t_{ij} + \sum_{i=1}^I \frac{g_i t_{ij}}{\sum_{j'=1}^J t_{ij'} f_{j'}} = 0 \quad (5.44)$$

The sum of $\sum_{i=1}^I t_{ij}$ is the probability that a photon emitted from pixel j is detected as any event i , i.e., the probability that the photon is detected at all. This sum represents the sensitivity of the detector system to the photons emitted from pixel j , and is denoted s_j . s_j is also referred to as the sensitivity image. Therefore, Eq. 5.44 becomes

$$\frac{\partial L(\mathbf{g}|\mathbf{f})}{\partial f_j} = -s_j + \sum_{i=1}^I \frac{g_i t_{ij}}{\sum_{j'=1}^J t_{ij'} f_{j'}} = 0 \quad (5.45)$$

If \mathbf{f} is a local maximum point of function $L(\mathbf{g}|\mathbf{f})$, it must satisfy Eq. 5.45. However, Eq. 5.45 is not a linear equation and is extremely difficult to be solved directly. A popular method to maximize the log likelihood function of Eq. 5.43 is the expectation maximization algorithm[71, 70], which requires iterative calculations. In each iteration, the algorithm consists of two steps which are called the expectation step and the maximization step. In the photon emission imaging applications, the expectation step calculates the expected value of the source distribution given the measurement \mathbf{g} and the previous estimation of the source distribution $\hat{\mathbf{f}}^k$. Then the maximum likelihood estimation of the source distribution is calculated based on this expected value.

For a photon detected as event i , it can come from many pixels in the imaging space J . Given the k^{th} estimation of the source distribution, the probability for the photon to be emitted from pixel j is

$$\Pr[j|i] = \frac{t_{ij} \hat{f}_j^k}{\sum_{j'=1}^J t_{ij'} \hat{f}_{j'}^k} \quad (5.46)$$

The measurement gives g_i counts as event i . For each of those g_i events, it has the probability defined by Eq. 5.46 to originate from pixel j . Therefore, within all of those g_i events, n_{ij} , which is the number of photons that were emitted from pixel j , follows a multinomial distribution of

$$\Pr[n_{ij}|g_i, \hat{\mathbf{f}}^k] = \frac{g_i!}{n_{ij}!(g_i - n_{ij})!} \Pr[j|i]^{n_{ij}} (1 - \Pr[j|i])^{g_i - n_{ij}} \quad (5.47)$$

The mean value of n_{ij} is

$$\mathbb{E}[n_{ij}|g_i, \hat{\mathbf{f}}^k] = g_i \Pr[j|i] \quad (5.48)$$

The mean value of the total number of photons that were emitted from pixel j and detected by the detector is

$$\mathbb{E}[n_j|\mathbf{g}, \hat{\mathbf{f}}^k] = \sum_{i=1}^I \mathbb{E}[n_{ij}|g_i, \hat{\mathbf{f}}^k] = \sum_{i=1}^I g_i \frac{t_{ij} \hat{f}_j^k}{\sum_{j=1}^J t_{ij} \hat{f}_j^k} = \hat{f}_j^k \sum_{i=1}^I \frac{g_i t_{ij}}{\sum_{j=1}^J t_{ij} \hat{f}_j^k} \quad (5.49)$$

The above equation is the mean value of n_j given the measurement and the previous estimation of the source. We can consider Eq. 5.49 as an observation of the number of photons that were emitted from pixel j and detected. Since n_j is a Poisson random variable, the maximum likelihood estimation of its mean value is just its observed value, i.e.

$$\hat{n}_j = \hat{f}_j^k \sum_{i=1}^I \frac{g_i t_{ij}}{\sum_{j'=1}^J t_{ij'} \hat{f}_{j'}^k} \quad (5.50)$$

As defined, \bar{n}_j is the average number of detected photons, and f_j is the average number of emitted photons. Therefore, the next estimation of f_j is

$$\hat{f}_j^{k+1} = \frac{\hat{n}_j}{s_j} = \frac{\hat{f}_j^k}{s_j} \sum_{i=1}^I \frac{g_i t_{ij}}{\sum_{j'=1}^J t_{ij'} \hat{f}_{j'}^k} \quad (5.51)$$

The above iterative equation is the MLEM algorithm for photon emission imaging applications. However, Eq. 5.51 is not the only form of the MLEM algorithm

for photon-emission imaging problems. Depending on different approaches in the expectation and maximization steps, the MLEM algorithm could appear in different forms[72].

5.3.2 Properties of the MLEM algorithm

5.3.2.1 Conservation of counts

From Eq. 5.51, we can get

$$\begin{aligned}
 \sum_{j=1}^J \hat{f}_j^{k+1} s_j &= \sum_{j=1}^J \hat{f}_j^k \sum_{i=1}^I \frac{g_i t_{ij}}{\sum_{j'=1}^J t_{ij'} \hat{f}_{j'}^k} \\
 &= \sum_{i=1}^I \frac{\sum_{j=1}^J \hat{f}_j^k g_i t_{ij}}{\sum_{j'=1}^J t_{ij'} \hat{f}_{j'}^k} \\
 &= \sum_{i=1}^I g_i
 \end{aligned} \tag{5.52}$$

which means that no matter what the start image is, the sum of the estimation of the detected photons is preserved to be the total number of measured photons.

5.3.2.2 Positivity

If the start image is positive ($f_j^k > 0$ for all j), it can be seen from Eq. 5.51 that $f_j^{k+1} > 0$ unless $g_i t_{ij} = 0$ for all i . The next estimation f_j^{k+1} is zero only when $g_i t_{ij} = 0$ for all i . In this case, if there are events measured as event i ($g_i \neq 0$), t_{ij} must be zero. This means that the probability for a photon from pixel j to create any of the measured events is zero. In other words, the measurement does not detect any event that is possibly from pixel j . Reasonably, in this case, the activity from pixel j should be estimated to be zero. Otherwise, the next estimation of the source is always positive.

5.3.2.3 Convergence

Dempster proved that the EM algorithm has the property of

$$L(\mathbf{g}|\mathbf{f}^{k+1}) \geq L(\mathbf{g}|\mathbf{f}^k) \quad (5.53)$$

which ensures the convergence of the algorithm[71]. The equality holds only when $\mathbf{f}^{k+1} = \mathbf{f}^k$.

Eq. 5.53 alone can not guarantee the algorithm converges to a maximum point of the log likelihood function. However, it can be proven that if $\hat{\mathbf{f}}$ is the convergence point, $\hat{\mathbf{f}}$ is also a maximum point[70, 73, 74, 75], given the condition that all components of the initial guess \mathbf{f}^0 are positive. This property can be illustrated by the following not-so-strict argument.

If Eq. 5.51 converges, which implies the difference between \mathbf{f}^{k+1} and \mathbf{f}^k is infinitely small given k is large enough, and if $\mathbf{f}_j^{k+1} \neq 0$ for all j , from Eq. 5.45 we will have $\frac{\partial L(\mathbf{g}|\mathbf{f})}{\partial f_j} = 0$. It means that if the MLEM method converges, the solution must be at a local maximum or minimum point of the log likelihood function.

A sufficient and necessary condition for the log likelihood function $L(\mathbf{g}|\mathbf{f})$ of Eq. 5.43 to be concave is that the matrix of second derivatives of $L(\mathbf{g}|\mathbf{f})$ is negative semidefinite[76]. This condition requires that for an arbitrary nonzero vector \mathbf{f}' , we have

$$\sum_{j_1=1}^J \sum_{j_2=1}^J f'_{j_1} f'_{j_2} \frac{\partial^2 L(\mathbf{g}|\mathbf{f})}{\partial f_{j_1} \partial f_{j_2}} \leq 0 \quad (5.54)$$

From Eq. 5.45, we have

$$\frac{\partial^2 L(\mathbf{g}|\mathbf{f})}{\partial f_{j_1} \partial f_{j_2}} = - \sum_{i=1}^I \frac{g_i t_{ij_1} t_{ij_2}}{\left[\sum_{j'=1}^J t_{ij'} f_{j'} \right]^2} \quad (5.55)$$

Therefore, the left part in Eq. 5.54 is

$$\begin{aligned}
\sum_{j_1=1}^J \sum_{j_2=1}^J f'_{j_1} f'_{j_2} \frac{\partial^2 L(\mathbf{g}|\mathbf{f})}{\partial f_{j_1} \partial f_{j_2}} &= - \sum_{j_1=1}^J \sum_{j_2=1}^J f'_{j_1} f'_{j_2} \sum_{i=1}^I \frac{g_i t_{ij_1} t_{ij_2}}{\left[\sum_{j'=1}^J t_{ij'} f'_{j'} \right]^2} \\
&= - \sum_{i=1}^I g_i \frac{\left[\sum_{j'=1}^J t_{ij'} f'_{j'} \right]^2}{\left[\sum_{j'=1}^J t_{ij'} f'_{j'} \right]^2}
\end{aligned} \tag{5.56}$$

From the above equation it can be seen that the sufficient and necessary condition of Eq. 5.54 for $L(\mathbf{g}|\mathbf{f})$ to be concave holds. As a result, there is no minimum point for $L(\mathbf{g}|\mathbf{f})$, and all maxima of $L(\mathbf{g}|\mathbf{f})$ are global maxima. Therefore, it can be concluded that if Eq. 5.51 converges, the solution is a global maximum point.

5.3.2.4 Uniqueness of the MLEM solution

The concavity of the log likelihood function does not imply the uniqueness of the maximum points. In fact, the non-uniqueness of the maximum points can occur if and only if Eq. 5.56 equals zero, which implies there exists a non-zero \mathbf{f}' that for each i , we have

$$\frac{\sqrt{g_i}}{\sum_{j'=1}^J t_{ij'} f'_{j'}} \sum_{j'=1}^J t_{ij'} f'_{j'} = 0 \tag{5.57}$$

Such \mathbf{f}' exists if and only if the I vectors

$$\frac{\sqrt{g_i}}{\lambda_i} \{t_{i1}, t_{i2}, \dots, t_{iJ}\} \tag{5.58}$$

span the J -dimensional Euclidean space. In the above equation, $\lambda_i = \sum_{j'=1}^J t_{ij'} f'_{j'}$, which is the average number of counts detected as event i given the source \mathbf{f} . In

other words, the rank of the matrix

$$\begin{bmatrix} \frac{\sqrt{g_1}}{\lambda_1} t_{11} & \frac{\sqrt{g_1}}{\lambda_1} t_{12} & \frac{\sqrt{g_1}}{\lambda_1} t_{13} & \dots & \frac{\sqrt{g_1}}{\lambda_1} t_{1J} \\ \frac{\sqrt{g_2}}{\lambda_2} t_{21} & \frac{\sqrt{g_2}}{\lambda_2} t_{22} & \frac{\sqrt{g_2}}{\lambda_2} t_{23} & \dots & \frac{\sqrt{g_2}}{\lambda_2} t_{2J} \\ \frac{\sqrt{g_3}}{\lambda_3} t_{31} & \frac{\sqrt{g_3}}{\lambda_3} t_{32} & \frac{\sqrt{g_3}}{\lambda_3} t_{33} & \dots & \frac{\sqrt{g_3}}{\lambda_3} t_{3J} \\ \dots & \dots & \dots & \dots & \dots \\ \frac{\sqrt{g_I}}{\lambda_I} t_{I1} & \frac{\sqrt{g_I}}{\lambda_I} t_{I2} & \frac{\sqrt{g_I}}{\lambda_I} t_{I3} & \dots & \frac{\sqrt{g_I}}{\lambda_I} t_{IJ} \end{bmatrix} \quad (5.59)$$

should be equal to or greater than J for the maximum point to be unique. Therefore, a necessary condition for the maximum point to be unique is that the total number of possible measurement outputs I is equal to or greater than the number of pixels J .

The total number of the measured events m can be obtained by summing g_i over all i , $m = \sum_{i=1}^I g_i$. The number of the non-zero components in the measurement \mathbf{g} is less than or equal to m . Therefore, the rank of the matrix 5.59 is less than or equal to m . As a result, another necessary condition for the maximum point to be unique is that the total number of the measured events is equal to or greater than the number of pixels J .

5.3.3 The List-Mode MLEM Algorithm

In the MLEM algorithm's general equation of Eq. 5.51, it is required to sum over all the possible measurement output i . In a single 3-D CdZnTe detector, if the depth is separated into 10 bins and the energy is represented by 1 keV per channel, for a system with dynamic range of 1 MeV, it requires $121 \times 10 \times 1000 \approx 10^6$ bins to store a single gamma-ray interaction. For a two-pixel events, the number of the required bins becomes 10^{12} , which is far beyond the memory limitation in modern computers. Instead of impractically storing the measurement result into binned data, an alternative way is to store the measured attributes of each event in a list. This

data storage mode is called list mode[77]. In list mode, the measurement can be represented by a set of ordered events, $\{i_1, i_2, \dots, i_M\}$.

In reality, the number of measured events is far less than the total number of bins. Therefore, the measurement \mathbf{g} is a very sparse vector with elements mostly zeros and ones. The list mode MLEM algorithm can be easily obtained by replacing g_i in Eq. 5.51 by ones for those measured events. As a result, the sum over all possible measurement output becomes the sum over all measured events, i.e.

$$\hat{f}_j^{k+1} = \frac{\hat{f}_j^k}{s_j} \sum_{i=1}^M \frac{t_{ij}}{\sum_{j'=1}^J t_{ij'} \hat{f}_{j'}^k} \quad (5.60)$$

The log likelihood of list-mode data is[77]

$$L_{\text{list}}(\mathbf{g}|\mathbf{f}) = -\ln(M!) - \sum_{j=1}^J s_j f_j + \sum_{i=1}^M \ln\left(\sum_{j=1}^J t_{ij} f_j\right) \quad (5.61)$$

5.3.4 Performance

The list-mode MLEM algorithm was first applied to the single 3-D CdZnTe detector by Lehner[30]. In Lehner's work, the sequence reconstruction was applied to each event and the events with smaller angular uncertainties were given more weight to accelerate the convergence speed. Although the sequence reconstruction and the weighting method seem to be able to achieve better angular resolution, neither of them was applied in the MLEM algorithm in this work. The sequence reconstruction algorithm selects one of the sequences with the higher probability, and discards the other sequence which could still be physically possible. Both sequences are part of the system response function and should be included in the complete system response function model. The weighting method tries to take advantage of those events with better angular resolution. However, this method is equivalent to applying weighting factors on the system response function. Applying the sequence reconstruction algorithm or the weighting method is equivalent to using an incomplete system response

function in the MLEM algorithm and might introduce artifacts or biases in the reconstructed image. The system response function used in this work includes both possible sequences, and no weighting factor is applied to each event. The system response function model is described in Section 6.2.1.

Both simulated and measured data described in Section 5.2.5 were reconstructed by the list-mode MLEM algorithm. Fig. 5.14 and Fig. 5.15 show the reconstructed images of the MLEM algorithm. For comparison, the simple back-projection and the filtered back-projection images are also shown.

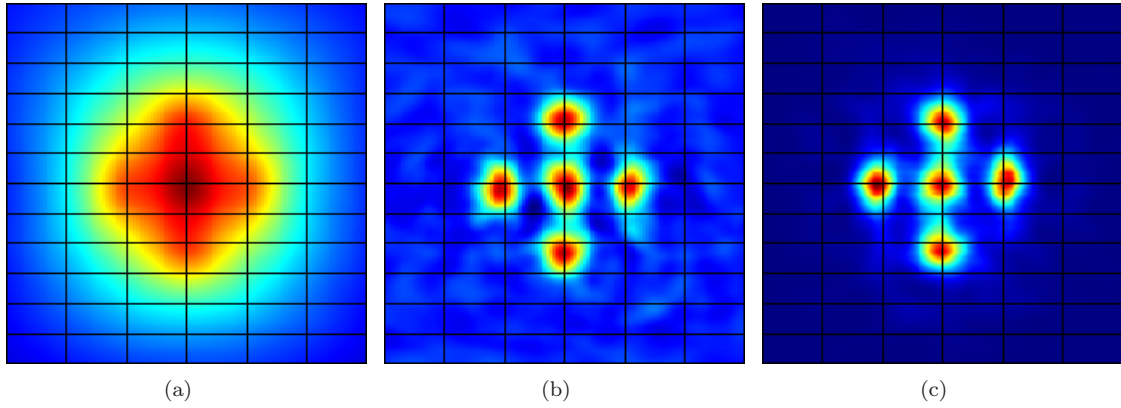


Figure 5.14: Reconstructed images of the simulated data with five Cs-137 point sources. (a). Simple back-projection. (b). Filtered back-projection with the simulated PSF shown in Fig. 5.10. (c). MLEM reconstructed image after 24 iterations.

It can be seen from Fig. 5.14 and Fig. 5.15 that the MLEM reconstructed images are better than the filtered back-projection images in terms of the signal-to-noise ratio and angular resolution. For a single Cs-137 point source, the angular resolution of the reconstructed image at the 24th iteration is about 10° and 14° in the azimuthal and lateral directions, respectively.

For the simulated data with five Cs-137 point sources, the convergence speed is shown in Fig. 5.16. The log likelihood is calculated by Eq. 5.61. The difference

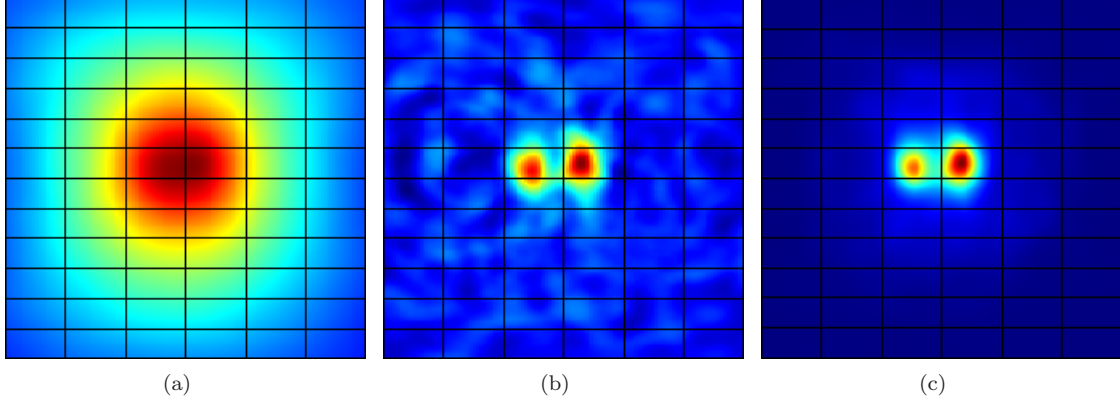


Figure 5.15: Reconstructed images of the measured data with two Cs-137 point sources separated by 15 degrees. (a). Simple back-projection. (b). Filtered back-projection with the simulated PSF shown in Fig. 5.10. (c). MLEM reconstructed image after 24 iterations.

between two images is defined as

$$D = \sum_j^J \left| \hat{f}_j^{k+1} - \hat{f}_j^k \right| \quad (5.62)$$

It can be seen that the log likelihood increases quickly in the first few iterations. However, the convergence speed slows down dramatically after the first few iterations. By using the filtered back-projection image as the start image, the improvement on the convergence speed is very limited.

The termination point of the MLEM algorithm is controversial. Various termination criteria have been proposed[49]. Although the angular resolution for a point source tends to improve as the number of iterations increases, the noise in the reconstructed image also increases. This is because the measurement itself is a statistical process and has noise inherently. If the statistics in the measurement is poor, the convergence point of the MLEM algorithm often differs from the true source distribution significantly, and usually the maximum likelihood solution is not desired. The convergence speed depends on both the number of measured events and the spatial distribution of the source. As a result, it is difficult to set a criteria to stop the iterations. In this study, we found that with enough counts, the reconstructed im-

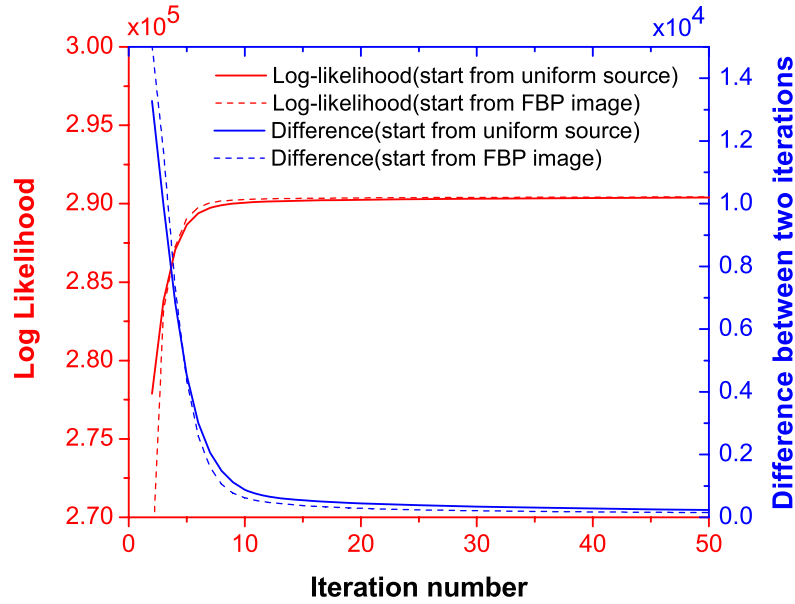


Figure 5.16: Convergence speed of the MLEM algorithm on the simulated data with five point Cs-137 sources. The red curves show the log likelihood as a function of number of iterations. The blue curves show the difference between the current image and the previous image.

ages of point sources look good enough after about 20 iterations. Further iterations improve the image very slowly and artifacts tend to appear. Therefore, in this work, all images reconstructed by the MLEM algorithm are stopped after 24 iterations.

5.4 3-D Imaging

When back-projecting the Compton cones onto the imaging sphere, the vertex of each cone is usually placed at the origin to simplify the geometrical calculation. This approximation is valid when the source-to-detector distance is large comparing with the detector size, thus is also referred to as “far field imaging”. However, if the source is in the vicinity of the detector, the displacement of the vertexes from the origin must be taken into account (Fig. 5.17). This technique is also referred to as “near field imaging”.

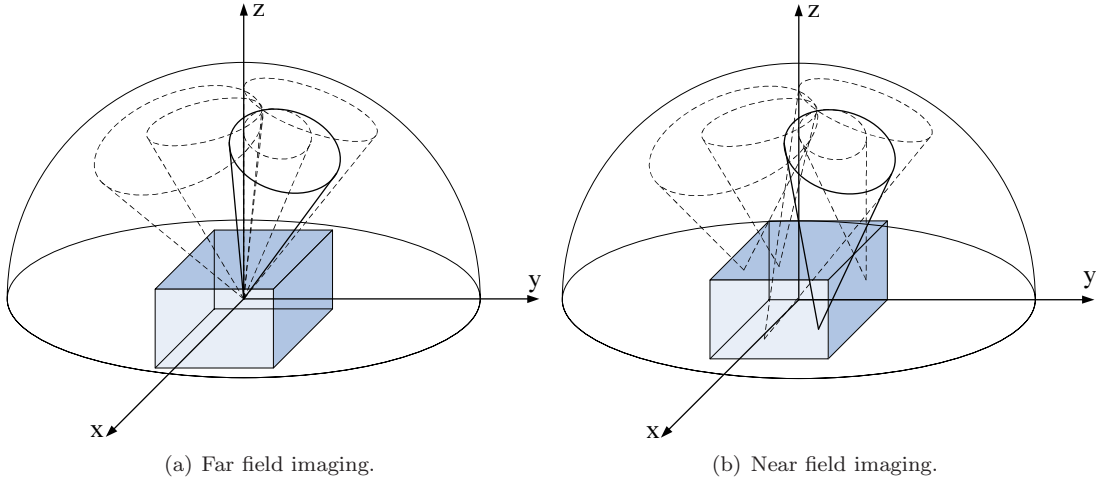


Figure 5.17: Illustration of the difference between far field imaging and near field imaging. In far field imaging, the vertex of each back-projection cone is approximately placed at the origin. In near field imaging, the vertex of each back-projection cone is placed at the first interaction position.

In far field imaging, the imaging space is the 4π directional space. In near field imaging, the vertex of the back-projection cone is placed at the position of the first interaction. As a consequence, one must specify the radius of the 4π imaging sphere. This radius is referred to as the “focus distance”. The reconstructed image of any source not on the focus distance will be blurred.

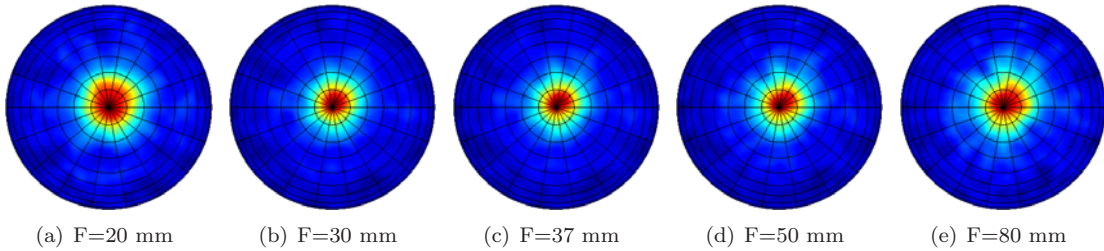


Figure 5.18: Reconstructed images at different focus distance. The measurement was taken with a Cs-137 point source placed 37 mm above the detector. The images were reconstructed using the filtered back-projection algorithm, and this figure shows the upper hemispheres.

Fig. 5.18 shows the images reconstructed at different focus distances for the same measurement. Fig. 5.19 shows the image resolution at different focus distances. It can be seen that when the focus distance is at 37 mm, which is the true source-to-

detector distance, the reconstructed image has the best resolution.

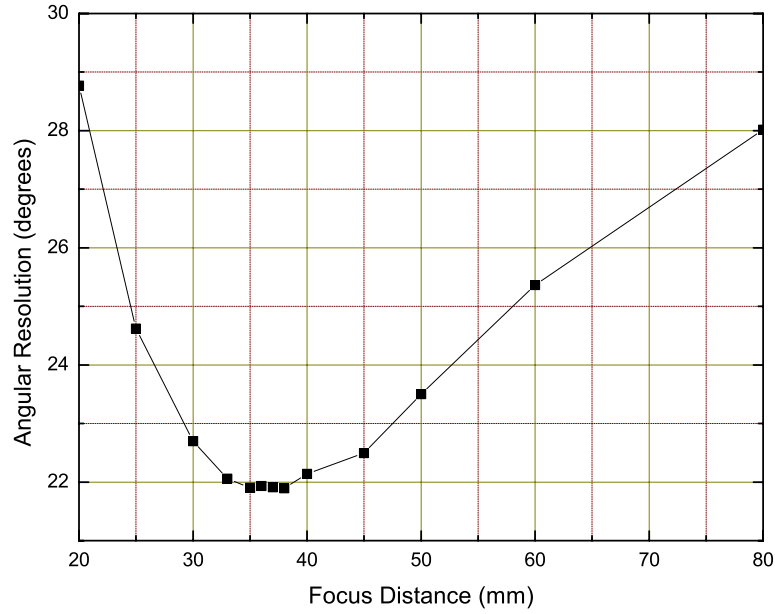


Figure 5.19: Image resolution versus focus distance.

It is possible to back project the cones into the 3-D space instead of the 4π sphere. Therefore, 3-D imaging can be realized with near field imaging at the cost of more storage space and more computation time. The measured data of a Cs-137 point source above the detector was reconstructed with 3-D imaging technique using the MLEM algorithm, and the result is shown in Fig. 5.20. The image indicates that a single 3-D CdZnTe detector can not only do 2-D imaging, it can also provide the source to detector distance. The resolution in radial direction is mostly limited by the size of the detector, which is only $15\text{ mm} \times 15\text{ mm} \times 10\text{ mm}$.

If detectors are arranged into arrays to form larger detecting dimensions, such as the Polaris systems currently under development, better 3-D imaging performance can be expected. A simulation was run to demonstrate the 3-D image capability of the Polaris system. There were 9 $15\text{ mm} \times 15\text{ mm} \times 10\text{ mm}$ detectors forming a 3×3

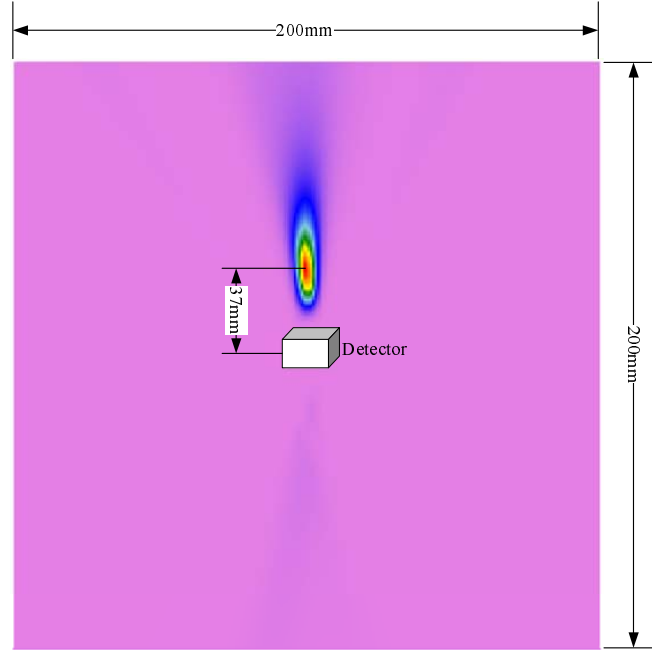


Figure 5.20: A vertical slice of the 3-D imaging space, which is a $200\text{ mm} \times 200\text{ mm} \times 200\text{ mm}$ cube around the detector. The measurement was taken with a Cs-137 point source placed 37 mm above the detector. The reconstruction algorithm was MLEM and was stopped after 24 iterations.

array in the simulation, and the gap between detectors was 5 mm . A $50\text{ mm} \times 35\text{ mm}$ “M” shape Cs-137 source was placed 20 mm above the upper surface of the detector array, as shown in Fig. 5.21. The gamma-ray source was uniformly distributed on the “M” shape. The imaging space was an $80\text{ mm} \times 80\text{ mm} \times 40\text{ mm}$ 3-D space above the detector array.

The reconstructed image is shown in Fig. 5.22. The “M” shape source can be clearly identified in this simulation.

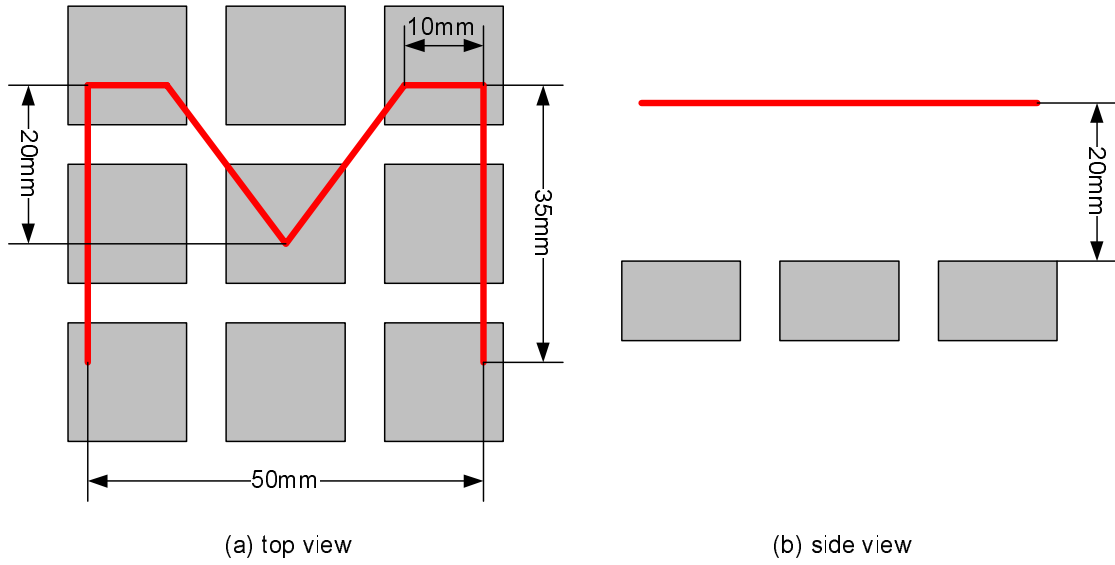


Figure 5.21: The geometry configuration of the simulation in which a Cs-123 source uniformly distributed on a “M” shape was placed 20 mm above a 3×3 array of 3-D CdZnTe detectors.

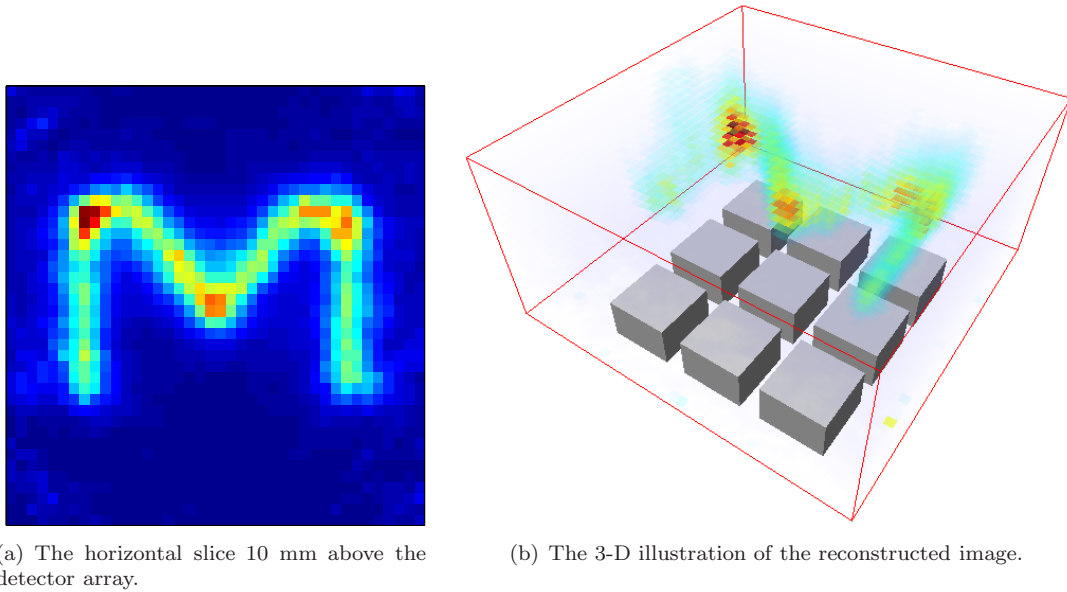


Figure 5.22: Reconstructed image of the “M” shape Cs-137 source above a 3×3 array of 3-D CdZnTe detectors. The MLEM algorithm was used and was stopped after 24 iterations.

CHAPTER VI

ENERGY-IMAGING INTEGRATED DE-CONVOLUTION

6.1 Spectral Deconvolution in Energy Space

Because of the various interaction mechanisms of gamma-rays with detectors, the measured spectra usually consist of various features, such as photo-peaks, Compton continua, and back scattering peaks. The task of spectral deconvolution is to estimate the incident gamma-ray energy spectrum given the measured “energy loss” spectrum and the detector response function. The spectral deconvolution problem is also known as spectral unfolding or spectral inversion.

The way that an incident gamma-ray spectrum produces an energy loss spectrum can be represent by[78]

$$d(E) = \int_0^{\infty} T(E, E_0)f(E_0)dE_0 \quad (6.1)$$

in which $f(E_0)$ is the incident spectrum, $d(E)$ is the observed spectrum, and $T(E, E_0)$ is the detector response function.

In reality, a detector has a finite dynamic range, and gives the measured counts in a fixed number of channels. As a result, the measured spectrum $d(E)$ is a discrete spectrum. Although the incident spectrum $f(E_0)$ is continuous, it is difficult to obtain information of $f(E_0)$ with structure finer than the channel width in the measurement. Therefore, $f(E_0)$ is usually discretized in the deconvolution. Eq. 6.1

thus can be expressed in a discrete form of

$$\mathbf{d} = \mathbf{T} \cdot \mathbf{f} \quad (6.2)$$

in which \mathbf{T} is also known as the system response matrix.

The deconvolution problem is to solve Eq. 6.2 given the measured spectrum \mathbf{d} and the system response \mathbf{T} . However, the solution may not be unique because there may exist solutions which satisfy $\mathbf{T}\mathbf{f}_0 = 0$. In this case, any solution \mathbf{f}_0 added to a solution \mathbf{f} is also a solution. Moreover, the solution that best satisfies Eq. 6.2 may be contrary to our a priori knowledge about the incident gamma-ray spectrum, e.g. it must be positive, conserve counts, be continuous, etc.[78] All of the above difficulties make the spectral deconvolution a complicated problem. Various algorithms have been proposed and studied, such as the Singular Value Decomposition (SVD), the Backus-Gilbert method[79, 80], the Linear Regularization method[81], the Maximum Entropy Method (MEM)[82], and the Maximum Likelihood method by Expectation Maximization (MLEM)[71]. Among these algorithms, the MLEM algorithm has been demonstrated to be advantageous[83]. Actually, it can be found that Eq. 6.2 is very similar to the image reconstruction problem of Eq. 5.39, except that the system response functions of the two problems differ from each other due to the different physics behind each problem. The MLEM algorithm described in Section 5.3 can be directly applied to the spectral deconvolution problem.

The system response function \mathbf{T} was obtained by Geant4 simulations. In the simulations, a single 3-D position-sensitive CdZnTe detector was operated as a spectrometer, and the sources were placed at one side of the detector. No surrounding material was included in the simulations, and as a result, there is no back scattering peak in the system response function. Fig. 6.1 shows the system responses at several selected incident gamma-ray energies.

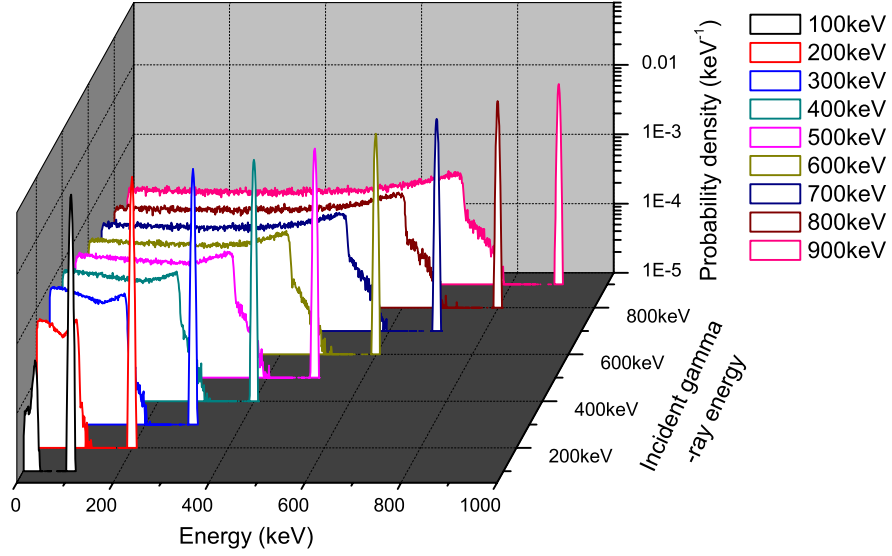


Figure 6.1: Simulated energy response functions at different incident gamma-ray energies.

In the experiment, a ^{137}Cs , a ^{22}Na , and a ^{133}Ba source were placed at three different sides of a single 3-D CdZnTe detector as shown in Fig. 6.2. The measured raw spectrum of all events is shown in the top figure in Fig. 6.3, in which a Compton continuum is clearly present.

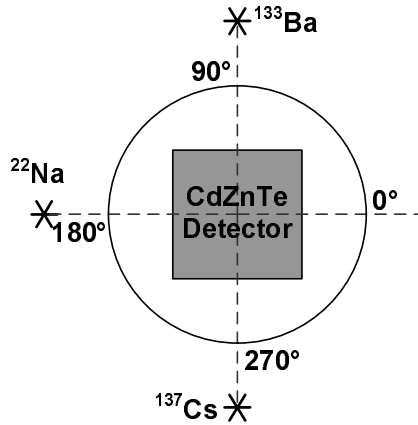


Figure 6.2: Experiment setup. Three point sources (a ^{137}Cs , a ^{22}Na and a ^{133}Ba) were placed at three different sides of the 3-D CdZnTe detector..

After the energy spectral deconvolution, the deconvolved spectrum is shown in the bottom figure in Fig. 6.3. As we can see, most of the Compton background was removed by the deconvolution. There is still a continuum between 100 keV and 300

keV, which is mostly caused by those photons scattered outside the detector.

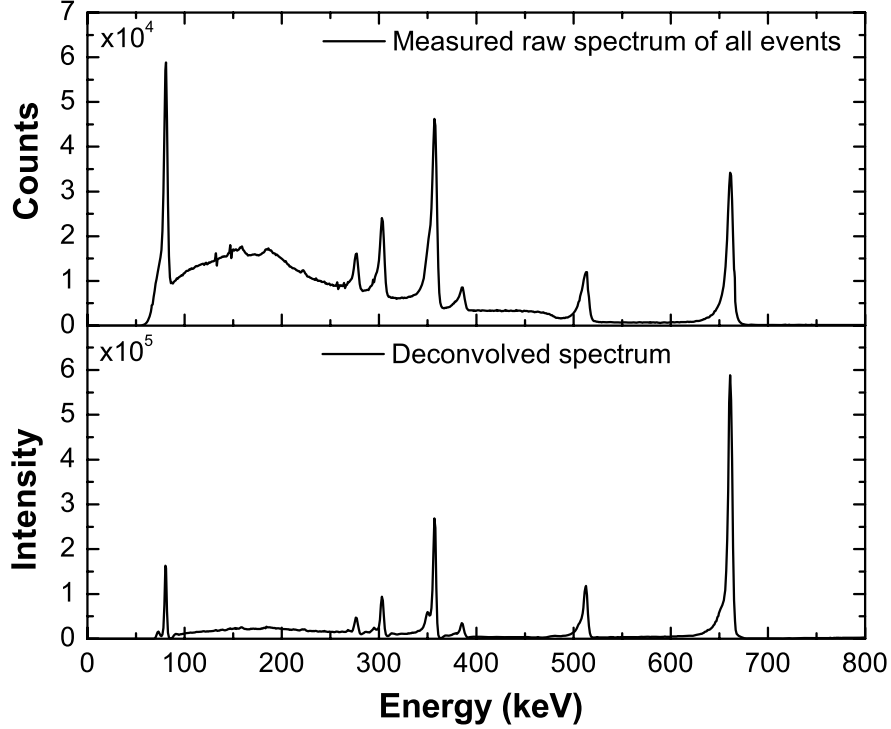


Figure 6.3: Energy spectral deconvolution on the measured spectrum with three point sources. The top figure shows the measured raw spectrum of all events. The bottom figure shows the deconvolved spectrum.

6.2 Energy-Imaging Integrated Deconvolution

From Fig. 6.3, we can see that the background of the photons scattered outside the detector can not be removed by energy spectral deconvolution because back-scattering was not modeled in the system response function. In order to model the back-scattering, the surrounding materials must be included in the simulations. This imposes a difficulty in the energy spectral deconvolution because the operation environment could change for a hand-held gamma-ray detector. Furthermore, since the system responses of most actual gamma-ray detectors depend on the incident gamma-ray direction, the spectral deconvolution methods are fundamentally vulnerable to spatially distributed sources.

In the 3-D position-sensitive CdZnTe detectors, the interaction position information can provide extra information about the direction of the incident gamma-rays. Therefore, the detector system response function can be modeled as a function of both the incident gamma-ray direction and energy. In this work, a new energy-imaging integrated deconvolution algorithm is proposed. The deconvolution space is defined as a combined space of both energy and spatial dimensions. By this mean, this method can simultaneously provide the source image at any gamma-ray energy, as well as the gamma-ray energy spectrum at any incident direction.

This energy-imaging integrated deconvolution algorithm removes the difficulty of the system response function dependence on the incident gamma-ray direction. On the other hand, the new algorithm will also benefit the imaging part. In conventional Compton imaging systems, it is sometimes assumed that the incident gamma-ray energy is known a priori. To reduce the Compton background, an image is typically reconstructed only from those events within a narrow energy window. However, in many applications, the incident gamma-ray energy is unknown, or the energy spectrum is continuous, and it is unlikely to set an energy window to select the full-energy events. Therefore, the reconstructed image is degraded by the Compton background, in which only a fraction of the incident gamma-ray energy is deposited within the detector. Even if the incident gamma-ray energy is known, in the case of multiple sources, the low-energy photopeak is contaminated by the Compton background from the high-energy sources, and the reconstructed image of the low-energy gamma-rays is affected by the distribution of the high-energy gamma-rays. Furthermore, although the back-projection rings of the Compton background do not pass the true source direction, those background events still contain information about the source distribution. Therefore, there will be a waste in efficiency if only full-energy events are

reconstructed. The new energy-imaging integrated deconvolution algorithm considers all the possibilities in the system response function model. Therefore, all of the measured events can contribute to the deconvolution. As a result, the energy-imaging integrated deconvolution algorithm does not require the a priori knowledge about the incident gamma-rays. The algorithm is also efficient, free of Compton background, and provides the best estimation of the incident gamma-rays.

6.2.1 Modeling of the System Response Function

In the energy-imaging integrated deconvolution algorithm, a source pixel \mathbf{j} is defined in a combined space of both spatial and energy dimensions, and a measurement \mathbf{i} is defined by two sets of position and energy information. Suppose the position is defined by an $11 \times 11 \times 10$ matrix, and the energy is divided into 1000 channels, there will be more than 10^6 bins in each set of position and energy information. A Compton scattered event requires at least two sets of position and energy information. As a result, 10^{12} bins are required to store the measurement output. On the other hand, in the imaging space, suppose the 4π directional space is divided into 16×16 pixels, and the energy space is divided into 500 channels. The whole imaging space thus has about 10^5 pixels. As a result, the system response function for the 3-D position-sensitive CdZnTe detector has more than 10^{17} elements, which is beyond the limit of any memory system currently available.

Because of the huge number of possible measurement events, it is impossible to pre-calculate the system response function t_{ij} by simulations. In this work, an analytical model was developed to calculate the system response function for each measured two-pixel event during the reconstruction process. This analytical approach considers the binning process and the uncertainties in an actual detector system. Since the imaging space includes the energy dimension, there are two possibilities for a photon

from an imaging pixel to create a measured event with two interactions. The first possibility is that the photon deposits all its energy in the detector by a Compton scattering followed by a photoelectric absorption. The other possibility is the photon deposits partial of its energy by two Compton scatterings and the scattered photon escapes. The system response function model should account for both possibilities.

The system response function t_{ij} is defined as the probability of a photon emitted from pixel \mathbf{j} to be observed as a measured event \mathbf{i} . The system response function t_{ij} therefore can be described as the probability of a photon with a certain energy emitted from a certain spatial direction to be observed as event \mathbf{i} .

The measurement data is usually binned due to pixellation or digitization. Therefore, the measurement result is actually a small bin volume around point \mathbf{i} in the measurement space. Before this binning process, the imperfect detector system will introduce uncertainties to the measurement quantities due to noise or Doppler broadening. Therefore, the system response function can be written as

$$t_{ij} = \int_{\Delta \mathbf{V}_i} d\hat{\mathbf{i}} \int f(\hat{\mathbf{i}}|\tilde{\mathbf{i}})f(\tilde{\mathbf{i}}|\mathbf{j})d\tilde{\mathbf{i}} \quad (6.3)$$

in which, $f(\tilde{\mathbf{i}}|\mathbf{j})$ is the probability density function for a photon from pixel \mathbf{j} to create a “real” event $\tilde{\mathbf{i}}$, which consists of the actual interaction positions and deposited energies, and $f(\hat{\mathbf{i}}|\tilde{\mathbf{i}})$ is the probability for the detector system to generate a response of $\hat{\mathbf{i}}$ due to uncertainties given the real event $\tilde{\mathbf{i}}$. $\Delta \mathbf{V}_i$ is the bin volume around measurement \mathbf{i} .

Our model will be based on this procedure to calculate the system response function. First, we will derive the probability density function $f(\tilde{\mathbf{i}}|\mathbf{j})$ for a photon emitted from pixel \mathbf{j} to create a real event $\tilde{\mathbf{i}}$. Then we will calculate the probability density function $f(\hat{\mathbf{i}}|\tilde{\mathbf{i}})$ for the detector system to output this event $\tilde{\mathbf{i}}$ to be $\hat{\mathbf{i}}$ in the measurement space due to measurement uncertainties, assuming all the uncertainties are

Gaussian. Finally, to obtain t_{ij} , the probability density function is integrated over the bin volume $\Delta \mathbf{V}_i$ around \mathbf{i} .

In this work, only two-interaction events are modeled. The system response function modeling for three or more interaction events can follow the same procedures but usually is much more complicated. The spatial domain in the imaging space is the 4π angular space around the detector, thus a source pixel in the energy-imaging integrated space is defined by $(E_0, \boldsymbol{\Omega}_0)$. The deconvolved image gives the incident gamma-ray intensity from a certain direction, which is irrelevant to the distance between the source and the detector. Therefore, it is reasonable to assume that the source is distributed on the surface of a sphere with radius R which is much greater than the dimension of the detector. As a result, a source pixel can also be described by (E_0, \mathbf{r}_0) , in which $\mathbf{r}_0 = R\boldsymbol{\Omega}_0$. The measurement event $\tilde{\mathbf{i}}$ and $\hat{\mathbf{i}}$ can be represented by $(\tilde{E}_1, \tilde{\mathbf{r}}_1, \tilde{E}_2, \tilde{\mathbf{r}}_2)$ and $(\hat{E}_1, \hat{\mathbf{r}}_1, \hat{E}_2, \hat{\mathbf{r}}_2)$, respectively. Fig. 6.4 illustrates a two-interaction event. d_1 is the distance that the incident photon travels before reaching the first interaction position, d is the distance between the two interaction positions, and d_2 is the distance that the escaping photon travels before leaving the detector.

6.2.1.1 Probability density function of $f(\tilde{\mathbf{i}}|\mathbf{j})$

In a measured event, if two interactions are observed by the detector system, the first interaction is always a Compton scattering. For the second interaction, there are two possibilities, which are another Compton scattering or a photoelectric absorption.

Define $\tilde{\boldsymbol{\Omega}}_1 = \frac{\tilde{\mathbf{r}}_1 - \mathbf{r}_0}{|\tilde{\mathbf{r}}_1 - \mathbf{r}_0|}$, and $\tilde{\boldsymbol{\Omega}}_2 = \frac{\tilde{\mathbf{r}}_2 - \tilde{\mathbf{r}}_1}{|\tilde{\mathbf{r}}_2 - \tilde{\mathbf{r}}_1|}$, which are the directions of the incident and scattered photons. We will have the conditional probability of

$$f(\tilde{\boldsymbol{\Omega}}_2|E_0, \tilde{E}_1, \tilde{\boldsymbol{\Omega}}_1) = \frac{\delta(\theta_r - \theta_e)}{2\pi \sin \theta_e} \quad (6.4)$$

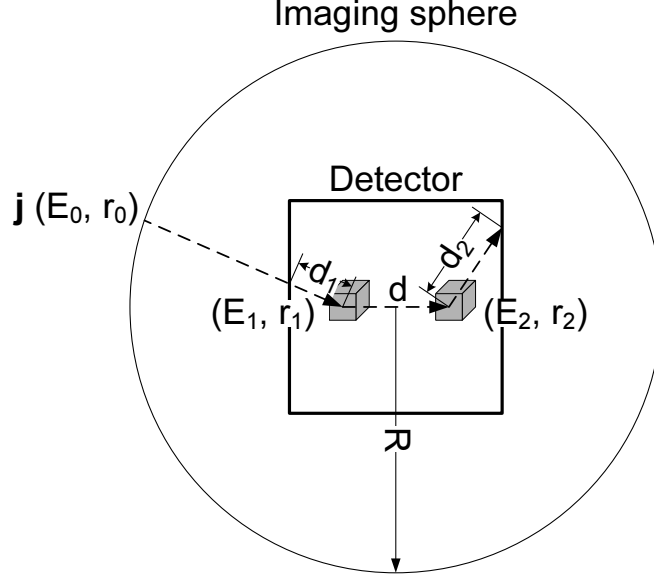


Figure 6.4: A photon from pixel \mathbf{j} creates a two-interaction event \mathbf{i} , which consists of energy depositions of E_1 and E_2 at positions \mathbf{r}_1 and \mathbf{r}_2 , respectively.

in which, θ_e is the scattering angle determined by energies ($\cos \theta_e = 1 + \frac{m_e c^2}{E_0} - \frac{m_e c^2}{E_0 - E_1}$), θ_r is the angle between $\tilde{\mathbf{\Omega}}_1$ and $\tilde{\mathbf{\Omega}}_2$, and $\delta(\theta_r - \theta_e)$ is the Dirac's delta function. Eq. 6.4 means that given the direction and the initial energy of the incident photon, and the energy deposited in the first scattering, the second interaction must occur on the surface of a cone with the half angle determined by Compton scattering kinematics (here, coherent scattering and Doppler broadening are neglected).

We introduce t as the distance that the scattered photon travels before the second interaction. If t is known, the second scattering must occur on a ring which is on the cone defined by Eq. 6.4. Since $\tilde{\mathbf{\Omega}}_1$ and $\tilde{\mathbf{\Omega}}_2$ is defined by $\tilde{\mathbf{r}}_0$, $\tilde{\mathbf{r}}_1$ and \mathbf{r}_2 , from Eq. 6.4 we have

$$f(\tilde{\mathbf{r}}_2 | E_0, \mathbf{r}_0, \tilde{E}_1, \tilde{\mathbf{r}}_1, t) = \frac{\delta(\theta_r - \theta_e) \delta(d - t)}{2\pi t^2 \sin \theta_e} \quad (6.5)$$

The probability density function for a photon with energy E_0 from \mathbf{r}_0 to interact at position $\tilde{\mathbf{r}}_1$ is

$$f(\tilde{\mathbf{r}}_1 | E_0, \mathbf{r}_0) = \frac{1}{4\pi R^2} \mu_{E_0} e^{-\mu_{E_0} d_1} \quad (6.6)$$

in which, $\frac{1}{4\pi R^2}$ is the solid angle and μ_E is the linear attenuation coefficient for gamma-rays at energy E .

The probability density function for a photon from (E_0, \mathbf{r}_0) to deposit \tilde{E}_1 in a Compton scattering given the condition that the photon interacts at position $\tilde{\mathbf{r}}_1$ is

$$\begin{aligned} f(\tilde{E}_1|E_0, \mathbf{r}_0, \tilde{\mathbf{r}}_1) &= \frac{1}{\sigma_t(E_0)} \frac{d\sigma_c(E_0)}{d\Omega} \bigg|_{\tilde{E}_1} \frac{d\Omega}{d\tilde{E}_1} \bigg|_{\tilde{E}_1} \\ &= \frac{N}{\mu_{E_0}} \frac{d\sigma_c(E_0)}{d\Omega} \bigg|_{\tilde{E}_1} \frac{d\Omega}{d\tilde{E}_1} \bigg|_{\tilde{E}_1} \end{aligned} \quad (6.7)$$

in which, $\sigma_t(E)$ is the total cross section at energy E , N is the number of nuclei per unit volume, and $\frac{d\sigma_c(E_0)}{d\Omega}$ is the differential scattering cross section defined by the Klein-Nishina formula.

The probability density function for the scattered photon to travel a distance of t before the second interaction is

$$f(t|E_0, \mathbf{r}_0, \tilde{E}_1, \tilde{\mathbf{r}}_1) = \mu_{E_0-E_1} e^{-\mu_{E_0-E_1} t} \quad (6.8)$$

From Eq. 6.6, 6.7, and 6.8, we can obtain

$$\begin{aligned} f(\tilde{E}_1, \tilde{\mathbf{r}}_1, t|E_0, \mathbf{r}_0) &= f(t|E_0, \mathbf{r}_0, \tilde{E}_1, \tilde{\mathbf{r}}_1) f(\tilde{E}_1|E_0, \mathbf{r}_0, \tilde{\mathbf{r}}_1) f(\tilde{\mathbf{r}}_1|E_0, \mathbf{r}_0) \\ &= \frac{1}{4\pi R^2} e^{-\mu_{E_0} d_1} N \frac{d\sigma_c(E_0)}{d\Omega} \bigg|_{\tilde{E}_1} \frac{d\Omega}{d\tilde{E}_1} \bigg|_{\tilde{E}_1} \mu_{E_0-\tilde{E}_1} e^{-\mu_{E_0-\tilde{E}_1} t} \end{aligned} \quad (6.9)$$

which is the probability density function that a photon with energy E_0 and from \mathbf{r}_0 creates the first scattering interaction of $(\tilde{E}_1, \tilde{\mathbf{r}}_1)$ and the scattered photon travels a distance of t before the second interaction.

From the Compton scattering kinematics, we obtain

$$d\Omega = 2\pi \sin \theta d\theta = \frac{2\pi m_e c^2}{(E_0 - E_1)^2} dE_1 \quad (6.10)$$

From Eq. 6.5, 6.9, and 6.10, we obtain

$$\begin{aligned}
f(\tilde{E}_1, \tilde{\mathbf{r}}_1, t, \tilde{\mathbf{r}}_2 | E_0, \mathbf{r}_0) &= f(\tilde{\mathbf{r}}_2 | E_0, \mathbf{r}_0, \tilde{E}_1, \tilde{\mathbf{r}}_1, t) f(\tilde{E}_1, \tilde{\mathbf{r}}_1, t | E_0, \mathbf{r}_0) \\
&= \frac{1}{4\pi R^2} e^{-\mu_{E_0} d_1} N \left. \frac{d\sigma_c(E_0)}{d\Omega} \right|_{\tilde{E}_1} \frac{2\pi m_e c^2}{(E_0 - \tilde{E}_1)^2} \\
&\quad \cdot \mu_{E_0 - \tilde{E}_1} e^{-\mu_{E_0 - \tilde{E}_1} t} \cdot \frac{\delta(\theta_r - \theta_e) \delta(t - d)}{2\pi t^2 \sin \theta_e}
\end{aligned} \tag{6.11}$$

Therefore, given that the initial photon has an energy of E_0 and is from \mathbf{r}_0 , the probability that the first interaction deposits \tilde{E}_1 at $\tilde{\mathbf{r}}_1$ and the second interaction happens at $\tilde{\mathbf{r}}_2$ is

$$\begin{aligned}
f(\tilde{E}_1, \tilde{\mathbf{r}}_1, \tilde{\mathbf{r}}_2 | E_0, \mathbf{r}_0) &= \int_0^\infty f(\tilde{E}_1, \tilde{\mathbf{r}}_1, t, \tilde{\mathbf{r}}_2 | E_0, \mathbf{r}_0) dt \\
&= \frac{1}{4\pi R^2} e^{-\mu_{E_0} d_1} N \left. \frac{d\sigma_c(E_0)}{d\Omega} \right|_{\tilde{E}_1} \frac{2\pi m_e c^2}{(E_0 - \tilde{E}_1)^2} \\
&\quad \cdot \mu_{E_0 - \tilde{E}_1} e^{-\mu_{E_0 - \tilde{E}_1} d} \cdot \frac{\delta(\theta_r - \theta_e)}{2\pi d^2 \sin \theta_e}
\end{aligned} \tag{6.12}$$

We will discuss two cases here depending on the type of the second interaction.

A. Photopeak events: The second interaction is a photo absorption, thus the full energy of the incident gamma-ray is deposited in the detector ($E_0 \approx E_1 + E_2$). $f(\tilde{\mathbf{i}}|\tilde{\mathbf{j}})$ becomes

$$\begin{aligned}
f(\tilde{\mathbf{i}}|\tilde{\mathbf{j}}) &= f(\tilde{E}_1, \tilde{\mathbf{r}}_1, \tilde{E}_2, \tilde{\mathbf{r}}_2 | E_0, \mathbf{r}_0) \\
&= f(\tilde{E}_1, \tilde{\mathbf{r}}_1, \tilde{\mathbf{r}}_2 | E_0, \mathbf{r}_0) f(\tilde{E}_2 | E_0, \mathbf{r}_0, \tilde{E}_1, \tilde{\mathbf{r}}_1, \tilde{\mathbf{r}}_2) \\
&= f(\tilde{E}_1, \tilde{\mathbf{r}}_1, \tilde{\mathbf{r}}_2 | E_0, \mathbf{r}_0) \frac{\sigma_p(\tilde{E}_2) \delta(E_0 - \tilde{E}_1 - \tilde{E}_2)}{\sigma_t(\tilde{E}_2)} \\
&= f(\tilde{E}_1, \tilde{\mathbf{r}}_1, \tilde{\mathbf{r}}_2 | E_0, \mathbf{r}_0) \frac{N \sigma_p(\tilde{E}_2) \delta(E_0 - \tilde{E}_1 - \tilde{E}_2)}{\mu_{E_0 - \tilde{E}_1}}
\end{aligned} \tag{6.13}$$

in which, $\sigma_p(\tilde{E}_2)$ is the photoelectric cross at energy \tilde{E}_2 .

B. Compton continuum: The second interaction is a Compton scattering and the scattered photon escapes the detector, thus only partial energy of the incident gamma-ray is deposited in the detector ($E_0 > E_1 + E_2$). $f(\tilde{\mathbf{i}}|\mathbf{j})$ becomes

$$\begin{aligned}
f(\tilde{\mathbf{i}}|\mathbf{j}) &= f(\tilde{E}_1, \tilde{\mathbf{r}}_1, \tilde{E}_2, \tilde{\mathbf{r}}_2|E_0, \mathbf{r}_0) \\
&= f(\tilde{E}_1, \tilde{\mathbf{r}}_1, \tilde{\mathbf{r}}_2|E_0, \mathbf{r}_0) f(\tilde{E}_2|E_0, \mathbf{r}_0, \tilde{E}_1, \tilde{\mathbf{r}}_1, \tilde{\mathbf{r}}_2) \\
&= f(\tilde{E}_1, \tilde{\mathbf{r}}_1, \tilde{\mathbf{r}}_2|E_0, \mathbf{r}_0) \frac{N}{\mu_{E_0-\tilde{E}_1}} \frac{d\sigma_c(E_0 - \tilde{E}_1)}{d\Omega} \bigg|_{\tilde{E}_2} \\
&\quad \cdot \frac{2\pi m_e c^2}{(E_0 - \tilde{E}_1 - \tilde{E}_2)^2} e^{-\mu_{E_0-\tilde{E}_1-\tilde{E}_2} d_2}
\end{aligned} \tag{6.14}$$

6.2.1.2 Uncertainties

Due to detector uncertainties, the observed event is different from the actual event. The probability for a photon emitted from pixel \mathbf{j} to create an observed event $\hat{\mathbf{i}}$ can be obtained by the integral of

$$f(\hat{\mathbf{i}}|\mathbf{j}) = \int f(\hat{\mathbf{i}}|\tilde{\mathbf{i}}) f(\tilde{\mathbf{i}}|\mathbf{j}) d\tilde{\mathbf{i}} \tag{6.15}$$

Specifically, 6.15 can be written as

$$f(\hat{E}_1, \hat{\mathbf{r}}_1, \hat{E}_2, \hat{\mathbf{r}}_2|E_0, \mathbf{r}_0) = \int f(\hat{E}_1, \hat{\mathbf{r}}_1, \hat{E}_2, \hat{\mathbf{r}}_2|\tilde{E}_1, \tilde{\mathbf{r}}_1, \tilde{E}_2, \tilde{\mathbf{r}}_2) f(\tilde{E}_1, \tilde{\mathbf{r}}_1, \tilde{E}_2, \tilde{\mathbf{r}}_2|E_0, \mathbf{r}_0) d\mathbf{V} \tag{6.16}$$

in which, $d\mathbf{V}$ is the integral volume in the measurement space defined by $\tilde{E}_1, \tilde{\mathbf{r}}_1, \tilde{E}_2$ and $\tilde{\mathbf{r}}_2$.

Suppose the measurements of the energy E and the position (x, y, z) all follow Gaussian distribution with uncertainties of σ_E , σ_x , σ_y , and σ_z , respectively. The probability density function of observing \hat{E} given the actual energy deposition of \tilde{E} is

$$f_E(\hat{E}|\tilde{E}) = \frac{1}{\sqrt{2\pi\sigma_E^2}} e^{-\frac{(\hat{E}-\tilde{E})^2}{2\sigma_E^2}} \tag{6.17}$$

Similarly, we have

$$f_x(\hat{x}|\tilde{x}) = \frac{1}{\sqrt{2\pi\sigma_x^2}} e^{-\frac{(\hat{x}-\tilde{x})^2}{2\sigma_x^2}} \quad (6.18)$$

$$f_y(\hat{y}|\tilde{y}) = \frac{1}{\sqrt{2\pi\sigma_y^2}} e^{-\frac{(\hat{y}-\tilde{y})^2}{2\sigma_y^2}} \quad (6.19)$$

$$f_z(\hat{z}|\tilde{z}) = \frac{1}{\sqrt{2\pi\sigma_z^2}} e^{-\frac{(\hat{z}-\tilde{z})^2}{2\sigma_z^2}} \quad (6.20)$$

As a result, $f(\hat{\mathbf{i}}|\tilde{\mathbf{i}}) = f(\hat{E}_1, \hat{\mathbf{r}}_1, \hat{E}_2, \hat{\mathbf{r}}_2|\tilde{E}_1, \tilde{\mathbf{r}}_1, \tilde{E}_2, \tilde{\mathbf{r}}_2)$ is a joint Gaussian distribution.

If the uncertainties in energy and position are smaller enough so that $f(\tilde{E}_1, \tilde{\mathbf{r}}_1, \tilde{E}_2, \tilde{\mathbf{r}}_2|E_0, \mathbf{r}_0)$ varies slowly around $(\hat{E}_1, \hat{\mathbf{r}}_1, \hat{E}_2, \hat{\mathbf{r}}_2)$, $f(\tilde{E}_1, \tilde{\mathbf{r}}_1, \tilde{E}_2, \tilde{\mathbf{r}}_2|E_0, \mathbf{r}_0)$ can be regarded as a constant and taken out of the integral in Eq. 6.16. Since, $\int f(\hat{E}_1, \hat{\mathbf{r}}_1, \hat{E}_2, \hat{\mathbf{r}}_2|\tilde{E}_1, \tilde{\mathbf{r}}_1, \tilde{E}_2, \tilde{\mathbf{r}}_2)d\mathbf{V} = 1$, we can approximate $f(\hat{E}_1, \hat{\mathbf{r}}_1, \hat{E}_2, \hat{\mathbf{r}}_2|E_0, \mathbf{r}_0)$ by replacing $(\tilde{E}_1, \tilde{\mathbf{r}}_1, \tilde{E}_2, \tilde{\mathbf{r}}_2)$ with $(\hat{E}_1, \hat{\mathbf{r}}_1, \hat{E}_2, \hat{\mathbf{r}}_2)$ in Eq. 6.13 and 6.14.

The above approximation is usually valid when $\tilde{E}_1 + \tilde{E}_2 < E_0$, which means the second interaction is a Compton scattering. However, if $\tilde{E}_1 + \tilde{E}_2 = E_0$, which means the second interaction is a photo-electric absorption, $(\tilde{E}_1, \tilde{\mathbf{r}}_1, \tilde{E}_2, \tilde{\mathbf{r}}_2|E_0, \mathbf{r}_0)$ has a term of a delta function and can not be regarded as a constant. In this case, the delta function should be integrated over \tilde{E}_1 and \tilde{E}_2 .

A. *Photopeak events:* $f(\hat{\mathbf{i}}|\mathbf{j})$ is obtained by

$$\begin{aligned} f(\hat{E}_1, \hat{\mathbf{r}}_1, \hat{E}_2, \hat{\mathbf{r}}_2|E_0, \mathbf{r}_0) &= f(\hat{E}_1, \hat{\mathbf{r}}_1, \hat{\mathbf{r}}_2|E_0, \mathbf{r}_0) \frac{N\sigma_p(\hat{E}_2)}{\mu_{E_0-\hat{E}_1}} \\ &\quad \cdot \iint \frac{d\tilde{E}_1 d\tilde{E}_2 \delta(E_0 - \tilde{E}_1 - \tilde{E}_2)}{2\pi\sigma_{E_1}\sigma_{E_2}} e^{-\frac{(\hat{E}_1-\tilde{E}_1)^2}{2\sigma_{E_1}^2} - \frac{(\hat{E}_2-\tilde{E}_2)^2}{2\sigma_{E_2}^2}} \\ &= f(\hat{E}_1, \hat{\mathbf{r}}_1, \hat{\mathbf{r}}_2|E_0, \mathbf{r}_0) \frac{N\sigma_p(\hat{E}_2)}{\mu_{E_0-\hat{E}_1}} \\ &\quad \cdot \int \frac{d\tilde{E}_1}{2\pi\sigma_{E_1}\sigma_{E_2}} e^{-\frac{(\hat{E}_1-\tilde{E}_1)^2}{2\sigma_{E_1}^2} - \frac{(E_0-\hat{E}_2-\tilde{E}_1)^2}{2\sigma_{E_2}^2}} \\ &= \frac{f(\hat{E}_1, \hat{\mathbf{r}}_1, \hat{\mathbf{r}}_2|E_0, \mathbf{r}_0) N\sigma_p(\hat{E}_2)}{\mu_{E_0-\hat{E}_1} \sqrt{2\pi(\sigma_{E_1}^2 + \sigma_{E_2}^2)}} e^{-\frac{(E_0-\hat{E}_1-\hat{E}_2)^2}{2(\sigma_{E_1}^2 + \sigma_{E_2}^2)}} \end{aligned} \quad (6.21)$$

B. Compton continuum: From Eq. 6.14, $f(\hat{\mathbf{i}}|\mathbf{j})$ is obtained by

$$f(\hat{E}_1, \hat{\mathbf{r}}_1, \hat{E}_2, \hat{\mathbf{r}}_2|E_0, \mathbf{r}_0) = f(\hat{E}_1, \hat{\mathbf{r}}_1, \hat{\mathbf{r}}_2|E_0, \mathbf{r}_0) \frac{N}{\mu_{E_0-\hat{E}_1}} \frac{d\sigma_c(E_0 - \hat{E}_1)}{d\Omega} \bigg|_{\hat{E}_2} \cdot \frac{2\pi m_e c^2}{(E_0 - \hat{E}_1 - \hat{E}_2)^2} e^{-\mu_{E_0-\hat{E}_1-\hat{E}_2} d_2} \quad (6.22)$$

In Eq. 6.21 and 6.22, $f(\hat{E}_1, \hat{\mathbf{r}}_1, \hat{\mathbf{r}}_2|E_0, \mathbf{r}_0)$ is the same as Eq. 6.12, except \tilde{E}_1 , $\tilde{\mathbf{r}}_1$, and $\tilde{\mathbf{r}}_2$ are replaced by \hat{E}_1 , $\hat{\mathbf{r}}_1$, and $\hat{\mathbf{r}}_2$.

6.2.1.3 Binning

The binning process is to integrate the probability density function over the bin volume, i.e.

$$t_{ij} = \int_{\Delta \mathbf{V}_i} f(\hat{\mathbf{i}}|\mathbf{j}) d\hat{\mathbf{i}} = \int_{\Delta \mathbf{V}_i} f(\hat{E}_1, \hat{\mathbf{r}}_1, \hat{E}_2, \hat{\mathbf{r}}_2|E_0, \mathbf{r}_0) d\hat{\mathbf{i}} \quad (6.23)$$

in which, $d\hat{\mathbf{i}} = d\hat{E}_1 d\hat{\mathbf{r}}_1 d\hat{E}_2 d\hat{\mathbf{r}}_2$.

If the bin volume is small enough such that all terms except the delta function in $f(\hat{E}_1, \hat{\mathbf{r}}_1, \hat{E}_2, \hat{\mathbf{r}}_2|E_0, \mathbf{r}_0)$ vary slowly within the bin volume, the integral can be approximated by moving those terms out of the integral.

A. Photopeak events: The system response function is

$$\begin{aligned} t_{ij} &= \int_{\Delta \mathbf{V}_i} f(\hat{E}_1, \hat{\mathbf{r}}_1, \hat{E}_2, \hat{\mathbf{r}}_2|E_0, \mathbf{r}_0) d\hat{\mathbf{i}} \\ &= \frac{1}{4\pi R^2} e^{-\mu_{E_0} d_1} N \frac{d\sigma_c(E_0)}{d\Omega} \bigg|_{E_1} \frac{2\pi m_e c^2}{(E_0 - E_1)^2} e^{-\mu_{E_0-E_1} d} \\ &\quad \cdot \frac{1}{2\pi d^2 \sin \theta_e} \frac{N\sigma_p(E_2)}{\sqrt{2\pi(\sigma_{E_1}^2 + \sigma_{E_2}^2)}} e^{-\frac{(E_0-E_1-E_2)^2}{2(\sigma_{E_1}^2 + \sigma_{E_2}^2)}} \cdot \int_{\Delta \mathbf{V}_i} \delta(\theta_r - \theta_e) d\hat{\mathbf{i}} \end{aligned} \quad (6.24)$$

B. Compton continuum: The system response function is

$$\begin{aligned}
t_{ij} &= \int_{\Delta \mathbf{V}_i} f(\hat{E}_1, \hat{\mathbf{r}}_1, \hat{E}_2, \hat{\mathbf{r}}_2 | E_0, \mathbf{r}_0) d\hat{\mathbf{i}} \\
&= \frac{1}{4\pi R^2} e^{-\mu_{E_0} d_1} N \left. \frac{d\sigma_c(E_0)}{d\Omega} \right|_{E_1} \frac{2\pi m_e c^2}{(E_0 - E_1)^2} e^{-\mu_{E_0-E_1} d} \frac{N}{2\pi d^2 \sin \theta_e} \\
&\quad \cdot \left. \frac{d\sigma_c(E_0 - E_1)}{d\Omega} \right|_{E_2} \frac{2\pi m_e c^2}{(E_0 - E_1 - E_2)^2} e^{-\mu_{E_0-E_1-E_2} d_2} \int_{\Delta \mathbf{V}_i} \delta(\theta_r - \theta_e) d\hat{\mathbf{i}}
\end{aligned} \tag{6.25}$$

In both cases, there is an integral of $\int_{\Delta \mathbf{V}_i} \delta(\theta_r - \theta_e) d\hat{\mathbf{i}}$ which needs to be solved. Considering that this integral depends on \mathbf{r}_0 , \mathbf{r}_1 , \mathbf{r}_2 , E_0 and E_1 , and the integral volume is a rectangular parallelepiped due to pixellation and digitization, it is formidable to obtain an analytical solution for this integral. Here, we make the following assumptions to ease the calculation.

1. \mathbf{r}_0 is on the back-projection cone defined by \mathbf{r}_1 , \mathbf{r}_2 , E_0 and E_1 . A Gaussian function with its standard deviation equal to the angular uncertainty will be used to approximate the system response for pixels not on the back-projection cone.
2. The integral volumes around \mathbf{r}_1 and \mathbf{r}_2 have the same volume, and are approximated by two spheres with equivalent radius of R_0 as illustrated in Fig. 6.5.
3. θ_e is constant in the integral region around E_1 .

Under the above assumptions, the integral of $\int_{\Delta \mathbf{V}_i} \delta(\theta_r - \theta_e) d\hat{\mathbf{i}}$ can be calculated by

$$\begin{aligned}
\int_{\Delta \mathbf{V}_i} \delta(\theta_r - \theta_e) d\hat{\mathbf{i}} &= \Delta E_1 \Delta E_2 \int_{\Delta \mathbf{V}_1} d\hat{\mathbf{r}}_1 \int_{\Delta \mathbf{V}_2} d\hat{\mathbf{r}}_2 \delta(\theta_r - \theta_e) \\
&= \Delta E_1 \Delta E_2 \int_{\Delta \mathbf{V}_1} d\hat{\mathbf{r}}_1 \int_{-R_0}^{R_0} dz \int_S ds \delta(\theta_r - \theta_e)
\end{aligned} \tag{6.26}$$

The integral region S consists of those points which satisfy $\theta_r = \theta_e$. Strictly speaking, S is not a plane. However, when $d \gg R_0$, S can be approximated by a

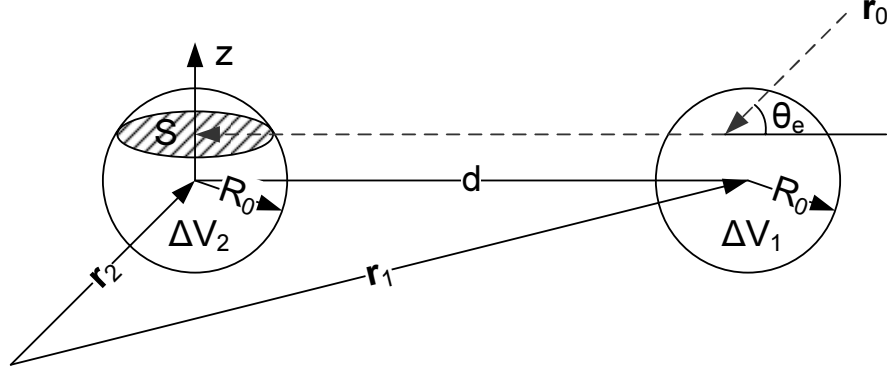


Figure 6.5: The bin volumes in the measurement space are approximated by two spheres when calculating the system response function.

plane. Also, when $d \gg R_0$, $dz = d \cdot d\theta_r$. As a result, we obtain

$$\begin{aligned}
 \int_{\Delta \mathbf{V}_i} \delta(\theta_r - \theta_e) d\hat{\mathbf{i}} &= \Delta E_1 \Delta E_2 d \int_{\Delta \mathbf{V}_1} S d\hat{\mathbf{r}}_1 \\
 &= \Delta E_1 \Delta E_2 d \int_0^\pi \pi (R_0 \sin \theta)^2 \pi (R_0 \sin \theta)^2 R_0 \sin \theta d\theta \\
 &= \frac{16}{15} \pi^2 R_0^5 d \Delta E_1 \Delta E_2
 \end{aligned} \tag{6.27}$$

6.2.1.4 Final result

For source pixel \mathbf{j} of which the gamma-ray initial position is on the back-projection cone defined by \mathbf{r}_1 , \mathbf{r}_2 , E_0 and E_1 , the system response function is

A. Photopeak events:

$$\begin{aligned}
 t_{ij} &= \frac{2R_0^5 \Delta E_1 \Delta E_2 N^2}{15R^2 d \sin \theta_e} e^{-\mu_{E_0} d_1} \left. \frac{d\sigma_c(E_0)}{d\Omega} \right|_{E_1} \frac{2\pi m_e c^2}{(E_0 - E_1)^2} \\
 &\quad \cdot e^{-\mu_{E_0 - E_1} d} \frac{\sigma_p(E_2)}{\sqrt{2\pi(\sigma_{E_1}^2 + \sigma_{E_2}^2)}} e^{-\frac{(E_0 - E_1 - E_2)^2}{2(\sigma_{E_1}^2 + \sigma_{E_2}^2)}}
 \end{aligned} \tag{6.28}$$

B. Compton continuum:

$$\begin{aligned}
 t_{ij} &= \frac{2R_0^5 \Delta E_1 \Delta E_2 N^2}{15R^2 d \sin \theta_e} e^{-\mu_{E_0} d_1} \left. \frac{d\sigma_c(E_0)}{d\Omega} \right|_{E_1} \frac{2\pi m_e c^2}{(E_0 - E_1)^2} e^{-\mu_{E_0 - E_1} d} \\
 &\quad \cdot \left. \frac{d\sigma_c(E_0 - E_1)}{d\Omega} \right|_{E_2} \frac{2\pi m_e c^2}{(E_0 - E_1 - E_2)^2} e^{-\mu_{E_0 - E_1 - E_2} d_2}
 \end{aligned} \tag{6.29}$$

For other source pixels not on the back-projection cone, their system responses are approximated by a Gaussian function of which the standard deviation equals the angular uncertainty, which is determined by the detector position uncertainties, Doppler broadening, and the energy uncertainties.

In Eq. 6.28 and 6.29, $e^{-\mu_{E_0} d_1}$ is the probability for the incident photon to reach the first interaction position, $\left. \frac{d\sigma_c(E_0)}{d\Omega} \right|_{E_1} \frac{2\pi m_e c^2}{(E_0 - E_1)^2}$ represents the probability for the incident photon to deposit E_1 in the scattering, $e^{-\mu_{E_0 - E_1} d}$ is the probability for the scattered photon to reach the second interaction position, $\sigma_p(E_2)$ represents the probability for the scattered photon to be photo-electric absorbed, $\left. \frac{d\sigma_c(E_0 - E_1)}{d\Omega} \right|_{E_2} \frac{2\pi m_e c^2}{(E_0 - E_1 - E_2)^2}$ represents the probability for the scattered photon to deposit E_2 in the second scattering, and $e^{-\mu_{E_0 - E_1 - E_2} d_2}$ is the probability for the escaping photon to leave the detector. The $\frac{1}{\sin \theta_e}$ term represents the probability that \mathbf{r}_2 is on the direction of the scattered photon. In the Compton continuum case, the lack of the energy Gaussian spread shown in the photopeak case is due to the facts that the system response function in the Compton continuum case is a slow-changing continuous function of the incident gamma-ray energy E_0 , and a Gaussian spread with a small uncertainty will not affect the system response function very much. This is the direct result of the approximation done in Eq. 6.22.

We notice that R_0 , ΔE_1 , ΔE_2 , N and R are all constants for a specific detector system, and d is a fixed value for a specific event. From Eq. 5.51, the iteration is not sensitive to the scaling factor in the system response function since t_{ij} appears on both the numerator and the denominator. Therefore, we can ignore those constants to simplify the system response function as

A. *Photopeak events:*

$$t_{ij} = \frac{1}{\sin \theta_e} e^{-\mu_{E_0} d_1} \left. \frac{d\sigma_c(E_0)}{d\Omega} \right|_{E_1} \frac{1}{(E_0 - E_1)^2} \cdot e^{-\mu_{E_0-E_1} d} \frac{\sigma_p(E_2)}{\sqrt{2\pi(\sigma_{E_1}^2 + \sigma_{E_2}^2)}} e^{-\frac{(E_0-E_1-E_2)^2}{2(\sigma_{E_1}^2 + \sigma_{E_2}^2)}} \quad (6.30)$$

B. *Compton continuum:*

$$t_{ij} = \frac{1}{\sin \theta_e} e^{-\mu_{E_0} d_1} \left. \frac{d\sigma_c(E_0)}{d\Omega} \right|_{E_1} \frac{1}{(E_0 - E_1)^2} e^{-\mu_{E_0-E_1} d} \cdot \left. \frac{d\sigma_c(E_0 - E_1)}{d\Omega} \right|_{E_2} \frac{2\pi m_e c^2}{(E_0 - E_1 - E_2)^2} e^{-\mu_{E_0-E_1-E_2} d_2} \quad (6.31)$$

6.2.1.5 Discussions on the system response function model

There are several details that need to be addressed:

A. *Total cross section* The total cross section may not include coherent scattering (Rayleigh scattering) cross section because the photon does not loss energy in coherent scattering process. Coherent scattering is usually unimportant in modeling gamma-ray transportation. However, when the gamma-ray energy is low (below a few hundred keV), the cross section and average deflection angle of coherent scattering become nontrivial, and coherent scattering should be taken into account in a complete model.

B. *Sequence ambiguity* In 3-D position-sensitive CdZnTe detectors, sequence reconstruction algorithms are applied to determine the order of the measured interactions. However, these algorithms can only estimate which sequence has the highest probability, but can not eliminate the sequence ambiguity. An accurate system response model should consider all the possible sequences. Particularly, for a two-interaction

event, each interaction can be the first interaction. Therefore, there are two back-projection rings at each energy in our model of the system response function.

C. Conventional Compton cameras For conventional Compton cameras with known incident gamma-ray energy E_0 and known interaction sequence, the system response function can be greatly simplified due to the insensitivity of the MLEM algorithm to the scaling factors in the system response function. In this case, Eq. 6.30 and Eq. 6.31 can both be reduced to $e^{-\sigma_t(E_0)d_1}$, which is the only term in the system response function related to pixel \mathbf{j} . If the size of the detector system is small, this term can be further reduced. Therefore, the system response function for conventional Compton cameras is constant on the back-projection cone with a spread defined by the angular uncertainty.

D. Variation in the binning volume size The anode surface of the 3-D position-sensitive CdZnTe detector is pixellized into an 11×11 array. The effective volume of the peripheral pixels is slightly larger than that of the central pixels. This variation in the binning volume size will affect the integral of $\int_{\Delta V_i} \delta(\theta_r - \theta_e) d\hat{\mathbf{i}}$ in the derivation of the system response function. However, this integral does not depend on the energy or direction of the incident gamma-ray, thus is a constant to all pixels. Again, due to the insensitivity of the MLEM algorithm to the scaling factors in t_{ij} , this integral can be ignored. Therefore, the variation in the binning volume size will not affect the deconvolution process.

E. Escaping distance d_2 If the incident photon is scattered twice in the detector, and the final scattered photon escapes the detector, the escaping photon can be on any direction on a cone, as shown in Fig. 6.6. Since the measurement does not

provide any information about the escaping direction, an average escaping distance is calculated by sampling 8 directions uniformly distributed on the cone.

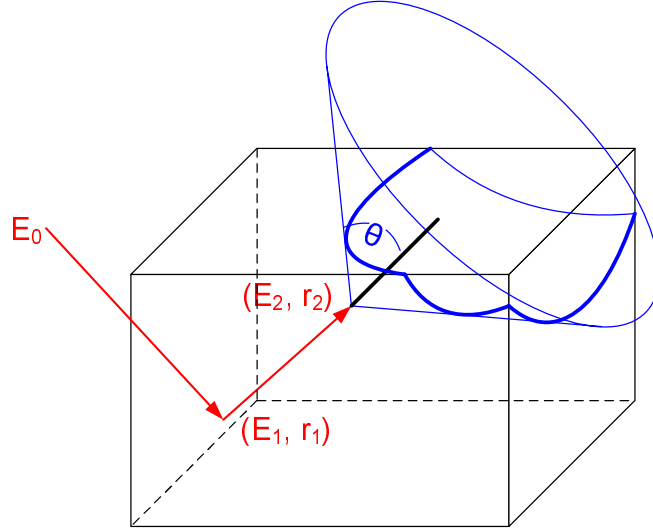


Figure 6.6: The escaping photon can be on any direction on the escaping cone. The half angle of the escaping cone can be calculated from E_0 , E_1 , and E_2 .

6.2.2 Factors not Included in the Model

There are several factors that can affect the system response function. The current ASIC (VAS3.1/TAT3) developed for 3-D position-sensitive CdZnTe detectors have an anode triggering threshold of about 30 keV and a dynamic range of about 1.6 MeV [29, 45]. New ASIC under development can have dynamic range up to 3 MeV. Any energy deposition below the triggering threshold or above the dynamic range will not be measured correctly, and have an impact on the system response function. For example, theoretically, it is possible for a photon with energy greater than $E_1 + E_2$ to scatter several times before depositing E_1 and E_2 in the detector, with the deposited energies lower than the triggering threshold in each scattering. However, this possibility is considered very low and will have little influence on the deconvolution results.

The effect of multiple interactions under the same pixel occurs in about one fifth

of the measured events. Since the measured depth is the interaction depth of the energy deposition which is the closest to the anode side, there is an asymmetry in the system response function between the cathode side and the anode side. Currently, no efficient method has been developed to account for the pixel sharing effect. However, as shown in Fig. 2.15, the separation distance between the two interactions under the same pixel is very small, and it is very likely that the two interactions are consecutive. Therefore, the impact on the image reconstruction is small by regarding the two interactions as a single interaction.

The charge sharing events are another factor that can affect the system response function. A K X-ray escaping to a neighboring pixel can also cause a two-pixel event in which the incident photon only deposit a single interaction in the detector. Currently, there is no efficient way to distinguish those events from the true two-interaction events. Since the charge sharing events have two energy depositions in neighboring pixels, and the depth difference between the two energy depositions is small (Fig. 2.14(a)), the charge sharing events can be eliminated by excluding the neighboring two-pixel events with depth difference less than 2 mm, at the expense of losing some true two interaction events.

6.2.3 Verification of the System Response Function

Eq. 6.30 and Eq. 6.31 give a theoretical model of the system response function for two-pixel events in 3-D position-sensitive CdZnTe detectors. This model can be examined by comparing with simulation results. However, the absolute value of a single element in the system response function is extremely small, which means the probability for a photon to create a specific two-pixel event is very low. Therefore, it requires huge amount of simulations to create enough counts in a specific bin. Here, we use an alternative way to compare the system response function model with

simulations by generating an energy spectrum from the system response function, and comparing it with the simulated spectrum. The energy spectrum can be generated by summing the system response function over all measurement output \mathbf{i} with certain total energy deposition, i.e.

$$P(E|\mathbf{j}) = \sum_{\substack{\mathbf{i} \\ E_{1i}+E_{2i}=E}} t_{ij} \quad (6.32)$$

The source is placed at the side of the detector. Two incident gamma-ray energies at 356 keV and 662 keV were compared. In the simulation, only two interaction events were counted. The ASIC triggering threshold, the pixel sharing effect, and the charge sharing effect were not included. The calculated spectra from the system response function and the simulated spectra are shown in Fig. 6.7

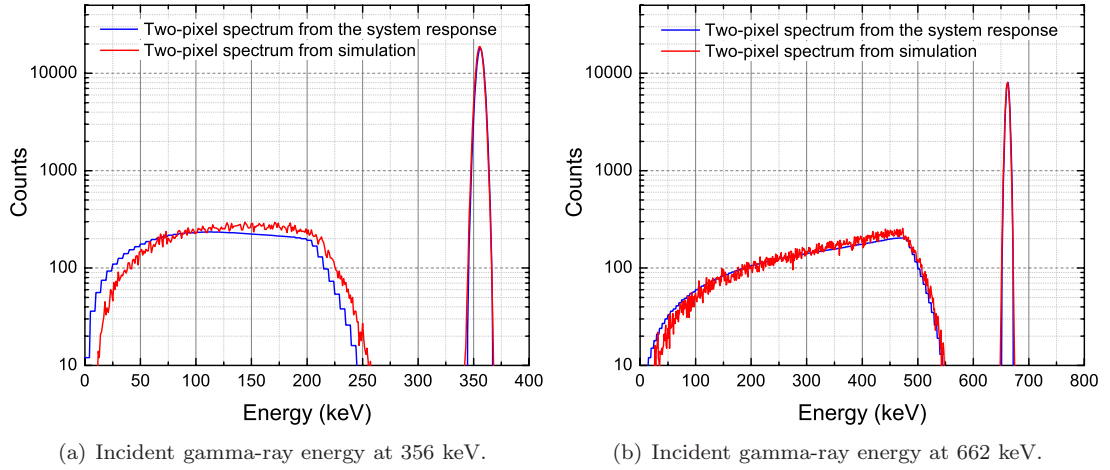


Figure 6.7: Comparison of the spectra generated from the system response function and the spectra from Geant4 simulations.

As we can see, the energy spectra generated by the system response function agree with the Geant4 simulations at both energies, which indicates that the proposed system response function models the 3-D CdZnTe detector very well. The slight difference in the Compton continuum could be caused by the error in the average escaping distance d_2 .

6.2.4 Calculation of the Sensitivity Image

The sensitivity image s_j in the list-mode MLEM algorithm of Eq. 5.60 needs to be precalculated. Theoretically, s_j can be calculated by summing the system response function over all possible measurement outputs, i.e.

$$s_j = \sum_i t_{ij} \quad (6.33)$$

However, the approach of Eq. 6.33 is impractical for 3-D CdZnTe detectors because the number of possible measurement outputs is huge. Therefore, the sensitivity image is usually obtained by Monte Carlo simulations. This method becomes very computational expensive if the number of image pixels is large, such as in 3-D imaging or energy-imaging integrated reconstruction. Carson proposed a method of summing over a down-sampled data set instead of summing over all possible measurement outputs [84]. Qi developed a sampling strategy to reduce the error in the calculated sensitivity image [85]. However, those sampling methods depends on the accuracy of the system response function. In this work, we propose another approach by summing over the measurement outputs obtained in Monte Carlo simulations. This method can produce the sensitivity image that is not affected by the scaling errors in the system response function.

In the proposed method, a Geant4 simulation with sources uniformly distributed in all imaging pixel \mathbf{j} was first performed to provide a data set. When we use the simulated data set to do the reconstruction using the MLEM algorithm, if the iteration begins with the true source distribution, the next MLEM iteration will converge toward the MLEM solution. Since the MLEM solution is an asymptotic unbiased estimator, we can assume that with enough statistics, the MLEM solution and the true source distribution are very close to each other. Therefore, $\hat{f}^{k+1} \approx \hat{f}^k$.

As a result, s_j can be estimated by

$$\hat{s}_j = \sum_{i=1}^N \frac{t_{ij}}{\sum_{j'} t_{ij'} \hat{f}_{j'}^0} \quad (6.34)$$

The list-mode data is obtained from the Monte Carlo simulation with a preset source distribution \hat{f}^0 , which is uniform in this work. As can be seen from Eq. 6.34, our estimator of the sensitivity image is not sensitive to the scaling error in the system response function.

Suppose there are M gamma rays emitted from the uniform source in the simulation. Those gamma rays are tagged by $m = 1, 2, \dots, M$. The source has J pixels with the same area, so the M gamma rays are uniformly distributed within these J pixels. The m^{th} gamma-ray is from pixel j_m , and $j_m \in \{1, 2, 3, \dots, J\}$. The average number of gamma rays emitted from pixel j is

$$E[n_j] = \frac{M}{J} \quad (6.35)$$

which will be our start image \hat{f}^0 .

For each gamma-ray j_m , it can either pass through the detector or be recorded. The number of possible measurement outputs is I , and we denote the measurement result of m^{th} gamma-ray is i_m , and $i_m \in \{1, 2, \dots, I\}$. If m^{th} gamma-ray is not detected, we let $i_m = 0$.

The proposed estimator of the sensitivity image s_j is written as

$$\hat{s}_j = \sum_{\substack{m=1 \\ i_m \neq 0}}^M \frac{t_{i_m j}}{\sum_{j'=1}^J t_{i_m j'} E[n_{j'}]} = \frac{J}{M} \sum_{\substack{m=1 \\ i_m \neq 0}}^M \frac{t_{i_m j}}{\sum_{j'=1}^J t_{i_m j'}} \quad (6.36)$$

The expectation value of this estimator is

$$E[\hat{s}_j] = \frac{J}{M} E \left[\sum_{\substack{m=1 \\ i_m \neq 0}}^M \frac{t_{i_m j}}{\sum_{j'=1}^J t_{i_m j'}} \right] \quad (6.37)$$

Since the M gamma rays are independent of each other, Eq. 6.37 becomes

$$E [\hat{s}_j] = J \cdot E \left[\frac{t_{ij}}{\sum_{j'=1}^J t_{ij'}} \right] \quad (6.38)$$

The physical meaning of the above equation is that the expectation of the sensitivity image s_j does not depend on how many gamma rays are simulated. Instead, the expected value of s_j can be calculated from a single simulation.

The probability for a gamma-ray to be recorded as event i is

$$\begin{aligned} & Pr [\text{a gamma-ray is recorded as event } i] \\ &= \sum_{j=1}^J Pr [\text{a gamma-ray is recorded as event } i \mid i \text{ from pixel } j] Pr [i \text{ from pixel } j] \\ &= \frac{1}{J} \sum_{j=1}^J t_{ij} \end{aligned} \quad (6.39)$$

Therefore, we have

$$\begin{aligned} E \left[\frac{t_{ij}}{\sum_{j'=1}^J t_{ij'}} \right] &= \sum_{i=1}^I \frac{t_{ij}}{\sum_{j'=1}^J t_{ij'}} Pr [\text{a gamma-ray is recorded as event } i] \\ &= \sum_{i=1}^I \frac{t_{ij}}{\sum_{j'=1}^J t_{ij'}} \frac{1}{J} \sum_{j'=1}^J t_{ij'} \\ &= \frac{1}{J} \sum_{i=1}^I t_{ij} \\ &= \frac{s_j}{J} \end{aligned}$$

As a result, the expectation value of the proposed sensitivity image estimator becomes

$$E [\hat{s}_j] = J \cdot E \left[\frac{t_{ij}}{\sum_{k=1}^J t_{ik}} \right] = s_j \quad (6.40)$$

which means \hat{s}_j is an unbiased estimator of the sensitivity image s_j .

The proposed estimator of the sensitivity image depends on the assumption of $\hat{f}^1 \approx \hat{f}^0$ given \hat{f}^0 is the true source distribution. It is well known that the MLEM convergence solution is quite noisy and might be different from the true source

distribution[86, 87]. However, since the MLEM convergence speed is also low, it is still reasonable to assume that the first iteration is very close to the true source distribution.

The calculated sensitivity image by Eq. 6.34 is compared with the Geant4 simulation result as shown in Fig. 6.8. Because it is impossible to run simulations for every image pixel \mathbf{j} , we only compare the sensitivity images as a function of the incident gamma-ray energy. In the Geant4 simulations, the incident gamma-rays are uniformly distributed from all directions, and the estimated sensitivity image is summed over all incident directions. It can be seen that the estimated sensitivity image agrees with the simulation result very well.

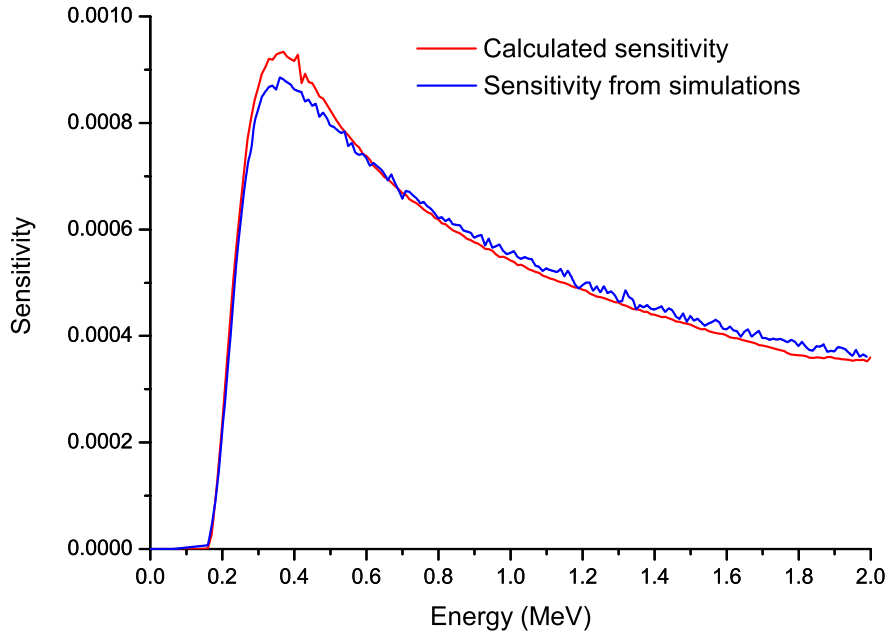


Figure 6.8: Comparison of the calculated sensitivity and the sensitivity from Geant4 simulations as a function of the incident gamma-ray energy.

6.3 Performance

The energy-imaging integrated deconvolution algorithm was applied to both simulated data and measured data. In the system response function model of Eq. 6.30,

the energy resolution was modeled by Eq. 4.5. The spatial imaging space of the 4π sphere was divided into 64×64 pixels, and the energy space was divided into 500 bins from 0 to 2 MeV. The MLEM algorithm was stopped after 24 iterations.

6.3.1 Deconvolution Using Simulation Data

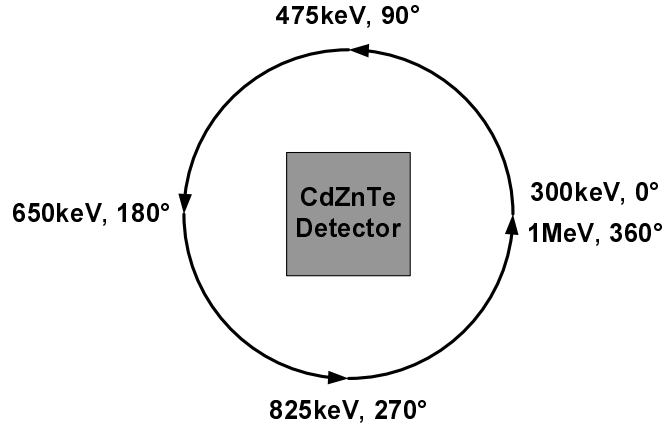


Figure 6.9: Source distribution in the Geant4 simulation. The source is uniformly distributed around the side of the detector. The source energy increases from 300 keV to 1 MeV linearly as a function of the rotational angle from 0° to 360° .

Ideally, the energy-imaging integrated deconvolution algorithm estimates the true incident gamma-ray intensity. A Geant4 simulation was performed with a point source uniformly distributed from 300 keV to 1 MeV. The source rotates around the detector at the side as the energy increases linearly as a function of the rotational angle, as shown in Fig. 6.9. By deconvolving the simulation data, we can examine both the energy and spatial uniformity of the deconvolution method. About 226k two-pixel events were used in the deconvolution.

Fig. 6.10 shows the simulated two-pixel spectrum and the deconvolved spectrum. The simulated raw spectrum does not imply that the source is uniform between 300 keV and 1 MeV. This is because the detection efficiencies at different energies are different, and the low-energy part of the spectrum is contaminated by the Compton background from the high-energy gamma-rays. The simulated raw spectrum also

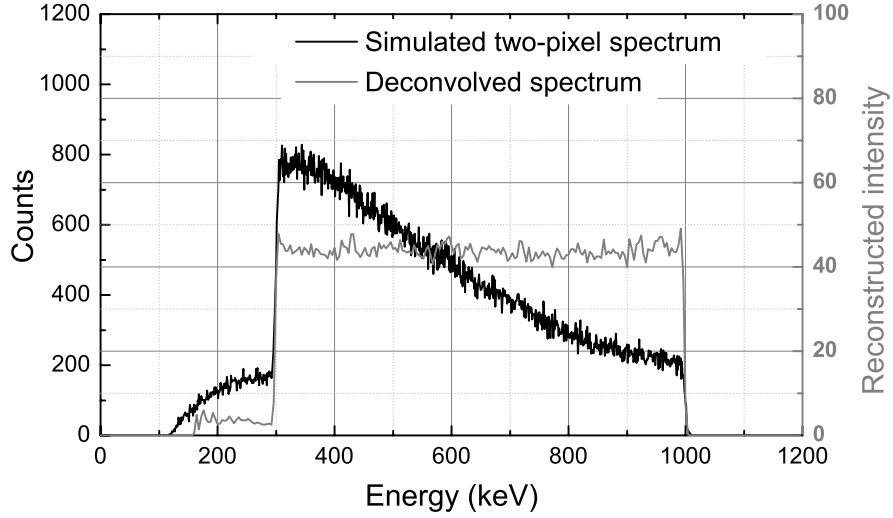


Figure 6.10: Simulated two-pixel spectrum and deconvolved spectrum.

shows a Compton background below 300 keV although there is no incident gamma-ray with energy below 300 keV. However, the deconvolved spectrum represents the true energy distribution of the incident gamma-rays, which is uniform from 300 keV to 1 MeV. Fig. 6.11 shows the deconvolved energy spectra at different gamma-ray incident directions. The deconvolved spectrum in Fig. 6.10 still shows some background below 300 keV. This is because the MLEM algorithm tends to amplify the statistical noise if the detection efficiency is low. As shown in Fig. 6.8, the two-pixel event detection efficiency decreases quickly for gamma-rays with energy lower than 300 keV, and this low efficiency introduces the background below 300 keV. In Fig. 6.11 we can see that those Compton background around 200 keV are distributed across all angles and can be ignored at each direction. Although the detection sensitivity varies according to the incident directions because of the asymmetry of the geometry of the detector, the deconvolved spectra correctly show that the source is spatially uniform.

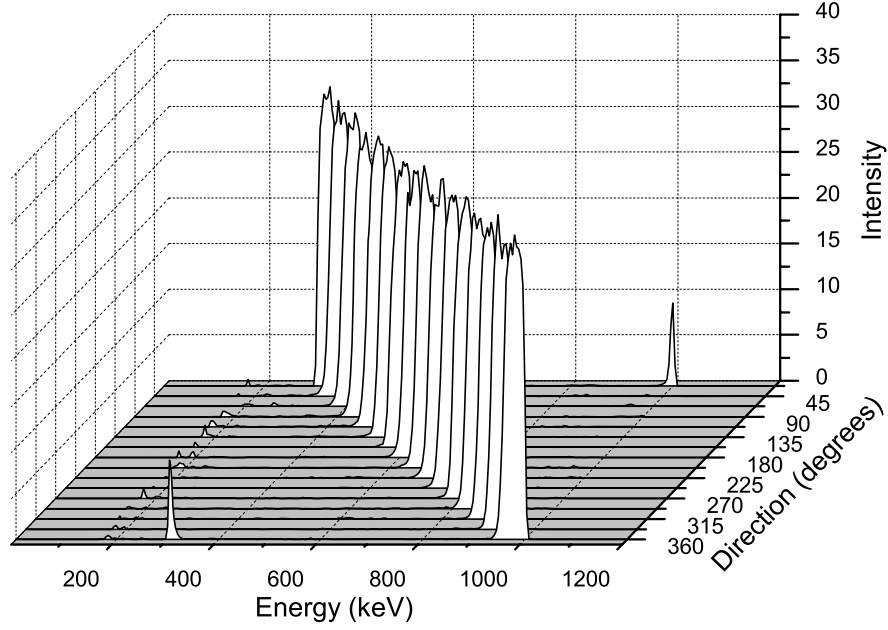


Figure 6.11: Deconvolved spectra at different directions. The spectra show that the source is not only uniformly distributed in energy from 300 keV to 1 MeV, but it is also uniformly distributed across spatial directions.

6.3.2 Deconvolution Using Experiment Data

The energy-imaging integrated deconvolution algorithm was applied to the measured data using three point sources as described by Fig. 6.2. The three point sources were Ba-133, Na-22, and Cs-137, respectively. About 41k two-pixel events were used in the deconvolution. After the deconvolution, the three sources were well resolved. Fig. 6.12 respectively shows the images at the three characteristic energies of the gamma-ray sources, which are 356 keV, 511 keV and 662 keV. It clearly shows the locations of the three sources. If we look at the directions of the three sources, as shown in Fig. 6.13, the deconvolved spectra only show the true incident gamma-ray spectra which are free of Compton continuum.

Although the spectral deconvolution method can remove the Compton continuum which is caused by the scatters within the detector, it is not able to remove the background in which the scatters occur outside the detector. In those events,

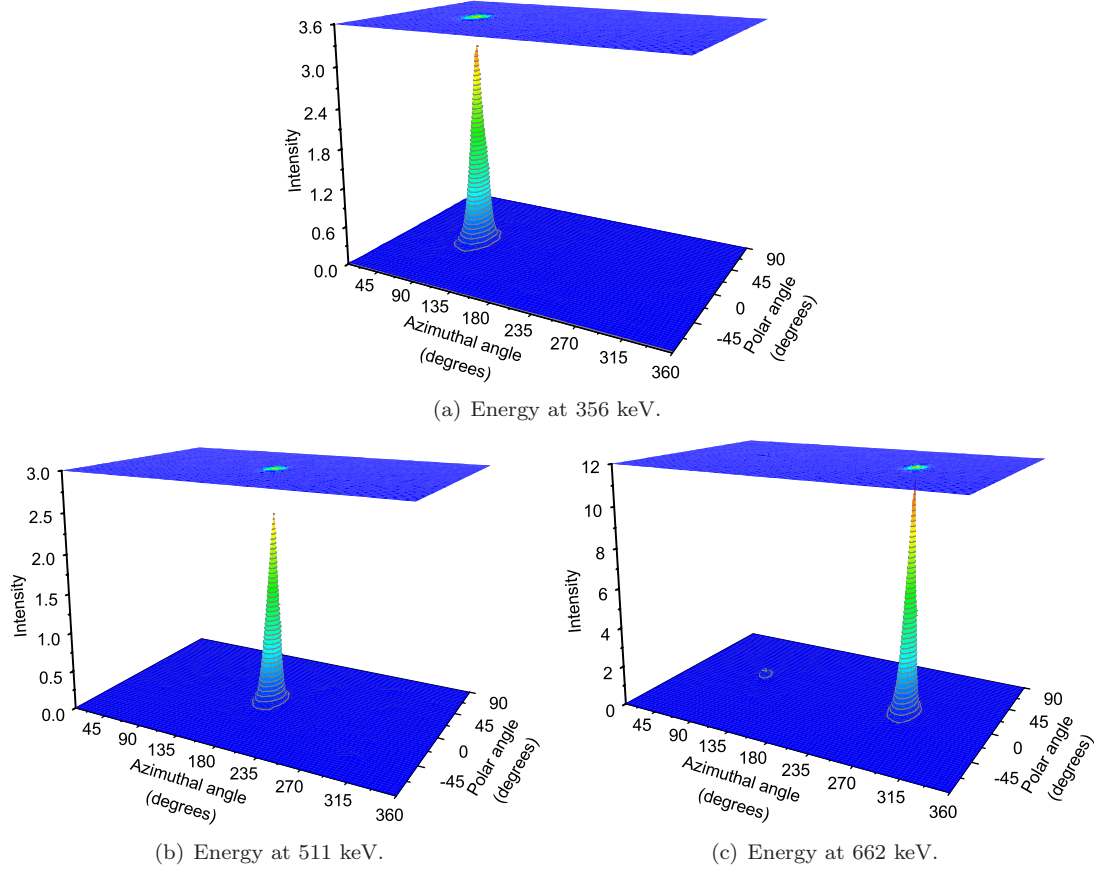


Figure 6.12: The deconvolved images at the photopeak energies of the three sources. The 4π imaging space is projected onto a plane defined by the azimuthal and the polar angles of the sphere.

the gamma-ray from the source is first scattered by the materials surrounding the detector, the scattered photon enters the detector and is recorded. The detector can not distinguish those scattered photons from the un-scattered photons. Since the deconvolved spectra represent the intensity of the incident gamma-rays, which include the scattered photons from the surrounding materials, we expect to see a distribution of those scattered photons, especially a backscatter peak. Fig. 6.13 also shows the deconvolved spectrum from all directions, in which a continuous background is present. However, because the scattered photons are spatially distributed, their distribution is not prominent in the localized spectrum shown in Fig. 6.13.

In order to verify that the deconvolved spectrum represents the true intensity of

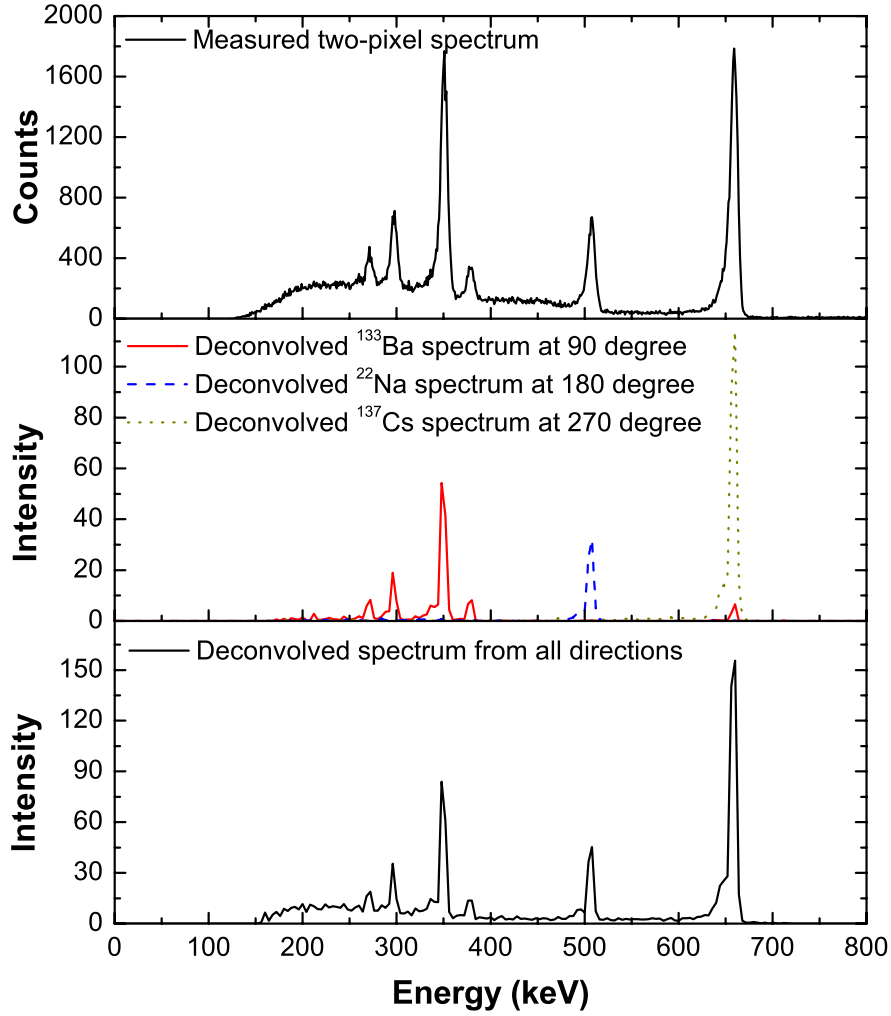


Figure 6.13: The upper figure is the measured two-pixel spectrum. The middle figure respectively shows the deconvolved spectra at the three source directions. The lower figure is the deconvolved spectrum from all directions.

the incident gamma-rays, the relative intensities of the four ^{133}Ba gamma lines to the 356 keV line are listed in Table 6.1. The relative intensities from the raw spectrum are calculated with background subtracted. As we can see, the deconvolved spectrum represents the true relative intensities much better than the measured raw spectrum.

6.3.3 Comparison with Conventional Compton Imaging and Energy Spectral Deconvolution

The conventional Compton imaging was performed by setting an energy window around the full energy peak. By doing so, the true full energy deposition events as

Table 6.1: Relative intensities of the four ^{133}Ba lines to the 356 keV line

	276 keV	302 keV	356 keV	384 keV
Absolute intensity	11.55%	29.54%	100%	14.41%
Measured spectrum	8.87%	26.70%	100%	11.39%
Deconvolved spectrum	12.30%	29.65%	100%	14.27%

well as the Compton backgrounds from the higher energy gamma-rays are selected. The Compton backgrounds are usually spatially distributed, and have little effect on the angular resolution of the reconstructed image of a point source. However, as shown in Fig. 6.14(a), the Compton backgrounds do introduce noises in the reconstructed image because they are from random directions. Fig. 6.14(b) shows the energy-imaging integrated deconvolved image summed in the same energy window. Since the Compton backgrounds are correctly recognized as from higher energy gamma-rays, they introduce less noises comparing with the conventional Compton imaging by setting an energy window.

The energy-imaging integrated algorithm uses all measured events and puts the Compton backgrounds into the right energy bin. As a result, the image obtained at a full energy peak is from both the true full energy deposition events and the Compton backgrounds. The Compton backgrounds usually have larger angular uncertainties than the full energy events. Therefore, the imaging spatial resolution of the new imaging-energy integrated deconvolution algorithm is not superior comparing with the conventional Compton imaging by setting an full energy window. Fig. 6.15 shows the images obtained by the two methods for the 511 keV gamma-rays from the ^{22}Na source. It can be seen that the energy-imaging integrated deconvolved image has a spatial resolution slightly worse than the reconstructed image by setting a full energy window.

Energy spectral deconvolution was also applied to the measurement. Because they

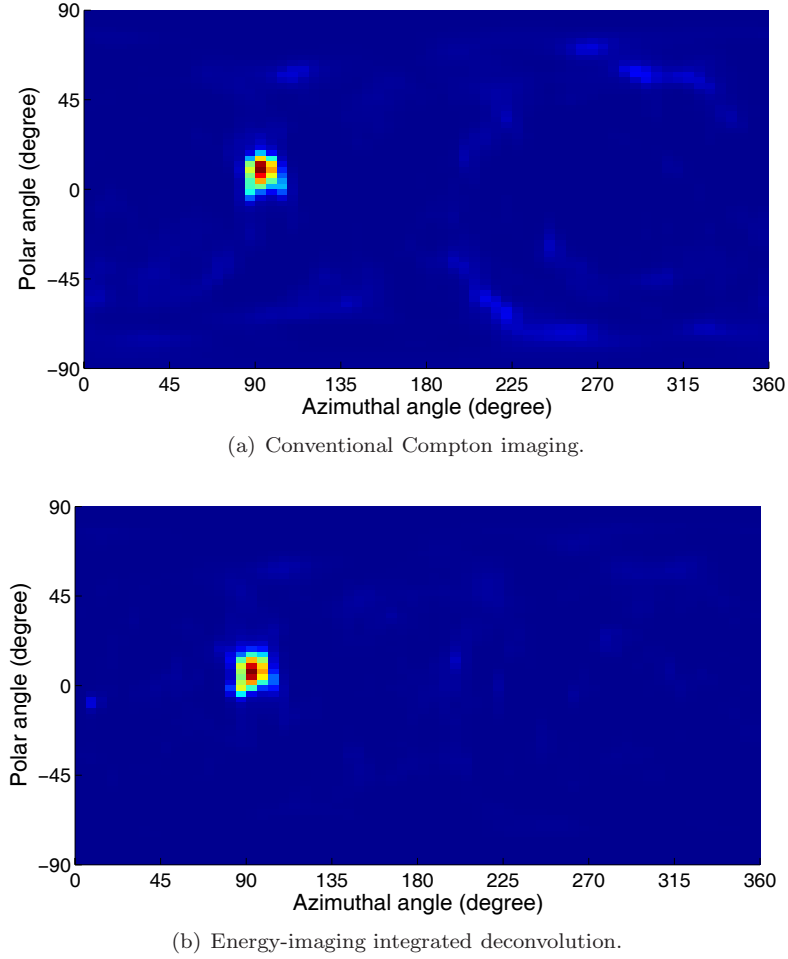


Figure 6.14: Images of the 384 keV line from the ^{133}Ba source. (a) Reconstructed image by setting an energy window from 370 keV to 390 keV. (b) Energy-imaging integrated deconvolved image summed from 370 keV to 390 keV.

do not require the directional information of the incident gamma-rays, single-pixel events can also be used in the deconvolution. Fig. 6.3 shows the measured raw spectrum of all events and the deconvolved spectrum. In the spectrum, it can be seen that the 80 keV photopeak from the ^{133}Ba source is also present. In the current system, the energy threshold for individual pixels is about 60 keV. Therefore, for two-pixel events, the minimal detectable energy is 120 keV, which is the reason why the 80 keV peak is absent in the spectra in Fig. 6.13. Comparing the energy-imaging integrated deconvolved spectrum in Fig. 6.13 with the spectral deconvolved spectrum

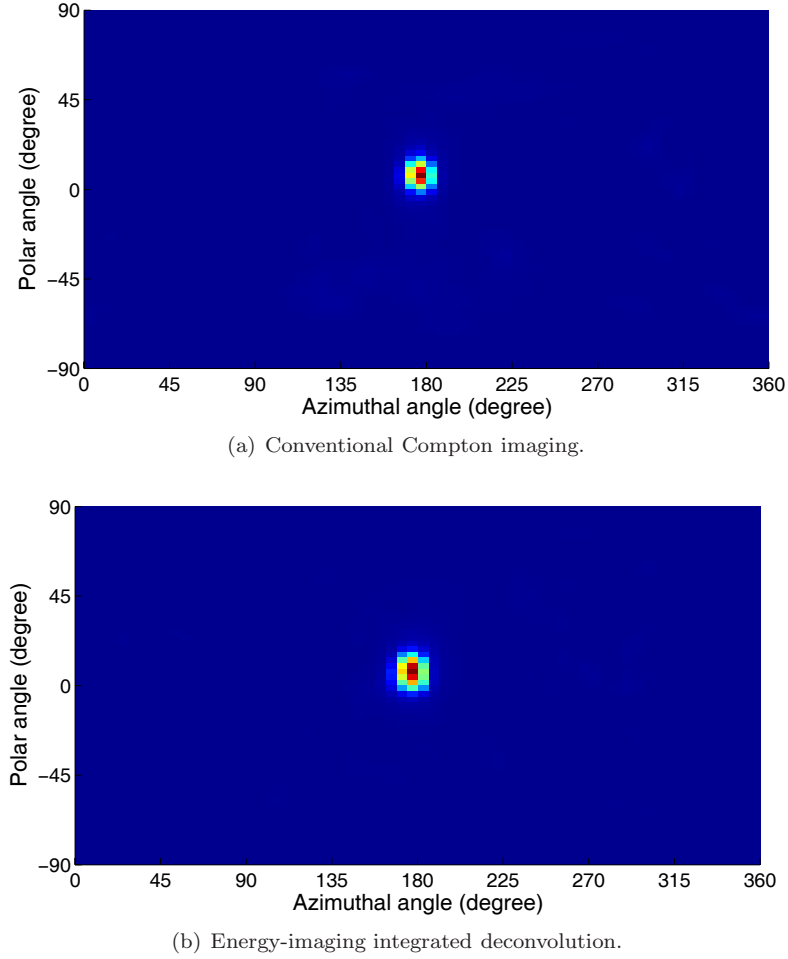


Figure 6.15: Images of the 511 keV line from the ^{22}Na source. (a) Reconstructed image by setting an energy window from 490 keV to 520 keV. (b) Energy-imaging integrated deconvolved image summed from 490 keV to 520 keV.

in Fig. 6.3, we can see both spectra show backgrounds due to photons that were scattered outside the detector. Because both methods did not model the surrounding materials, the scattering background can not be removed by either method. Although by carefully modeling the surrounding materials, the energy spectral deconvolution method can provide a more detailed system response function, and can remove the scattering background, this practice is not possible for hand-held detectors of which the operation environment changes frequently. In the energy-imaging integrated deconvolved spectrum, because the scattering background is spatially distributed,

the scattering background is not present in the localized spectra at the true source directions. As a result, the signal-to-noise ratio can be improved at the true source directions.

CHAPTER VII

POLARIZATION MEASUREMENT

The polarimetry of X-ray or gamma-ray sources is an important tool to study the origins of X-ray or gamma-ray production in high-energy astrophysics. With the recent report of linear polarization in the prompt gamma-ray emission from gamma-ray burst GRB021206[88], which provided detailed information of the origin of gamma-ray bursts (GRB), interest has risen in polarimetry in high-energy astrophysics[89]. The current X-ray or gamma-ray detectors employed for astrophysics missions are not optimized for polarization study, and polarimetry ability is one of the most interested characteristics for next-generation X-ray and gamma-ray telescopes. In 1996, S.E. Inderhees and R.A. Kroeger successfully demonstrated the detection of the polarization of gamma rays using position-sensitive germanium strip detectors (GSD) [90, 91]. However, the cooling requirement of germanium detectors is a serious limitation for satellite missions. In this study, we show that room temperature 3-D position-sensitive CdZnTe detectors, which are designed for gamma-ray spectroscopy and imaging[92, 29, 30], can be an excellent candidate to do polarization measurements[93].

7.1 The Klein-Nishina Formula for Polarized Incident Gamma-Rays

All of the three most important interactions of X-rays and gamma-rays with matter are polarization dependent. The direction of the products from these interactions, i.e., photoelectrons in photoelectric absorption, scattered photons in Compton scattering, and electron-positron pairs in pair production, all retain signatures of the polarization information of the incident photons. This angular dependence on the polarization direction of the incident photons can be the basis of the polarization measurement in different energy ranges. For soft gamma-rays with energy between 300 keV and 10 MeV, Compton scattering is the dominant process and is the most-used interaction in current polarization measurements.

According to the Klein-Nishina formula, the Compton scattering cross section per electron for a linearly-polarized gamma-ray is[62]

$$d\sigma = \frac{r_0^2}{4} d\Omega \frac{k_1^2}{k_0^2} \left[\frac{k_0}{k_1} + \frac{k_1}{k_0} - 2 + 4 \cos^2 \Theta \right] \quad (7.1)$$

in which $d\sigma$ is the differential cross section, $d\Omega = \sin \theta d\theta d\eta$ is the differential solid angle around Ω , θ is the scattering angle, the azimuthal angle η is the angle between the electric vector of the incident gamma-ray and the scattering plane, r_0 is the classical electron radius, k_1 and k_0 are the respective momenta of the scattered and initial gamma rays, and Θ is the angle between the electric vectors of the incident gamma-ray and scattered photon ε_0 and ε' , respectively. The angles and directions involved in the scattering are shown in Fig. 7.1

From Fig. 7.1, we can easily obtain the geometrical relationships of

$$\cos \Theta = \cos \beta \sin \xi \quad (7.2)$$

and

$$\cos \xi = \sin \theta \cos \eta \quad (7.3)$$

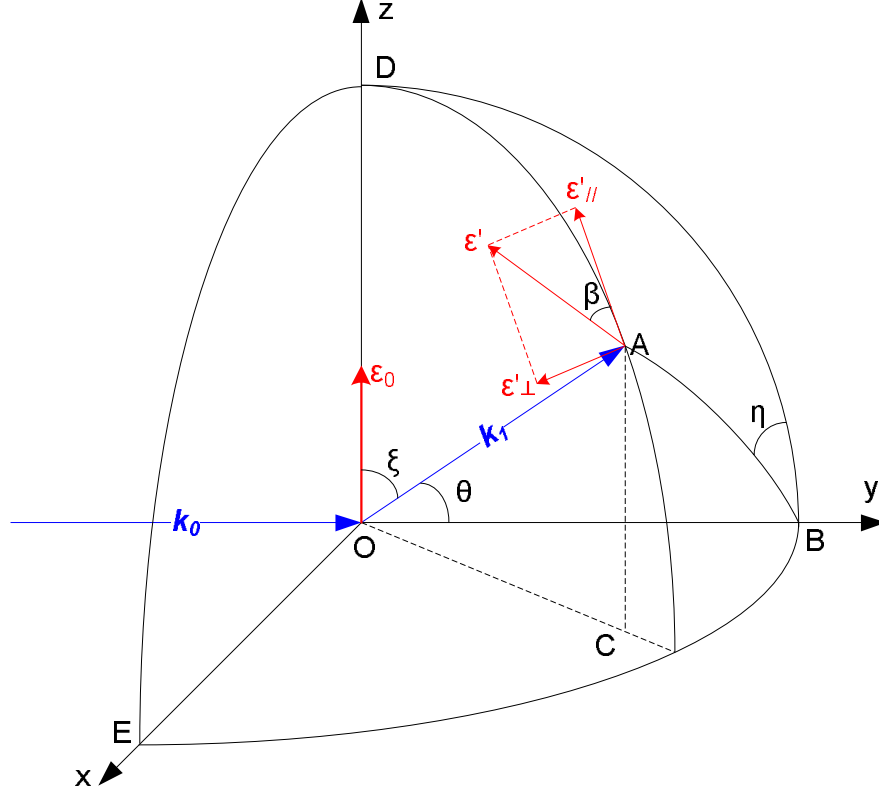


Figure 7.1: Compton scattering of a polarized photon at position O. ε_0 and ε' are the electric vectors of incident and scattered photons, respectively. θ is the scattering angle, ξ is the angle between the scattering direction and the electric vector of the incident photon, η is the angle between the electric vector of the incident photon and the scattering plane, and β is the angle between the electric vector of the scattered photon and OCAD plane.

Eq. 7.1 becomes

$$d\sigma = \frac{r_0^2}{4} d\Omega \frac{k_1^2}{k_0^2} \left[\frac{k_0}{k_1} + \frac{k_1}{k_0} - 2 + 4 \cos^2 \beta (1 - \sin^2 \theta \cos^2 \eta) \right] \quad (7.4)$$

The total differential cross section for a scattering in which the photon is scattered at a specific θ and η can be calculated by summing over all directions of polarization of the scattered photon. In particular, it can be calculated by summing the differential cross sections when $\beta = 0$ and $\beta = \pi/2$. As a result, we have

$$\begin{aligned} d\sigma &= d\sigma_{\parallel} + d\sigma_{\perp} \\ &= \frac{r_0^2}{2} d\Omega \frac{k_1^2}{k_0^2} \left[\frac{k_0}{k_1} + \frac{k_1}{k_0} - 2 \sin^2 \theta \cos^2 \eta \right] \end{aligned} \quad (7.5)$$

Eq. 7.5 is the differential Compton scattering cross section for polarized gamma-

rays. For unpolarized gamma-rays, the incident gamma-ray can be resolved into two orthogonally polarized components with the same intensity. The directions of the two components can be chosen to be perpendicular and parallel to the scattering plane ($\eta = \pi/2$ and $\eta = 0$), respectively. As a result, the differential cross section for unpolarized gamma-rays is the sum of these two components, i.e.

$$\begin{aligned} d\sigma &= \frac{1}{2}d\sigma_{\eta=\pi/2} + \frac{1}{2}d\sigma_{\eta=0} \\ &= \frac{r_0^2}{2}d\Omega \frac{k_1^2}{k_0^2} \left[\frac{k_0}{k_1} + \frac{k_1}{k_0} - \sin^2 \theta \right] \end{aligned} \quad (7.6)$$

which is the Klein-Nishina formula for unpolarized incident gamma-rays (Eq. 5.16).

7.2 Polarimetry Using Compton Scattering

From the differential cross section of Eq. 7.5 for polarized incident gamma-rays, it can be seen that for any specific scattering angle θ , the scattering probability is maximized when $\eta = \pi/2$, which means that the scattered photon prefers to be ejected at directions perpendicular to the polarization plane of the incident photon. By measuring the azimuthal angular distribution of the scattered photons, the polarization information of the incident photons can be deduced.

To quantify the polarization information, the modulation ratio is defined as

$$R(\varphi) = \frac{n(\varphi) - n(\varphi + \pi/2)}{n(\varphi) + n(\varphi + \pi/2)} \quad (7.7)$$

where φ is an arbitrary angle in a plane perpendicular to the incident photon direction, and $n(\varphi)$ is the measured number of events in $d\varphi$ about that angle.

Suppose the polarization direction of the incident gamma rays is at φ_0 , then

$\eta = \varphi - \varphi_0$. The modulation ratio becomes

$$\begin{aligned}
 R(\varphi) &= \frac{n(\varphi) - n(\varphi + \pi/2)}{n(\varphi) + n(\varphi + \pi/2)} \\
 &= \frac{d\sigma|_{\eta=\varphi-\varphi_0} - d\sigma|_{\eta=\varphi+\pi/2-\varphi_0}}{d\sigma|_{\eta=\varphi-\varphi_0} + d\sigma|_{\eta=\varphi+\pi/2-\varphi_0}} \\
 &= \frac{-\sin^2 \theta \cos(2\varphi - 2\varphi_0)}{\frac{k_0}{k_1} + \frac{k_1}{k_0} - \sin^2 \theta} \tag{7.8}
 \end{aligned}$$

in which $d\sigma|_{\eta}$ is the differential Compton scattering cross section at η . As we can see, at each scattering angle θ , the modulation ratio is a sinusoid function of $\cos(2\varphi - 2\varphi_0)$, which has a period of π . The amplitude of the modulation ratio versus the scattering angle at different the incident gamma-ray energies is shown in Fig. 7.2. Since the phase of the modulation ratio is independent of θ , the average modulation ratio over all scattering angles is still a function of $\cos(2\varphi - 2\varphi_0)$. The modulation ratio is maximized when φ is perpendicular to the polarization plane of the incident photon ($\varphi = \varphi_0 + \pi/2$), and is minimized when φ is along the polarization plane ($\varphi = \varphi_0$). Therefore, the polarization direction and degree can be deduced from the measured phase and amplitude of the modulation ratio, respectively.

7.3 Experiment Setup

Natural gamma-rays emitted from decaying isotopes are unpolarized. To obtain a polarized gamma-ray source, 662 keV photons from a ^{137}Cs source were scattered 90° by a $25.4 \text{ mm} \times 25.4 \text{ mm}$ BaF_2 scintillator before entering the 3-D CdZnTe detector. The scintillator and the CdZnTe detector were operated in coincidence to suppress the background. The 90° -scattered photons irradiated the CdZnTe detector from the cathode side. Those scattered photons were 58% polarized. In the actual experiment configuration shown in Fig. 7.3, due to the finite size of the scintillator, the photons entering the CdZnTe detector were not exactly 90° scattered. Therefore,

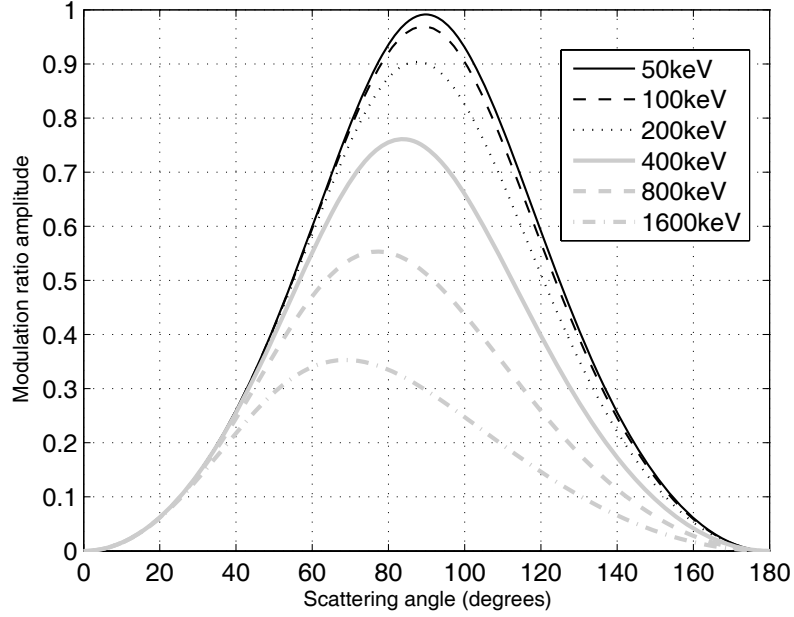


Figure 7.2: The change of the modulation ratio amplitude according to different incident gamma-ray energies and scattering angles. For a fixed incident gamma-ray energy, the modulation ratio amplitude is maximized when the scattering angle is slightly less than 90° .

the polarization degree of the incident photons was slightly less than 58%, which is one of the reasons causing the deficiency of the simulated modulation ratio when compared with the theoretical value (Fig. 7.4). When changing the position of the ^{137}Cs source, the polarization direction of the scattered photons will change accordingly. This will be reflected by the phase change of the measured modulation ratio.

7.4 Theoretical Prediction of the Modulation Ratio Amplitude

For an unpolarized 662 keV gamma-ray from the Cs-137 source, the direction of its electric vector is uniformly distributed in 2π . As a result, the azimuthal angle η is uniformly distributed. Therefore, to calculate the polarization status of the 90° -scattered photon, η should be integrated over 2π . When the scattering angle θ

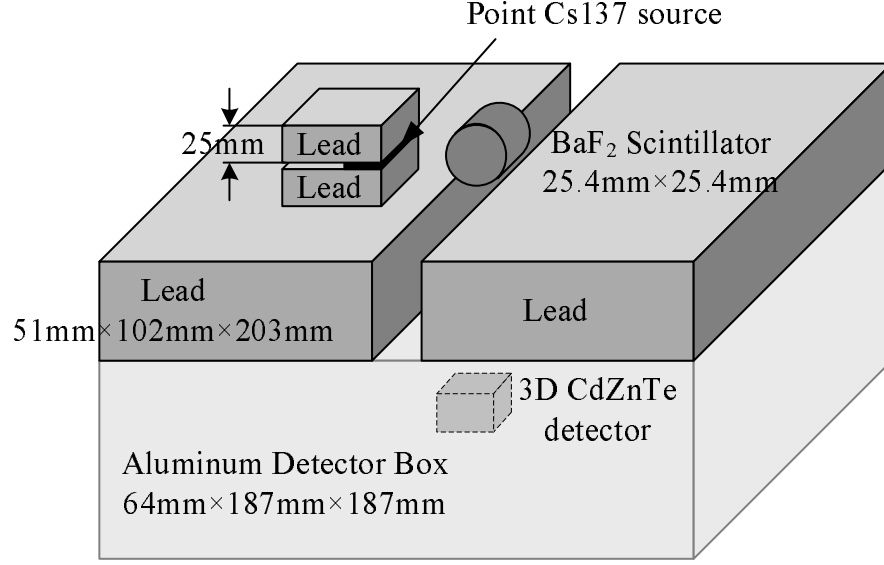


Figure 7.3: Experimental setup. The Cs-137 source was scattered by the BaF₂ scintillator before entering the CdZnTe detector. The scintillator was operated in coincidence with the CdZnTe detector to suppress the background. The CdZnTe detector is enclosed in the detector box and placed underneath the scintillator.

equals $\pi/2$, we have

$$\begin{aligned}\epsilon_{\parallel}^2 &= \left. \frac{d\sigma_{\parallel}}{d\theta} \right|_{\theta=\pi/2} = \frac{r_0^2}{4} \int_0^{2\pi} d\eta \frac{k_1^2}{k_0^2} \left[\frac{k_0}{k_1} + \frac{k_1}{k_0} - 2 + 4(1 - \cos^2 \eta) \right] \\ &= \frac{r_0^2}{4} \cdot \frac{2\pi k_1^2}{k_0^2} \left[\frac{k_0}{k_1} + \frac{k_1}{k_0} \right]\end{aligned}\quad (7.9)$$

and

$$\begin{aligned}\epsilon_{\perp}^2 &= \left. \frac{d\sigma_{\perp}}{d\theta} \right|_{\theta=\pi/2} = \frac{r_0^2}{4} \int_0^{2\pi} d\eta \frac{k_1^2}{k_0^2} \left[\frac{k_0}{k_1} + \frac{k_1}{k_0} - 2 \right] \\ &= \frac{r_0^2}{4} \cdot \frac{2\pi k_1^2}{k_0^2} \left[\frac{k_0}{k_1} + \frac{k_1}{k_0} - 2 \right]\end{aligned}\quad (7.10)$$

Eq. 7.9 and Eq. 7.10 are obtained from Eq. 7.4 with $\beta = 0^\circ$ for σ_{\parallel} and $\beta = 90^\circ$ for σ_{\perp} . The ratio of k_1 and k_0 can be calculated from the Compton scattering equation, and is presented by

$$k_1 = \frac{k_0}{1 + \alpha(1 - \cos \theta)} \quad (7.11)$$

in which, $\alpha = h\nu_0/m_e c^2$ and $h\nu_0 = 662$ keV.

The polarization degree of the 90°-scattered photons is

$$\frac{\epsilon_{\parallel}^2 - \epsilon_{\perp}^2}{\epsilon_{\parallel}^2 + \epsilon_{\perp}^2} = \frac{2}{\frac{k_0}{k_1} + \frac{k_1}{k_0} + \frac{k_0}{k_1} + \frac{k_1}{k_0} - 2} = 0.577 \quad (7.12)$$

We first calculate the modulation ratio of linearly polarized photons at 288 keV, which is the scattered photon energy at 90° from the 662 keV gamma-rays. The modulation ratio of the actual 90°-scattered photons can be obtained by multiplying the modulation ratio of linearly polarized 288 keV photons by the actual polarization degree of the incident gamma rays.

The differential scattering cross section of a linearly polarized 288 keV photon is represented by Eq. 7.5. When we integrate over the scattering angle θ in Eq. 7.5, we can get the differential cross section of a linearly polarized photon to be scattered into different azimuthal angles, i.e.

$$d\sigma(\eta) = \frac{r_0^2}{4} d\eta \int_0^\pi \sin \theta d\theta \frac{k_1^2}{k_0^2} \left[\frac{k_0}{k_1} + \frac{k_1}{k_0} - 2 \sin^2 \theta \cos^2 \eta \right] \quad (7.13)$$

in which k_1/k_0 can be calculated by Eq. 7.11 with $h\nu_0 = 288$ keV, which is the energy of the 90°-scattered photon from a 662 keV gamma-ray.

The modulation ratio of linearly polarized 288 keV photons calculated from Eq. 7.13 is 0.412.

As a result, the theoretical modulation ratio expected in our experiment is: $0.412 \times 0.577 = 0.238$.

7.5 Simulations

Theoretical calculation gives the amplitude of the modulation ratio to be 0.238 if Compton scatterings at all scattering angles are recorded (see Appendix). From Eq. 7.8 and Fig. 7.2, the modulation ratio is a function of the scattering angle θ . In the actual detector system, the detection efficiency will vary at different scattering

angles, therefore the measured amplitude of the modulation ratio depends on the geometry of the detector. However, in this experiment, due to the low incidental gamma-ray energy, the detection efficiency at different scattering angles will be very close to 100%, except those scattering events with very large or small scattering angles (those events will deposit two interactions under the same pixel and will not be recorded as two pixel events by the detector system). Therefore, the measured modulation ratio should be still close to the theoretical value. In addition, since the detector is pixellated, the measured count rate at a specific scattering direction inside the CdZnTe detector depends on the solid angles subtended by pairs of pixel anodes along that scattering direction, which will contribute to the decrease of the amplitude of the modulation ratio. Simulations were run using the Geant Monte Carlo package to account for the effect of the detector geometry. As we can see in Fig. 7.4, the simulated amplitude of the modulation ratio is slightly less than the theoretical calculation.

Simulations were also run to study the efficiency of the 3-D CdZnTe detector as a polarimeter. In the simulation, the detector was irradiated by a beam of linearly polarized photons from the cathode side. For comparison, a Ge detector with the same geometry was also simulated. The polarimeter efficiency was calculated using only non-neighboring two-pixel events. For incident gamma rays with energy greater than 200 keV, the results in Fig. 7.5 show that CdZnTe detector has higher efficiency although the Compton scattering cross sections of CdZnTe and germanium are very close to each other. The advantage of CdZnTe is more significant if only photo peak events are selected for polarization measurement. This is because that CdZnTe has more stopping power for the scattered photon due to higher photoelectric cross section.

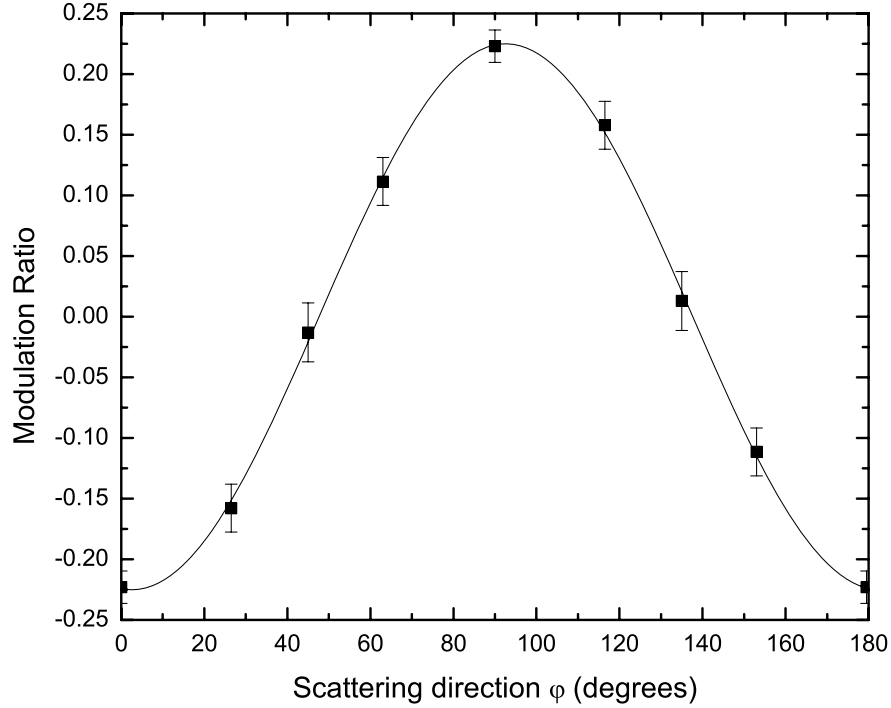


Figure 7.4: The modulation ratio from simulation. The amplitude of the modulation ratio is 0.225, which is slightly less than the theoretical value of 0.24. The difference is caused by the finite size of the scintillator, the different detection efficiencies for different scattering angles and the finite pixel size.

7.6 Results

As shown in Fig. 7.6, the Cs-137 source was placed at four different locations, which are at 0° , 30° , 60° and 90° with respect to the direction of the gap between the two lead shielding blocks. Events recorded by two neighboring anode pixels on the 3-D pixellated CdZnTe detector were excluded to eliminate the influence of charge sharing events. The activity of the ^{137}Cs source was $20\mu\text{Ci}$. The count rate of two-pixel events in the detector was very low due to the low coincidence rate between the BaF_2 scintillator and the 3-D CdZnTe detector. After one week of data acquisition, only about 3500 useful events were recorded. The observed events were mostly recorded by two anode pixels that are separated only by one pixel in between, thus the recorded scattering direction can only have some discrete values, such as 0° ,

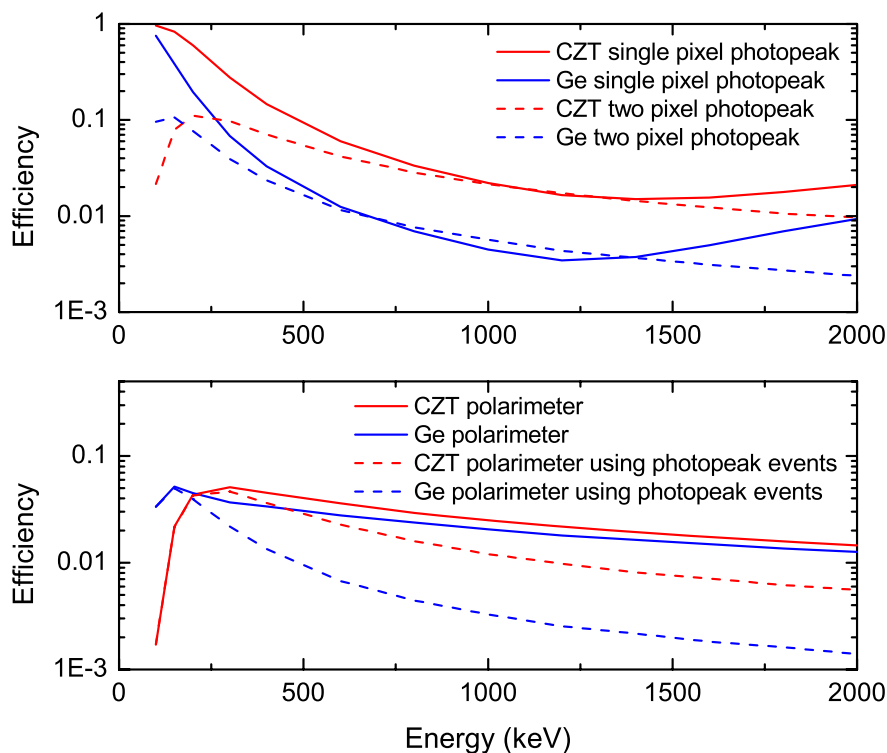


Figure 7.5: Simulated spectrometer and polarimeter efficiencies for CdZnTe and Ge detectors. The events useful for polarimeter are defined as non-neighboring two-pixel events.

27°, 45°, 63° and 90°.

The polarization direction of the scattered photons will change according to the position of the ^{137}Cs source. This will be reflected by the phase change of the measured modulation ratio as shown in Fig. 7.7. The modulation ratio should have a period of 180°, and any two points with 90° phase difference should differ only in the sign.

The low count rate has contributed to the large experimental uncertainties. However, the phase change in the modulation ratio is still evident. The amplitude of the modulation ratio is between 0.19 and 0.25, which is close to the theoretical value of 0.238 and the simulated result of 0.225. The statistical uncertainties of the measurement should be improved if more counts are collected.

The source location can be reconstructed by Compton imaging. Since the incident

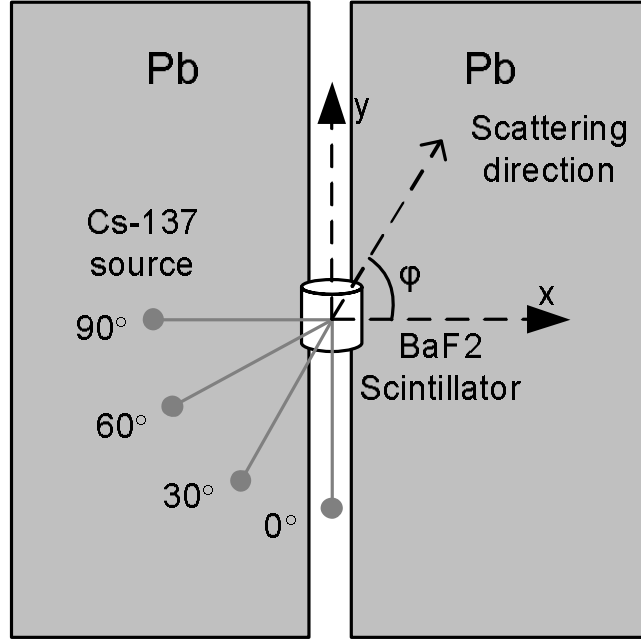


Figure 7.6: Top view of the measurement setup. The source was placed at four different locations to produce scattered gamma rays with different polarization directions, which can be deduced by measuring the distribution of the scattering direction in the CdZnTe detector. The CdZnTe detector was placed underneath the BaF₂ scintillator and is not displayed in this figure.

direction of gamma rays from a source can be identified, the polarization measurement can be performed on any source in space. Fig. 7.8 shows the reconstructed image using one of the measured data sets with the list-mode MLEM algorithm. The image shows the source correctly at the location of the BaF₂ scintillator.

In our data processing program, events with all scattering angles were taken into account to provide better statistics. From Fig.7.2, we can see that the modulation ratio is maximized at scattering angle slightly less than 90°. If a specific range of scattering angles around 90° is selected to enhance the polarization effect, higher modulation ratio can be obtained. The selection of scattering angles can be done by selecting scatter energies, positions of interactions, or even both to provide better accuracy by rejecting those non-Compton scattering events, such as events with multiple interactions under one pixel anode or events produced by pair production at

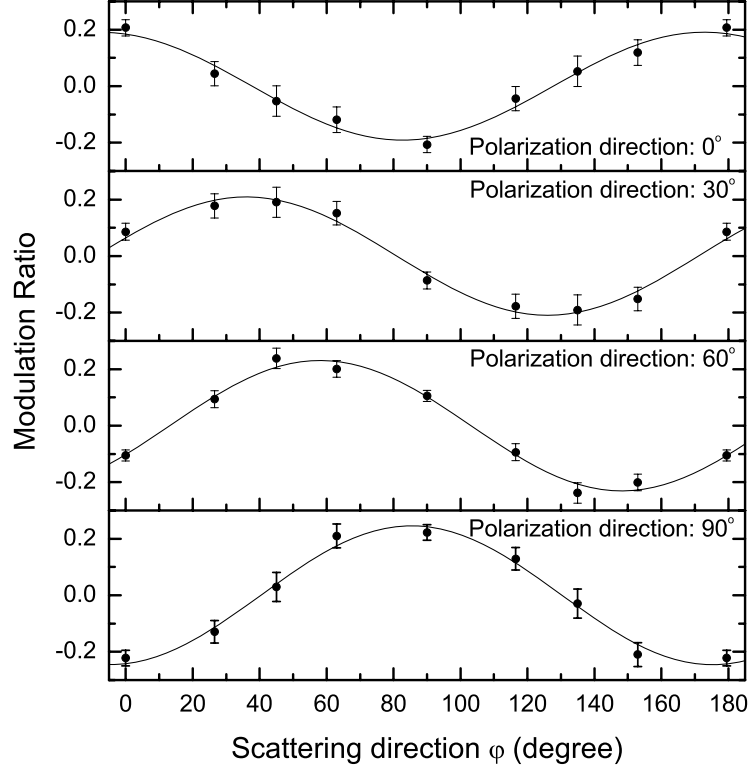


Figure 7.7: Modulation ratio measured for 288 keV gamma rays with 60% polarization degree. The phase shift of the modulation ratio reflects the measured polarization direction, and the amplitude of the modulation ratio is proportional to the polarization degree.

higher energies. However, to get the scattering angle from the interaction positions, the direction of the incident gamma-ray source must be known a priori. This will be possible from the imaging capability of the 3-D CdZnTe detector.

In principle, three (or more) pixel events are also useful in polarization measurement and they provide more information. However, for energy as low as 300 keV, three or more pixel events in CdZnTe are rare. At higher energies, three or more pixel events should contribute more to the polarization measurement.

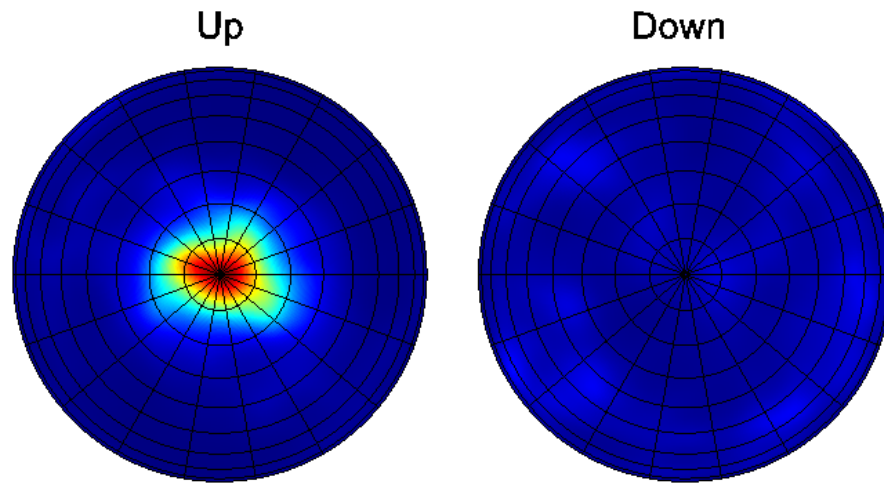


Figure 7.8: Reconstructed image of the 90° -scattered photons after 24 iterations with the list-mode MLEM algorithm. The image shows the up and down hemispheres of the 4π imaging space. Since the scintillator has a finite size, the reconstructed image is a distributed phantom.

CHAPTER VIII

Summary and Future Work

8.1 Summary

It has been demonstrated that three-dimensional position-sensitive room temperature CdZnTe detectors are precise and versatile gamma-ray measurement devices. Besides the excellent energy resolution, information about the incident gamma-ray position and polarization can be measured without the use of mechanical collimators or coded apertures common to other gamma-ray imaging devices. Furthermore, the detector has a full 4π field of view. The dimensions of the detector studied in this work are $15\text{ mm} \times 15\text{ mm} \times 10\text{ mm}$. The position resolution is approximately $1.3\text{ mm} \times 1.3\text{ mm} \times 0.4\text{ mm}$, and the energy resolution is approximately 1% FWHM for single pixel events and 1.6% FWHM for two pixel events.

Sequence reconstruction is necessary in image reconstruction algorithms such as the simple back-projection and the filtered back-projection. Monte Carlo simulation data shows that following a Compton edge test, there is a greater probability for the first interaction to deposit more energy across all the energy range in a $15\text{ mm} \times 15\text{ mm} \times 10\text{ mm}$ detector. The simple comparison method chooses the higher energy deposition as the first interaction if the event passes the Compton edge test. At 662 keV, this method can identify 77% of full-energy two-pixel events in simulations.

The deterministic method relies on the position information as well as the energy information to identify the sequence. Because of the small size of the detector, the deterministic method provides little advantage over the simple comparison method. Given the information of the direction of the incident gamma-rays, the sequencing efficiency can be improved even further.

The angular resolution of the imager can be affected by various factors, of which the detector position resolution is the limiting factor. The average separation distance between the positions of a two-pixel event is only about 4.3 mm at 662 keV. The $1.3 \text{ mm} \times 1.3 \text{ mm} \times 0.4 \text{ mm}$ position resolution introduces an angular uncertainty with standard deviation of about 12.4° . Because of the high Z number of CdZnTe, the Doppler broadening effect is another dominant factor, introducing 8.4° standard deviation in the angular uncertainty. Energy resolution and coherent scattering introduce relatively small effects in the angular uncertainty. When a number of detectors are arranged into an array, the angular uncertainty introduced by the position resolution can be decreased since more events are separated with longer distance. Although the variation in the angular uncertainty for different events introduces difficulties in image reconstruction algorithms, the variation also enables an improvement in angular resolution by selecting those events with less angular uncertainties (at the expense of detection efficiency).

Three different image reconstruction algorithms have been applied to the 4π Compton imager. The simple back-projection algorithm has relatively poor resolution, but it is a very straight forward method and may be an appropriate choice if identification of the presence of a source is more important than angular resolution. The angular resolution of the simple back-projection algorithm is about 50° for a Cs-137 source to the side of the detector. The filtered back-projection algorithm

utilizes the Fourier transform between the 4π sphere and the spherical harmonics to deconvolve the point spread function from the simple back-projection images. With recent advances in fast transform algorithms, the filtered back-projection algorithm can be operated in real-time. The angular resolution of the filtered back-projection algorithm is about 22° . The maximum likelihood method estimates the source distribution from a statistical point of view, resulting in the solution which is the most likely to generate the measured data. The angular resolution of the MLEM algorithm is about 12° after 24 iterations. When the source is in the vicinity of the detector, the finite size of the detector can help to identify the source-to-detector distance with near field imaging technique. More powerful 3-D imaging capability has been demonstrated using Monte Carlo simulations with a 3×3 CdZnTe detector array.

Because of the imaging capability of the detector, the system response function of the detector is a function of both the energy and the direction of the incident gamma-ray. A new energy-imaging integrated deconvolution algorithm is proposed and studied in this work. By applying the MLEM algorithm, the deconvolution gives the estimation of the true incident distribution of the gamma-rays as a function of both the energy and the direction. Comparing with the conventional energy spectral deconvolution method, the energy-imaging integrated deconvolution method is not sensitive to the direction of incident gamma-rays and the surrounding materials. The proposed algorithm can not remove the back-scattered photons because these photons are part of the incident gamma-ray spectrum. However, the back-scattered photons are spatially distributed and are not present in the localized energy spectrum at the true source directions.

Polarization is another important characteristic of gamma-rays. When a polarized gamma-ray is Compton scattered, an asymmetry exists in the scattered photon's

azimuthal direction. The polarization information can therefore be deduced by measuring the azimuthal distribution of the Compton scattered events. The position-sensitive CdZnTe detector was operated as a polarimeter, and 58% polarized 288 keV gamma-rays were measured. The measurement results showed good agreement with theoretical calculations and Monte Carlo simulations.

8.2 Suggestions for Future Work

There are several topics not addressed in this work that should be studied in the future. Currently, only the system response function for two-pixel events was modeled. At 662 keV, the fractions of one, two, and three-or-more pixel events are 31%, 37%, and 32%, respectively[94]. As the gamma-ray energy increases, the fraction of three or more pixel events also increases. It is necessary to model the system response function of three or more pixel events to increase the efficiency. It will be a challenging task since there will be $N!$ possible sequences for a N -pixel event.

Currently, the computation cost of the MLEM algorithm remains high. This is especially true for the energy-imaging integrated deconvolution algorithm as the number of pixels is very large. Ordered subset expectation maximization (OSEM) algorithm[95] is a possible way to accelerate the reconstruction speed. The OSEM algorithm divides the measured data set into several subsets, and uses the reconstruction image of the previous subset as the initial image of the next subset. The algorithm can provide order-of-magnitude acceleration over the conventional MLEM algorithm and is easy to implement[95]. However, the variance and convergence properties of the OSEM algorithm are still unclear.

In the filtered back-projection algorithm, the point spread function is obtained from a simulation with a Cs-137 source placed at the side of the detector. In reality,

the point spread function depends on the incident gamma-ray energy and direction. The volume of the CdZnTe detector is quite symmetric, therefore the PSF of the source from the side can be applied to other source directions. However, for a detector system with large geometrical asymmetry (such as a detector array), the PSF should be modeled as a function of the incident gamma-ray direction. The PSF should also be calculated at different energies.

Another promising avenue of study is the possibility to improve sensitivity by making best use of the inherent imaging capability. In applications where a point source is to be detected in the presence of a strong background, traditional gamma-ray spectrometers use the counts in the full-energy window as the detection criteria. However, the natural gamma-ray background is usually distributed in all directions. By looking into the source direction, the background will be reduced thus the signal-to-noise ratio can be increased. Therefore, the sensitivity of detecting a point source in a strong background can be improved over traditional gamma-ray spectrometers.

BIBLIOGRAPHY

BIBLIOGRAPHY

- [1] M. W. Groch and W. D. Erwin, "Single-photon emission computed tomography in the year 2001: instrumentation and quality control," *Journal of Nuclear Medicine Technology*, vol. 29, no. 1, p. 12, 2001.
- [2] J. M. Ollinger and J. A. Fessler, "Positron emission tomography," *IEEE Signal Processing Magazine*, vol. 14, no. 1, pp. 43–55, 1997.
- [3] E. E. Fenimore and T. M. Cannon, "Coded aperture imaging with uniformly redundant arrays," *Applied Optics*, vol. 17, no. 3, pp. 337–347, 1978.
- [4] D. M. Smith, G. J. Hurford, and S. E. Boggs, "Rotating modulation collimator imagers," *New Astronomy Reviews*, vol. 48, no. 1-4, pp. 209–213, 2004.
- [5] M. Singh, "An electronically collimated gamma camera for single photon emission computed tomography. Part I: Theoretical considerations and design criteria," *Medical Physics*, vol. 10, no. 4, pp. 421–427, 1983.
- [6] M. Singh and D. Doria, "An electronically collimated gamma camera for single photon emission computed tomography. Part II: Image reconstruction and preliminary experimental measurements," *Medical Physics*, vol. 10, no. 4, pp. 428–435, 1983.
- [7] V. Schönfelder, A. Hirner, and K. Schneider, "A telescope for soft gamma ray astronomy," *Nuclear Instruments and Methods*, vol. 107, no. 2, pp. 385–394, 1973.
- [8] R. W. Todd, J. M. Nightingale, and D. B. Everett, "A proposed gamma camera," *Nature*, vol. 251, no. 5471, pp. 132–134, 1974, 10.1038/251132a0 10.1038/251132a0.
- [9] V. Schönfelder, H. Aarts, K. Bennett, H. de Boer, J. Clear, W. Collmar, A. Connors, A. Deerenberg, R. Diehl, A. von Dordrecht, J. W. den Herder, W. Hermsen, M. Kippen, L. Kuiper, G. Lichti, J. Lockwood, J. Macri, M. McConnell, D. Morris, R. Much, J. Ryan, G. Simpson, M. Snelling, G. Stacy, H. Steinle, A. Strong, B. N. Swanenburg, B. Taylor, C. de Vries, and C. Winkler, "Instrument description and performance of the Imaging Gamma-Ray Telescope COMPTEL aboard the Compton Gamma-Ray Observatory," *Astrophysical Journal Supplement Series*, vol. 86, pp. 657–692, June 1993.
- [10] A. W. Strong, "Diffuse Galactic Gamma-Ray Continuum Emission," *Space Science Reviews*, vol. 76, pp. 205–230, 1996.
- [11] J. B. Martin, G. F. Knoll, D. K. Wehe, N. Dogan, V. Jordanov, N. Petrick, and M. Singh, "A ring Compton scatter camera for imaging medium energy gamma rays," *IEEE Transactions on Nuclear Science*, vol. 40, no. 4, pp. 972–978, 1993.
- [12] T. Kamae, N. Hanada, and R. Enomoto, "Prototype design of multiple Compton gamma-ray camera," *IEEE Transactions on Nuclear Science*, vol. 35, no. 1, pp. 352–355, 1988.
- [13] N. Dogan, D. K. Wehe, and G. F. Knoll, "Multiple Compton scattering gamma ray imaging camera," *Nuclear Instruments and Methods in Physics Research Section A: Accelerators, Spectrometers, Detectors and Associated Equipment*, vol. 299, no. 1-3, pp. 501–506, 1990.

- [14] J. W. LeBlanc, N. H. Clinthorne, C. H. Hua, E. Nygard, W. L. Rogers, D. K. Wehe, P. Weilhammer, and S. J. Wilderman, "C-SPRINT: a prototype Compton camera system for low energy gamma ray imaging," *IEEE Transactions on Nuclear Science*, vol. 45, no. 3, pp. 943–949, 1998, 0018-9499.
- [15] J. W. LeBlanc, N. H. Clinthorne, C.-H. Hua, E. Nygard, W. L. Rogers, D. K. Wehe, P. Weilhammer, and S. J. Wilderman, "Experimental results from the C-SPRINT prototype Compton camera," *IEEE Transactions on Nuclear Science*, vol. 46, no. 3, pp. 201–204, 1999.
- [16] J. W. LeBlanc, N. H. Clinthorne, C. Hua, W. L. Rogers, D. K. Wehe, and S. J. Wilderman, "A Compton camera for nuclear medicine applications using $^{113\text{m}}\text{In}^1$," *Nuclear Instruments and Methods in Physics Research Section A: Accelerators, Spectrometers, Detectors and Associated Equipment*, vol. 422, no. 1-3, pp. 735–739, 1999.
- [17] R. B. Piercey, A. G. Weisenberger, J. E. McKisson, and C. Girit, "Preliminary characteristics of a germanium-based, Compton-scatter telescope," *IEEE Transactions on Nuclear Science*, vol. 36, no. 1, pp. 887–890, 1989.
- [18] J. E. McKisson, P. S. Haskins, G. W. Phillips, S. E. King, R. A. August, R. B. Piercey, and R. C. Mania, "Demonstration of three-dimensional imaging with a germanium Compton camera," *IEEE Transactions on Nuclear Science*, vol. 41, no. 4, pp. 1221–1224, 1994.
- [19] B. F. Philips, S. E. Inderhees, R. A. Kroeger, W. N. Johnson, R. L. Kinzer, J. D. Kurfess, B. L. Graham, and N. Gehrels, "Performance of a Compton telescope using position-sensitive germanium detectors," *IEEE Transactions on Nuclear Science*, vol. 43, no. 3, pp. 1472–1475, 1996.
- [20] G. J. Schmid, D. A. Beckedahl, J. E. Kammeraad, J. J. Blair, K. Vetter, and A. Kuhn, "Gamma-ray Compton camera imaging with a segmented HPGe," *Nuclear Instruments and Methods in Physics Research Section A: Accelerators, Spectrometers, Detectors and Associated Equipment*, vol. 459, no. 3, pp. 565–576, 2001.
- [21] T. Niedermayr, K. Vetter, L. Mihailescu, G. J. Schmid, D. Beckedahl, J. Blair, and J. Kammeraad, "Gamma-ray imaging with a coaxial HPGe detector," *Nuclear Instruments and Methods in Physics Research Section A: Accelerators, Spectrometers, Detectors and Associated Equipment*, vol. 553, no. 3, pp. 501–511, 2005.
- [22] E. A. Wulf, J. Ampe, W. N. Johnson, R. A. Kroeger, J. D. Kurfess, and B. E. Philips, "Depth measurement in a germanium strip detector," *IEEE Transactions on Nuclear Science*, vol. 49, no. 4, pp. 1876–1880, 2002.
- [23] E. A. Wulf, B. F. Philips, W. N. Johnson, R. A. Kroeger, J. D. Kurfess, and E. I. Novikova, "Germanium strip detector Compton telescope using three-dimensional readout," *IEEE Transactions on Nuclear Science*, vol. 50, no. 4, pp. 1182–1189, 2003.
- [24] E. A. Wulf, B. F. Philips, W. N. Johnson, J. D. Kurfess, and E. I. Novikova, "Thick silicon strip detector Compton imager," *IEEE Transactions on Nuclear Science*, vol. 51, no. 5, pp. 1997–2003, 2004.
- [25] R. A. Kroeger, W. N. Johnson, J. D. Kurfess, B. F. Philips, and E. A. Wulf, "Three-Compton telescope: theory, simulations, and performance," *Nuclear Science, IEEE Transactions on*, vol. 49, no. 4, pp. 1887–1892, 2002.
- [26] E. A. Wulf, B. F. Philips, J. D. Kurfess, E. I. Novikova, and C. M. Fitzgerald, "A Silicon Compton Imager," *Nuclear Science Symposium Conference Record, 2005 IEEE*, vol. 1, pp. 1–5, 2005.

- [27] M. Burks, D. Chivers, C. E. Cork, M. F. Cunningham, L. Fabris, D. Gunter, E. L. Hull, D. J. Lange, H. Manini, L. Mihailescu, K. Nelson, T. R. Niedermayr, J. D. Valentine, K. Vetter, and D. Wright, "Imaging Performance of the Si/Ge Hybrid Compton Imager," *Nuclear Science Symposium Conference Record, 2005 IEEE*, vol. 1, pp. 6–10, 2005.
- [28] Y. F. Du, Z. He, G. F. Knoll, D. K. Wehe, and W. Li, "Evaluation of a Compton scattering camera using 3-D position sensitive CdZnTe detectors," *Nuclear Instruments and Methods in Physics Research, Section A: Accelerators, Spectrometers, Detectors and Associated Equipment*, vol. 457, no. 1-2, pp. 203–211, 2001.
- [29] F. Zhang, Z. He, D. Xu, G. Knoll, D. Wehe, and J. Berry, "Improved Resolution for 3-D Position Sensitive CdZnTe Spectrometers," *IEEE Transactions on Nuclear Science*, vol. 51, no. 5, pp. 2427–2431, 2004.
- [30] C. Lehner, Z. He, and F. Zhang, "4-pi Compton imaging using a 3-D position-sensitive CdZnTe detector via weighted list-mode maximum likelihood," *IEEE Transactions on Nuclear Science*, vol. 51, no. 4, pp. 1618–1624, 2004.
- [31] T. J. O'Neill, D. Bhattacharya, M. Polsen, A. D. Zych, J. Samimi, and A. Akyuz, "Development of the TIGRE Compton telescope for intermediate-energy gamma-ray astronomy," *IEEE Transactions on Nuclear Science*, vol. 50, no. 2, pp. 251–257, 2003.
- [32] E. Aprile, A. Curioni, K. L. Giboni, U. Oberlack, and S. Ventura, "An upgraded data-acquisition system for the balloon-borne liquid xenon γ -ray imaging telescope LXeGRIT," *IEEE Transactions on Nuclear Science*, vol. 48, no. 4, pp. 1299–1305, 2001.
- [33] A. Takada, K. Hattori, H. Kubo, K. Miuchi, T. Nagayoshi, H. Nishimura, Y. Okada, R. Orito, H. Sekiya, A. Tada, and T. Tanimori, "Development of an advanced Compton camera with gaseous TPC and scintillator," *Nuclear Instruments and Methods in Physics Research Section A: Accelerators, Spectrometers, Detectors and Associated Equipment*, vol. 546, no. 1-2, pp. 258–262, 2005.
- [34] Z. He, "Review of the Shockley-Ramo theorem and its application in semiconductor gamma-ray detectors," *Nuclear Instruments and Methods in Physics Research Section A: Accelerators, Spectrometers, Detectors and Associated Equipment*, vol. 463, no. 1-2, pp. 250–267, 2001.
- [35] O. Frisch, *British Atomic Energy Report BR-49*, 1944.
- [36] P. N. Luke, "Single-polarity charge sensing in ionization detectors using coplanar electrodes," *Applied Physics Letters*, vol. 65, no. 22, pp. 2884–2886, 1994.
- [37] —, "Unipolar charge sensing with coplanar electrodes-application to semiconductor detectors," *IEEE Transactions on Nuclear Science*, vol. 42, no. 4, pp. 207–213, 1995.
- [38] H. H. Barrett, J. D. Eskin, and H. B. Barber, "Charge Transport in Arrays of Semiconductor Gamma-Ray Detectors," *Physical Review Letters*, vol. 75, pp. 156–159, 1995.
- [39] Z. He, G. F. Knoll, D. K. Wehe, R. Rojeski, C. H. Mastrangelo, M. Hammig, C. Barrett, and A. Uritani, "1-D position sensitive single carrier semiconductor detectors," *Nuclear Instruments and Methods in Physics Research Section A: Accelerators, Spectrometers, Detectors and Associated Equipment*, vol. 380, no. 1-2, pp. 228–231, 1996.
- [40] Z. He, G. F. Knoll, D. K. Wehe, and J. Miyamoto, "Position-sensitive single carrier CdZnTe detectors," *Nuclear Instruments and Methods in Physics Research, Section A: Accelerators, Spectrometers, Detectors and Associated Equipment*, vol. 388, no. 1-2, pp. 180–185, 1997.
- [41] Z. He, W. Li, G. F. Knoll, D. K. Wehe, J. Berry, and C. M. Stahle, "3-D position sensitive CdZnTe gamma-ray spectrometers," *Nuclear Instruments and Methods in Physics Research, Section A (Accelerators, Spectrometers, Detectors and Associated Equipment)*, vol. 422, no. 1-3, pp. 173–8, 1999.

- [42] W. Li, Z. He, G. F. Knoll, D. K. Wehe, and C. M. Stahle, "Spatial variation of energy resolution in 3-D position sensitive CZT gamma-ray spectrometers," *IEEE Transactions on Nuclear Science*, vol. 46, no. 3, pt.1, pp. 187–92, 1999.
- [43] Z. He, W. Li, G. F. Knoll, D. K. Wehe, and C. M. Stahle, "Measurement of material uniformity using 3-D position sensitive CdZnTe gamma-ray spectrometers," *Nuclear Instruments and Methods in Physics Research, Section A: Accelerators, Spectrometers, Detectors and Associated Equipment*, vol. 441, no. 3, pp. 459–467, 2000.
- [44] Z. Feng, H. Zhong, and D. Xu, "Analysis of detector response using 3-D position-sensitive CZT gamma-ray spectrometers," *Nuclear Science, IEEE Transactions on*, vol. 51, no. 6, pp. 3098–3104, 2004.
- [45] F. Zhang, Z. He, G. F. Knoll, D. K. Wehe, and J. E. Berry, "3-D position sensitive CdZnTe spectrometer performance using third generation VAS/TAT readout electronics," *IEEE Transactions on Nuclear Science*, vol. 52, no. 5, pp. 2009–2016, 2005.
- [46] Particle Data Group, R. M. Barnett, C. D. Carone, D. E. Groom, T. G. Trippe, C. G. Wohl, B. Armstrong, P. S. Gee, G. S. Wagman, F. James, M. Mangano, K. Monig, L. Montanet, J. L. Feng, H. Murayama, J. J. Hernandez, A. Manohar, M. Aguilar-Benitez, C. Caso, R. L. Crawford, M. Rocs, N. A. Tornqvist, K. G. Hayes, K. Hagiwara, K. Nakamura, M. Tanabashi, K. Olive, K. Honscheid, P. R. Burchat, R. E. Shrock, S. Eidelman, R. H. Schindler, A. Gurtu, K. Hikasa, G. Conforto, R. L. Workman, C. Grab, and C. Amsler, "Review of Particle Physics," *Physical Review D*, vol. 54, no. 1, pp. 1–708, 1996.
- [47] D. H. Dowell, A. M. Sandorfi, A. Q. R. Baron, B. J. Fineman, O. C. Kistner, G. Matone, C. E. Thorn, and R. M. Sealock, "Computed tomography of scintillators with muons: Understanding the response to high energy gamma rays," *Nuclear Instruments and Methods in Physics Research Section A: Accelerators, Spectrometers, Detectors and Associated Equipment*, vol. 286, no. 1-2, pp. 183–201, 1990.
- [48] E. Frlez, I. Supek, K. A. Assamagan, C. Bronnimann, T. Flugel, B. Krause, D. W. Lawrence, D. Mzavia, D. Pocanic, and D. Renker, "Cosmic muon tomography of pure cesium iodide calorimeter crystals," *Nuclear Instruments and Methods in Physics Research Section A: Accelerators, Spectrometers, Detectors and Associated Equipment*, vol. 440, no. 1, pp. 57–85, 2000.
- [49] C. E. Lehner, "4-Pi Compton imaging using a single 3-D position-sensitive CdZnTe detector," *Ph. D. Thesis, University of Michigan*, 2004.
- [50] Y. F. Du, Z. He, W. Li, G. F. Knoll, and D. K. Wehe, "Monte Carlo investigation of the charge sharing effects in 3-D position sensitive CdZnTe gamma ray spectrometers," *IEEE Transactions on Nuclear Science*, vol. 46, no. 4, pp. 844–847, 1999.
- [51] S. Agostinelli, J. Allison, K. Amako, J. Apostolakis, H. Araujo, P. Arce, M. Asai, D. Axen, S. Banerjee, and G. Barrand, "G4—a simulation toolkit," *Nuclear Instruments and Methods in Physics Research Section A: Accelerators, Spectrometers, Detectors and Associated Equipment*, vol. 506, no. 3, pp. 250–303, 2003.
- [52] G. F. Knoll, *Radiation detection and measurement*, 3rd ed. New York: J. Wiley, 2000.
- [53] A. Niemelä and H. Sipilä, "Evaluation of CdZnTe detectors for soft x-ray applications," *IEEE Transactions on Nuclear Science*, vol. 41, no. 4, pp. 1054–1057, 1994.
- [54] F. Salvat, J. M. Fernández-Varea, and J. Sempau, *PENELOPE - a code system for Monte Carlo simulation of electron and photon transport*. Issy-les-Moulineaux, France: Workshop Proceedings, 2003.

- [55] R. Ribberfors, "Relationship of the relativistic Compton cross section to the momentum distribution of bound electron states," *Physical Review B*, vol. 12, pp. 2067–2074, 1975.
- [56] D. Brusa, G. Stutz, J. A. Riveros, J. M. Fernandez-Varea, and F. Salvat, "Fast sampling algorithm for the simulation of photon Compton scattering," *Nuclear Instruments and Methods in Physics Research Section A: Accelerators, Spectrometers, Detectors and Associated Equipment*, vol. 379, no. 1, pp. 167–175, 1996.
- [57] F. Biggs, L. B. Mendelsohn, and J. B. Mann, "Hartree-Fock Compton profiles for the elements," *Atomic Data and Nuclear Data Tables*, vol. 16, no. 3, pp. 201–309, 1975.
- [58] M. S. Tom Hebert, Richard Leahy, "Three-dimensional maximum-likelihood reconstruction for an electronically collimated single-photon-emission imaging system," *Optical Society of America*, vol. 7, no. 7, pp. 1305–1313, 1990.
- [59] M. J. Cree and P. J. Bones, "Towards direct reconstruction from a gamma camera based on Compton scattering," *IEEE Transactions on Medical Imaging*, vol. 13, no. 2, pp. 398–407, 1994.
- [60] R. Basko, G. L. Zeng, and G. T. Gullberg, "Application of spherical harmonics to image reconstruction for the Compton camera," *Physics in Medicine and Biology*, vol. 43, no. 4, pp. 887–894, 1998.
- [61] L. Parra, "Reconstruction of cone-beam projections from Compton scattered data," *IEEE Transactions on Nuclear Science*, vol. 47, no. 4, pp. 1543–1550, 2000.
- [62] R. D. Evans, *The atomic nucleus*. New York: McGraw-Hill, 1955.
- [63] T. Tomitani and M. Hirasawa, "Image reconstruction from limited angle Compton camera data," *Physics in Medicine and Biology*, no. 12, pp. 2129–2145, 2002.
- [64] J. R. Driscoll and D. M. Healy, "Computing Fourier Transforms and Convolutions on the 2-Sphere," *Advances in Applied Mathematics*, vol. 15, no. 2, pp. 202–250, 1994.
- [65] D. M. Healy Jr., D. Rockmore, P. Kostelec, and S. Moore, "FFTs for the 2-Sphere-Improvements and Variations," *Journal of Fourier Analysis and Applications*, vol. 9, no. 4, pp. 341–385, 2003.
- [66] S. Kunis and D. Potts, "Fast spherical Fourier algorithms," *Journal of Computational and Applied Mathematics*, vol. 161, no. 1, pp. 75–98, 2003.
- [67] J. Hsieh, *Computerized Tomography: Principles, Design, Artifacts, and Recent Advances*. Bellingham: SPIE-The International Society for Optical Engineering, 2003.
- [68] T. Budinger, S. Derenzo, G. Gullberg, W. Greenberg, and R. Huesman, "Emission computer assisted tomography with single-photon and positron annihilation photon emitters," *Journal of Computer Assisted Tomography*, vol. 1, pp. 131–145, 1977.
- [69] M. Ter-Pogossian, M. Raichle, and B. Sobel, "Positron emission tomography," *Scientific American*, vol. 243, no. 170–181, 1980.
- [70] L. Shepp and Y. Vardi, "Maximum likelihood reconstruction for emission tomography," *IEEE Transactions on Medical Imaging*, vol. MI-1, pp. 113–122, April 1982.
- [71] A. Dempster, N. Laird, and D. Rubin, "Maximum likelihood from incomplete data via the EM algorithm," *Journal of the Royal Statistical Society*, vol. B39, no. 1, pp. 1–38, 1977.
- [72] J. M. Fitzpatrick and M. Sonka, *Handbook of Medical Imaging, Volume 2. Medical Image Processing and Analysis*. SPIE Press, 2000.

- [73] K. Lange and R. Carson, "EM reconstruction algorithms for emission and transmission tomography," *Journal of Computer Assisted Tomography*, vol. 8, no. 2, pp. 302–316, 1984.
- [74] T. M. Cover, "An algorithm for maximizing expected log investment return," *IEEE Transactions on Information Theory*, vol. 30, no. 2, pp. 369–373, 1984.
- [75] I. Csiszàr and G. Tusnàdy, "Information geometry and alternating minimization procedures," *Statistics and Decisions, Supplemental Issue*, no. 1, pp. 205–237, 1982.
- [76] Y. Vardi, L. A. Shepp, and L. Kaufman, "A statistical model for positron emission tomography (with discussion)," *Journal of the American Statistical Association*, vol. 80, pp. 8–37, 1985.
- [77] H. Barrett, T. White, and L. Parra, "List-mode likelihood," *Journal of the Optical Society of America*, vol. A14, no. 11, pp. 2914–2923, November 1997 1997.
- [78] L. Bouchet, "A comparative study of deconvolution methods for gamma-ray spectra," *Astronomy and Astrophysics, Supplemental Series*, vol. 113, pp. 167–183, 1995.
- [79] R. L. Parker, "Understanding inverse theory," *Annual Reviews of Earth and Planetary Sciences*, vol. 5, pp. 35–64, 1977.
- [80] T. J. Loredo and R. I. Epstein, "Analyzing gamma-ray burst spectral data," *the Astrophysical Journal*, vol. 336, pp. 896–919, 1989.
- [81] D. L. Phillips, "A technique for the numerical solution of certain integral equations of the first kind," *Journal of the Association for Computing Machinery*, vol. 9, no. 1, pp. 84–97, 1962.
- [82] E. T. Jaynes, "Information Theory and Statistical Mechanics," *Physical Review*, vol. 106, no. 4, p. 620, 1957.
- [83] L. Meng and D. Ramsden, "An inter-comparison of three spectral-deconvolution algorithms for gamma-ray spectroscopy," *IEEE Transactions on Nuclear Science*, vol. 47, no. 4, pp. 1329–1336, 2000.
- [84] R. Carson, W. Barker, J.-S. Liow, and C. Johnson, "Design of a motion-compensation OSEM list-mode algorithm for resolution-recovery reconstruction for the HRRT," in *Nuclear Science Symposium Conference Record, 2003 IEEE*, vol. 5, 2003, pp. 3281–3285 Vol.5.
- [85] J. Qi, "Calculation of the Sensitivity Image in List-Mode Reconstruction," in *Nuclear Science Symposium Conference Record, 2005 IEEE*, vol. 4, 2005, pp. 1924–1928.
- [86] L. Shepp, "From Convolution Algorithms To Maximum Likelihood," in *Nuclear Science Symposium Conference Record, 1990 IEEE*, 1990, pp. 1441–1444.
- [87] E. Veklerov, J. Llacer, and E. J. Hoffman, "MLE reconstruction of a brain phantom using a Monte Carlo transition matrix and a statistical stopping rule," *IEEE Transactions on Nuclear Science*, vol. 35, no. 1, pp. 603–607, 1988.
- [88] W. Coburn and S. E. Boggs, "Polarization of the prompt [gamma]-ray emission from the [gamma]-ray burst of 6 December 2002," *Nature*, vol. 423, no. 6938, pp. 415–417, 2003.
- [89] M. L. McConnell and J. M. Ryan, "Status and prospects for polarimetry in high energy astrophysics," *New Astronomy Reviews*, vol. 48, no. 1-4, pp. 215–219, 2004.
- [90] S. Inderhees, B. Philips, R. Kroeger, W. Johnson, R. Kinzer, J. Kurfess, B. Graham, and N. Gehrels, "Spectroscopy, imaging and Compton-scatter polarimetry with a germanium strip detector," *IEEE Transactions on Nuclear Science*, vol. 43, no. 3, pp. 1467–1471, 1996.

- [91] R. A. Kroeger, W. N. Johnson, J. D. Kurfess, and B. F. Philips, "Gamma ray polarimetry using a position sensitive germanium detector," *Nuclear Instruments and Methods in Physics Research Section A: Accelerators, Spectrometers, Detectors and Associated Equipment*, vol. 436, no. 1-2, pp. 165–169, 1999.
- [92] D. Xu, Z. He, C. E. Lehner, and F. Zhang, "4-pi Compton imaging with single 3D position sensitive CdZnTe detector," *Proceedings SPIE*, vol. 5540, pp. 144–155, 2004.
- [93] D. Xu, Z. He, and F. Zhang, "Detection of Gamma Ray Polarization Using a 3-D Position-Sensitive CdZnTe Detector," *Nuclear Science, IEEE Transactions on*, vol. 52, no. 4, pp. 1160–1164, 2005.
- [94] F. Zhang, "Events reconstruction in 3-D position sensitive CdZnTe gamma-ray spectrometers," *Ph. D. Thesis, University of Michigan*, 2005.
- [95] H. M. Hudson and R. S. Larkin, "Accelerated image reconstruction using ordered subsets of projection data," *IEEE Transactions on Medical Imaging*, vol. 13, no. 4, pp. 601–609, 1994.